Fermi National Accelerator Laboratory

FN-514
[SSC-N-641]

Energy Deposition in Large Targets by 1-20 TeV Proton Beams

S. Qian* and A. Van Ginneken
Fermi National Accelerator Laboratory
P.O. Box 500, Batavia, Illinois 60510 U.S.A.

May 1989

Operated by Universities Research Association, Inc., under contract with the United States Department of Energy

Energy Deposition in Large Targets by 1–20 TeV Proton Beams

S. Qian* and A. Van Ginneken
Fermi National Accelerator Laboratory†
P. O. Box 500, Batavia, IL 60510

May 1989

Abstract

Results of energy deposition calculations are reported for proton beams of 1 TeV to 20 TeV incident on a variety of targets and for a large range of rms beam sizes. Targets include solid cylinders (dumps) of various materials as well as segmented dumps, i.e., slabs of variable thickness spaced apart, which allow the beam and developing cascade to spread radially with consequent reductions in maximum energy deposited. The case of oblique incidence of beam on target is contrasted with perpendicular entrance. Application to beam sweeping and to other practical uses are briefly discussed.

1 Introduction

This paper provides some background information on energy deposition densities in large targets for incident protons in the TeV regime. Such information is useful, e.g., in design of beam dumps and in assessing consequences of beam loss in superconducting magnets and detector components [1]. The present study is complementary to earlier work [2] which dealt with hadron and muon dose outside relatively thick shields but has the same motivation and perspective as [2], i.e., to serve as rough guide from which more detailed design and development work can be launched. Specifically, it is

*Present address: CERN, Geneva, Switzerland.

†Fermi National Accelerator Laboratory is operated by Universities Research Association under contract with the US Department of Energy.

attempted to calculate the energy density, and its spatial dependence, in a thick target in the broad vicinity of its maximum, which is expected to occur along the beam axis at depths of up to a few interaction lengths into the target, depending on beam size. Analysis of these problems is excluded from consideration in [2].

The energy range explored is between 1 and 20 TeV (fixed target) with emphasis on the latter since less is known from experience at the higher energies and since potential problems are more severe there for the SSC: the energy is higher, beams are smaller and magnets are operated closer to their quenching limit. A sample of 1 TeV and 10 TeV results indicates how the calculations scale with energy and has some direct interest as well: Tevatron [3] and injection into SSC (1 TeV), and the contemplated Large Hadron Collider at CERN ($\sim$ 10TeV). Only incident protons are considered. All results presented here derive from the Monte-Carlo program CASIM [4] which simulates hadronic cascades, supplemented by AEGIS [5] for electromagnetic showers. To apply CASIM in the multi-TeV domain to the type of problems addressed here necessitates major changes in both particle production and transport. A brief discussion of these matters appears in Sec. 2. In addition to incident proton energy, other variables of the problem explored here are target atomic number, beam size, and beam-target geometry. The target species studied are carbon, aluminum, iron, and tungsten. These cover most of the Z–range, and each is directly useful. In all cases the beam distribution is assumed to be Gaussian in each transverse coordinate with $\sigma_x = \sigma_y$ and with $x' = y' = 0$ for all particles. Beam size ranges from $\sigma = 0.005\ cm$ to 20 cm. Three geometries are analyzed: (1) (the quintessential) solid cylinders with beam on axis, (2) solid targets with beam incident at relatively small (grazing) angles to the surface, and (3) segmented targets which interrupt the build-up of the cascade and thereby increase its transverse spread and dilute the energy density. Only targets of homogeneous composition are included. Heterogeneous targets, while readily accomodated in the program, typically evolve only in the later stages of a design. The same holds true for a more complete description of the incident beam.

Results, along with some practical implications, are discussed in Sec. 3 and are all presented in graphical form. To prevent the text from becoming too fragmented, the (full page) figures exhibiting the main results are placed at the end, while a few explanatory figures remain in-text. The Appendix contains a brief comparison of the present work with other calculations [6] at these elevated energies and with an experiment [7] at lower energy (300 GeV). A note on notation: the symbols for energy deposition

density used throughout are

ρ_E: energy density anywhere in the target;

ρ_E^{max}: maximum ρ_E at a given depth (or for any other coordinate held fixed);

$\widehat{\rho}_E^{max}$: maximum ρ_E encountered in the entire target.

2 Physical Models

This section outlines changes made in CASIM to address specifically the problem of energy deposition at TeV energies. These changes consist chiefly of extending the physical model of inelastic interactions of hadrons with nuclear targets to $20 TeV$-plus lab energy and of a more refined simulation of the energy deposition along a particle's trajectory. Since beams are generally smaller in transverse size at these energies, particlular attention must be paid to lateral spread of the energy deposition at small radii.

The physical processes occurring in a thick target can be broadly classified as *elastic*, *radiative*, and *inelastic*. The elastic processes included are multiple- and large-angle Coulomb scattering, coherent and incoherent nuclear scattering and collisions with atomic electrons. The radiative part consists of bremsstrahlung and direct pair production both off nuclei and off atomic electrons. The typical inelastic interaction with a target nucleus is characterized by the production of (many) additional particles (see Sec. 2.1). However, when a collision proceeds *diffractively* and only the *target* nucleon is excited to a state of low invariant mass, the incident particle loses very little momentum and resembles an elastically scattered one. This case is treated separately from the other inelastic events [8]. For completeness, inelastic interactions of hadrons with atomic electrons are also included [9].

To put the models of particle production and energy deposition into proper perspective it is recalled that CASIM is a weighted Monte Carlo calculation. Briefly, when a hadron member of the cascade undergoes an inelastic nuclear interaction only one *cascade propagating* particle is selected to represent all outgoing particles. Pursuing this throughout the cascade means such a particle represents an entire generation of cascade particles. Particle type, momentum, and angle are selected from an *inclusive distribution* (and its integrals), which represents the assumed physical model, but weighted by the energy of the outgoing particle. The latter assures that particles are represented roughly in proportion to their ability to produce

more particles in subsequent generations. For most applications, in addition to the propagating particle, one or more *recording* particles are generated from each inelastic interaction with intent to simulate the contributions of their generation to the specific problem being analyzed. However, for energy density calculations of the type reported here, propagating particles also serve well as recording particles. This is also computationally efficient since it obviates the need to generate the extra particles.

At present, particles below 600 GeV are still treated as in the 'old' CASIM, both insofar as hadroproduction and energy deposition characteristics are concerned (except for a more complete simulation of the spatial distribution of the energy deposited by δ–rays, see below). The model has been reasonably successful in comparisons with thick target experiments in this energy range, including target heating in a variety of materials [10,11]. Some recent criticisms [12,13] point to a discrepancy between CASIM and other codes. This discrepancy appears limited to higher atomic weight target materials and is attributed [13] to an overestimate of the leading particle component in the (Hagedorn-Ranft [14]) particle production model used in CASIM. Qualitatively, this seems plausible, based on observed trends in recent particle production experiments on nuclear targets [15]. Being limited to heavy nuclear targets, such a discrepancy would not necessarily contradict the comparisons referred to above (except possibly some target heating experiments [11]). Recently published comparisons of CASIM results with experiment [7] in [12,13] are discussed in the Appendix, along with a more complete CASIM simulation of that particlular experiment [7].

2.1 Hadron Production

In addition to the above mentioned question for heavier targets, the Hagedorn-Ranft hadroproduction model [14] used in CASIM is in obvious difficulty at SSC energies, as discussed in [2]. While these difficulties are not expected to invalidate estimates of, e.g., dose outside of a thick shield, estimates of the maximum energy deposition, which receives large contributions from the first few generations of the hadronic cascade and associated electromagnetic showers, are expected to be much more sensitive to the particle production model. For this reason hadroproduction is treated differently here above a somewhat arbitrary cut-off energy of 600 GeV.

The difficulties of the Hagedorn-Ranft model in the multi-TeV regime are not surprising considering the factor of 10^3 or so in energy between where the model was conceived (and where its parameters are fixed) and the SSC

regime. In addition, experimental and theoretical understanding gained in the interim can be incorporated into a model which is both simpler and more readily extrapolated and which can be easily adjusted to accomodate, e.g., new data from CERN and Tevatron colliders or new results of Monte Carlo calculations [16,17] of hadron production.

Such a model, which qualitatively satisfies the general features of inclusive hadroproduction and energy conservation, is briefly outlined below. It is recalled that CASIM uses *inclusive* distributions to represent hadroproduction and limits itself to nucleons and pions. Energy is conserved (on average) in hadroproduction, and these particles are sufficiently representative of all baryons and mesons for (general purpose) energy deposition calculations. Three types of particles are distinguished: (a) leading particles, (b) 'wounded' nucleons, and (c) produced pions. All cross sections are assumed to factorize in rapidity, y, and in p_T.

2.1.1 Leading Particles

The invariant cross section $Ed^3\sigma/dp^3 = (1/\pi)d^3\sigma/dydp_T^2$ is assumed to be constant over the entire range of y. This is close to what is observed experimentally for Feynman-x above 0.2 [18]. Its continuation over the entire range is made for simplicity and does not contradict measurement or the general physical picture. More precisely:

$$\frac{d\sigma}{dy} = k_i \left(0.18 - 0.06\sqrt{\ln A}\right) / (1 - C_e) \qquad 0 \leq y \leq y_{max} \qquad (1)$$

where $k_p = 1.0$ and $k_\pi = 0.45$ are both taken from experiment [18] and $k_n = k_p$ is assumed. A in Eq.1 is the atomic mass number and C_e is the charge exchange probability, assumed to equal 1/3 for both nucleons and pions. For the latter double charge exchange is neglected. The y-limit refers to lab rapidity for collision with a nucleon. Since the k_i are independent of energy, a flat spectrum in y means a slow growth in the average number of leading particles. This is not necessarily unphysical, since their number within a fixed rapidity interval of either incident particle stays constant and since their total number remains well below two even at $40\,TeV$.

The p_T^2 dependence is assumed to obey:

$$\frac{d\sigma}{dp_T^2} = k(e^{-\alpha p_T^2} + be^{-\beta p_T^2} + ce^{-\gamma p_T^2}) \qquad (2)$$

where k normalizes $d\sigma/dp_T^2$ to unity and where $\alpha = 4.7, \beta = 3.4, \gamma = 1.0, b = 0.03A^{0.4}$, and $c = [0.03\,(\ln(\ln p) - 2), 0]_{max}$. Most of the p_T dependence is

in the constants α and β which are from CERN ISR $p-p$ data [19], while b introduces an observed A–dependence at high p_T [15]. The third term causes a slow rise in $\langle p_T^2 \rangle$ with incident momentum so as to match CERN Collider results [20].

2.1.2 'Wounded' Nucleons

These are nucleons which have been struck by the incident particle (ignoring any possible difficulties with this concept). Their average number is assumed to be $\overline{\nu} = \sigma_{hp}A/\sigma_{hA}$, where subscripts hp and hA refer to hadron-proton and hadron-nucleus collisions. The y-distribution is represented by a half-Gaussian in the backward hemisphere, peaking at $y' = 0$ ($y' \equiv y/y_{max}$) and with $\sigma_{y'} = 0.23$ ($= \sigma^{\pi}_{y'}$, see below). The p_T dependence is as for leading particles (Eq. 2). These wounded nucleons share only a small fraction of the incident energy and are not very important in energy deposition studies.

2.1.3 Produced Pions

The y' distribution is assumed to be Gaussian, truncated at both kinematic limits. The peak is assumed to be at $y' = 0.5 - 0.07(\overline{\nu} - 1)$, with $\overline{\nu}$ as for the wounded nucleons and $\sigma_{y'} = 0.23$. These values are obtained from fits to experiments at lower energies. An energy dependent normalization ensures overall energy conservation. The p_T dependence is again as for leading particles except that $\alpha = 7.3, \beta = 2.5$, and $b = 0.012A^{0.4}$ here while c and γ remain the same.

Fig. 1 shows the average charged particle multiplicity and inelasticity of the different components for nuclear targets, as a function of energy.

2.2 Energy Deposition

The basic algortihms of energy deposition are discussed in [4] and [5]. A description of the elastic and radiative processes, which become important with increasing energy, and their implementation into Monte Carlo transport has appeared elsewhere [8,21]. To deposit the energy associated with those *point processes*, which produce photons or electrons, AEGIS [5] is called upon to generate electromagnetic showers. It should be noted that, in AEGIS, electrons below $5\,MeV$ are allowed to range out. Collisions with atomic electrons which transfer less than $10\,MeV$ kinetic energy are not simulated in detail. The average energy loss in a Monte Carlo step is determined and a random energy loss, chosen from a Landau distribution,

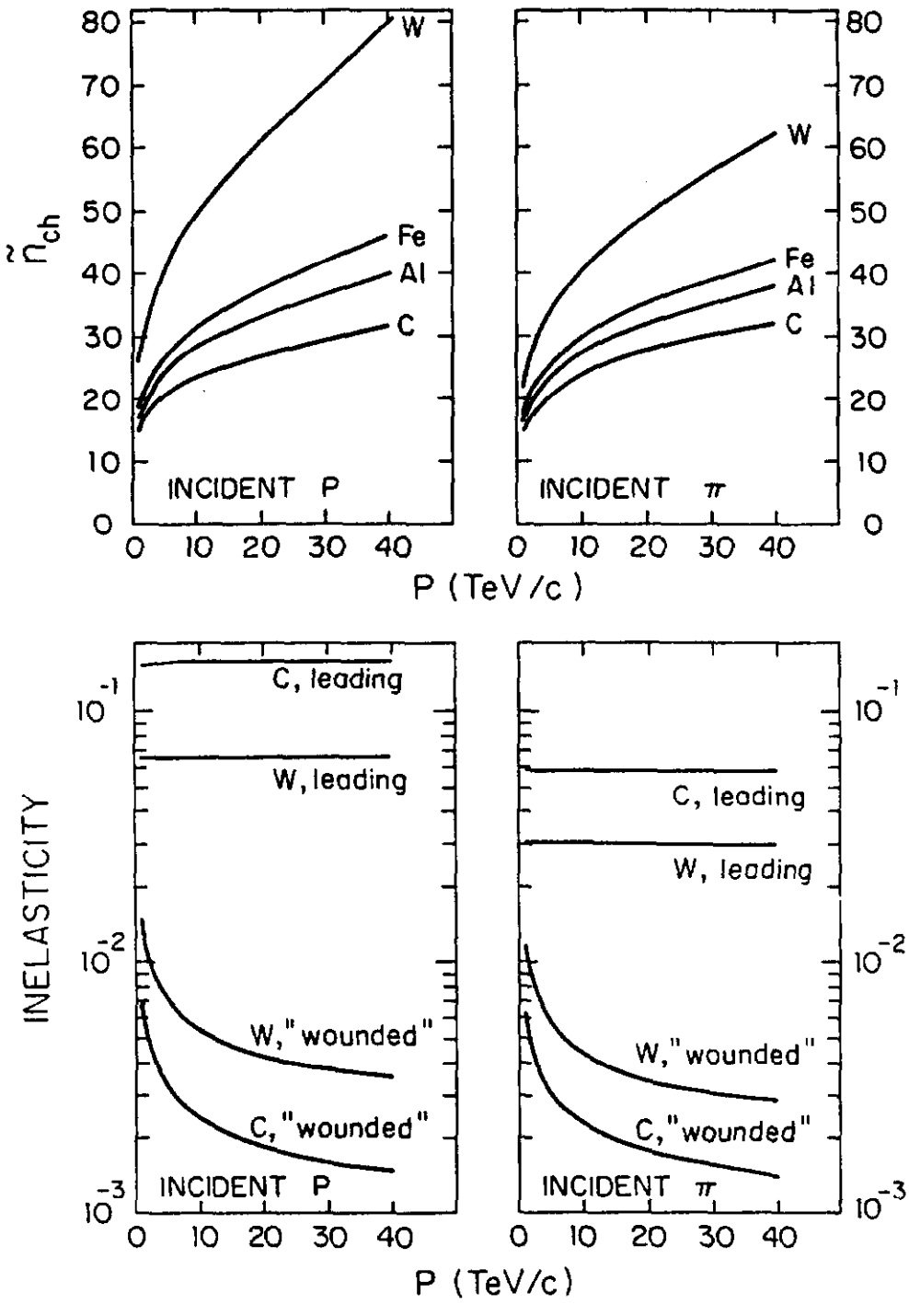

Figure 1: (top)–Average charged multiplicity for p and π on nuclear targets versus momentum. (bottom)–Average inelasticity for leading particles and 'wounded' nucleons for p and π on Carbon and Tungsten versus momentum. Missing inelasticity goes into *produced* pions.

is applied. To deposit this energy, a point is selected randomly along the particle's trajectory, taking account of multiple Coulomb scattering. The fraction carried off by electrons with energy below $0.10\,MeV$ is removed locally. The fraction with $(0.10 \leq T_e \leq 10\,MeV)$ is deposited at a point chosen randomly along the residual range of a representative electron originating at this point. The kinetic energy of this electron is selected from a T_e^{-1} distribution, which closely approximates $T_e P(T_e)$, where $P(T_e)$ is the probability [22] of producing an electron with kinetic energy T_e. Its angle with respect to the incident direction, $\theta_e \simeq \arcsin\sqrt{2m_e T_e}/p_e$, follows from momentum conservation. Energy losses for $T_e > 10\,MeV$ are fully simulated. A similar algorithm is incorporated in AEGIS.

The recoil energy of nuclei following coherent scattering is deposited locally since their range is well below the smallest beam size studied here. For incoherent scattering, the energy carried off by the target nucleon is deposited in the general vicinity of the particle track using the CASIM alogorithm.

3 Results

Calculated results for the three geometries mentioned in the Introduction are summarized in a set of graphs. The combinatorics of geometry, type of material, incident energy, etc., discourage an exhaustive treatment. Even for the small subset of calculations actually performed much more information is generated than can reasonably be reproduced here. For oblique incidence geometry and for segmented targets, the variations are virtually endless and what is included amounts to no more than a few examples. The results presented here are limited to targets of homogeneous composition. In performing the calculations, this limitation is exploited by writing for each material and energy (and for a sufficiently large number of incident particles) a 'history file' which contains serial identification, type, coordinates, direction, and momentum at birth for each particle participating in the cascade. A separate program then reads the history file and attends to the energy deposition routines. Each particle is now traced through the geometry in the usual fashion, with absorption taken into account on average, i.e., by reducing its weight exponentially with distance traversed, while the various contributions to the energy deposition are simulated and tallied. These particles are traced until escape or until their weight becomes negligible. Electromagnetic showers are also traced in this stage. Since,

for a homogeneous target (including one with voids), different geometries can be simply related by geometric scaling such a file can thus be used repeatedly with savings in computing time. Other computational benefits are that each half-program is simpler to deal with in terms of debugging, storage requirements, etc. Because of the common genealogy, results for different geometries are statistically strongly correlated. This is most useful in analyzing related geometries such as beams at different angles for oblique incidence, since systematic trends become more easily discerned.

The results presented here are smoothed with respect to statistical fluctuations, which are an obvious consequence of the Monte Carlo technique and are more prevalent at large z and/or r. Such smoothing may succeed more readily when done simultaneously for a large number of (interrelated) cases than for an isolated calculation. Hence it seems sensible to do so here, rather than serve the calculated results 'raw', but the user should remain aware of it.

Practical applications of the results included in this note center on the problem of beam dumping, accidental or intentional. Where such matters are discussed below, it is strictly from the narrow perspective of energy deposition. The many other questions which arise in this connection regarding heat transfer, shock waves, structural stability, quenching, radiological considerations, etc., are not addressed here.

3.1 Cylinders

The geometry studied here is the venerable cylindrical geometry with a beam entering the target centered on the axis. To save computing time the trick of simulating several beam sizes within the same run [23] is employed. (Essentially, a pencil beam is brought in along the cylinder axis and whenever an energy deposition event occurs a randomly variable vector, representing the distance of the beam particle to the cylinder axis, is added to the radially transverse event coordinates. The point made about manifold use of the history files applies in even stronger form here since different beam sizes are now fully correlated and thus intercomparison is greatly facilitated.) As mentioned in the Introduction, beams all have Gaussian profiles with $\sigma = \sigma_x = \sigma_y$. Twelve different beam sizes are simultaneously simulated ranging in size from 0.005 cm to 20 cm. Energy deposition is collected in a set of ring-shaped cells with their radii adjusted to each beam size, ranging in size from $r < 0.5\sigma$ to $15\sigma < r < 20\sigma$.

Contours of equal energy density in the z–r plane are presented in

Figs. 2–17. They are shown for two beam sizes, $\sigma = 0.15\,cm$ and $\sigma = 2\,cm$, for all four of the materials at $20\,TeV$, and for carbon and tungsten also at $1\,TeV$ and $10\,TeV$. The choice of these beam σ's reflects the beam sizes anticipated at the SSC beam abort dump. If beam is dumped at $20\,TeV$, and both the blow-up lens and spiral kickers fail, it would be roughly $\sigma = 0.15\,cm$ in size. If only the spiral kickers fail it would be about $\sigma = 2\,cm$ [24].

Maximum energy density as a function of z, i.e., the energy density on the beam axis, is shown in Figs. 18–25. Target materials and beam energies are the same as for the contour plots but here the entire gamut of beam sizes is included. The on-axis energy density is estimated using an algorithm which assumes that the radial distribution of the energy density is a superposition of a (slowly spreading) Gaussian beam plus a growing tail due to cascading. At low z the difference between ρ_E^{max} and $\bar{\rho}_E$ (averaged over the on-axis bin, $r < \sigma/2$) is predictable and small ($\sim 6\%$). At large z results begin to suffer statistically in the central r bins but there the algorithm serves to combine them in an improved estimate of ρ_E^{max}.

3.2 Beam Sweeping

The immediate utility of the results on the solid cylinders for beam dump questions is clear without further elaboration. The results are also useful, at an intermediate level, to calculate energy densities resulting from beam sweeping. (The formulae given below are applicable to segmented dumps as well.) Beam sweeping lowers the maximum energy deposition by means of kicker magnets with oscilllating fields which cause the beam spot to be swept, in various patterns, on the face of the dump. They are, e.g., part of the SSC abort beam dump design. A few remarks on this subject, with particular applicability to the results presented here, follow.

The dilution in ρ_E achieved via beam sweeping is calculated analytically from the Monte Carlo results much in the manner of Ijspeert and Stevenson [25], but adapted to the results generated here. Ref.[25] starts out with a pencil beam and uses the distribution

$$\rho_E = \frac{\rho_0}{1 + (r/a)^2} \tag{3}$$

which approximates the radial variation of ρ_E, as predicted by the FLUKA [26] program, at a depth corresponding to the maximum of the laterally integrated energy density, where ρ_0 and a also are fixed. The limitation to this particular depth is somewhat troublesome (though not so much for

application to dumping, see below). The procedure described here yields ρ_{E_s}, the energy density produced by the sweeping beam, at any depth, which is necessary for an accurate determination of the maximum ρ_{E_s} occurring in the target.

As mentioned above, ρ_E is fitted to a Gaussian plus a tail in the program. This provides the on-axis energy density, $\rho_0(z)$, as well as $\sigma(z)$, at all z

$$\rho_E = \rho_0 e^{-\frac{x^2+y^2}{2\sigma^2}} \tag{4}$$

with the arguments of ρ_0 and σ in Eq. 4 suppressed for clarity.

At low depth, the validity of Eq. 4 in the central region rests on the assumption of a Gaussian beam. At large z, small r, similarity with multiple scattering suggests that the small angle processes once again yield Eq. 4. It makes sense then to adopt Eq. 4 at all z. In the discussion below the tail at large r is ignored, i.e., it is assumed that Eq. 4 describes all of ρ_E. This is already quite accurate for finding $\rho_{E_s}^{max}(z)$. One approach to include the tail is to replace Eq. 4 by a sum of two or more Gaussians since the formulae given below readily generalize to that case. Generalization to beams with $\sigma_x \neq \sigma_y$ is likewise easily accomplished but likewise not done explicitly here. The different sweeping modes included here are directly borrowed from Ref. [25].

3.2.1 Linear Sweeping

Linear sweeping here means that the center of the Gaussian beam sweeps back and forth along a line of length L. The sweep velocity is constant, except at the turning points. This leads to an energy density

$$\rho_{E_s} = \frac{1}{L}\int_{\frac{-L}{2}}^{\frac{L}{2}} \rho_0 e^{-\frac{y^2+(x-\xi)^2}{2\sigma^2}}\, d\xi \tag{5}$$

where ξ is the coordinate of the beam's center. Integration yields

$$\rho_{E_s} = \frac{\rho_0\sqrt{2\pi}\sigma}{2L} e^{-\frac{y^2}{2\sigma^2}} \left[erf\left(\frac{L/2+x}{\sqrt{2}\sigma}\right) + erf\left(\frac{L/2-x}{\sqrt{2}\sigma}\right)\right] \quad . \tag{6}$$

For $L \gg \sigma$, which is the case of most interest, and for $|x| \ll L$, the erf's in Eq. 6 approach unity and

$$\rho_{E_s} = \frac{\sqrt{2\pi}\rho_0\sigma}{L} e^{-\frac{y^2}{2\sigma^2}} \quad . \tag{7}$$

From the geometry it is clear that ρ_{E_s} is maximal at $x = y = 0$. From Eq. 6

$$\rho_{E_s}^{max} = \frac{\sqrt{2\pi}\rho_0\sigma}{L} erf\left(\frac{L}{2\sqrt{2}\sigma}\right) \tag{8}$$

and for $L \gg \sigma$ either Eq. 7 or Eq. 8 yields

$$\rho_{E_s}^{max}(z) = \frac{\sqrt{2\pi}\rho_0(z)\sigma(z)}{L} \tag{9}$$

where the arguments of $\rho_{E_s}^{max}$, ρ_0, and σ are explicitly reintroduced to call attention to the z–dependence. For small L, the error functions in Eq. 6 can be expanded in series to describe ρ_{E_s}. For $L \ll \sigma$, $\rho_{E_s}^{max}$ approaches ρ_0 as expected.

3.2.2 Circular Sweeping

In circular sweeping the beam center is swept with uniform velocity along a circle of constant radius

$$\rho_{E_s} = \frac{\rho}{2\pi}\int_0^{2\pi} e^{-\frac{(r-R)^2)}{2\sigma^2}}\, d\phi \tag{10}$$

where R and ϕ are the sweeping radius and azimuthal angle. This integrates out to

$$\rho_{E_s} = \rho_0 I_0\left(\frac{Rr}{\sigma^2}\right) e^{-\frac{r^2+R^2}{2\sigma^2}} \tag{11}$$

where I_0 is the modified Bessel function of the first kind and zeroth order. The maximal ρ_{E_s} occurs for r given by the solution to

$$RI_1\left(\frac{Rr}{\sigma^2}\right) = rI_0\left(\frac{Rr}{\sigma^2}\right). \tag{12}$$

For $R \gg \sigma$, as would typically prevail, the Bessel functions approach each other asymptotically and $\rho_{E_s}^{max}$ occurs at $r = R$, as expected. By using the asymptotic formula for I_0, Eq. 11 becomes

$$\rho_{E_s} = \frac{\rho_0\sigma}{\sqrt{2\pi r R}} e^{-\frac{(r-R)^2}{2\sigma^2}} \simeq \frac{\sqrt{2\pi}\rho_0\sigma}{2\pi R} e^{-\frac{(r-R)^2}{2\sigma^2}} \tag{13}$$

i.e., linear sweeping along a circle of radius R, see Eq. 7, and the analogy applies to $\rho_{E_s}^{max}$ as well:

$$\rho_{E_s}^{max}(z) = \frac{\sqrt{2\pi}\rho_0(z)\sigma(z)}{2\pi R}. \tag{14}$$

For $Rr \ll \sigma^2$ the series expansion of the Bessel functions can be used to describe ρ_{E_s}. It is again easy to show that the maximum ρ_{E_s} approaches ρ_0 as $R \to 0$.

3.2.3 Spiral Sweeping

A spiral sweep, e.g., of the type proposed for SSC [1], can be approximated by a set of concentric circular sweeps with each circle contributing the same number of particles. In the limit of an infinite number of circles, the sum over circles becomes the integral of $\rho_E dR$ from R_1 to R_2, averaged over $(R_2 - R_1)$. Assuming $R_1 \gg \sigma$, Eq. 13 leads to

$$\rho_{E_s} = \frac{\rho_0 \sigma}{\sqrt{2\pi}\,(R_2 - R_1)} \int_{R_1}^{R_2} \frac{1}{\sqrt{rR}} e^{-\frac{(r-R)^2}{2\sigma^2}}\, dR. \tag{15}$$

From the geometry, $\rho_{E_s}^{max}$ is expected to occur close to the inner limit circle. To estimate $\rho_{E_s}^{max}$, r is replaced by R_1 in Eq. 15 and, since most of ρ_{E_s} at R_1 derives from beam at nearby R, it is only a slight overestimate to replace $\sqrt{R_1 R}$ in the denominator of Eq. 15 by R_1 as well. Then

$$\rho_{E_s}^{max} = \frac{\rho_0 \sigma^2}{2R_1\,(R_2 - R_1)} erf\left(\frac{R_2 - R_1}{\sqrt{2}\sigma}\right). \tag{16}$$

If $(R_2 - R_1) \gg \sigma$, as is needed for effective dilution, $erf\left(\frac{R_2 - R_1}{\sqrt{2}\sigma}\right) \sim 1$ and

$$\rho_{E_s}^{max}(z) = \frac{\rho_0(z)\sigma^2(z)}{2R_1\,(R_2 - R_1)}. \tag{17}$$

Given R_2, the maximal excursion, the question arises for what R_1 is $\rho_{E_s}^{max}$ a *minimum*. It is easily derived from Eq. 17 that this occurs at $R_1 = R_2/2$ where $\rho_{E_s}^{max} = \frac{\rho_0(z)\sigma^2(z)}{2R_1^2}$.

3.2.4 Depth Dependence

It is interesting to further explore the depth dependence of $\rho_{E_s}^{max}$ for the different sweeps. The final expressions for each case indicate the way that the shape of the depth dependence is altered from $\rho_0(z)$ itself, by the depth dependence of $\sigma(z)$ ($\sigma\rho_0$, for linear/circular— and $\sigma^2\rho_0$, for spiral sweeps). The effect will thus be more pronounced for smaller beams, heavier targets, and for spiral vis-a-vis linear/circular sweeping.

Fig. 26 shows, by way of illustration, ρ_E^{max} ($\equiv \rho_0$), in relative units, for

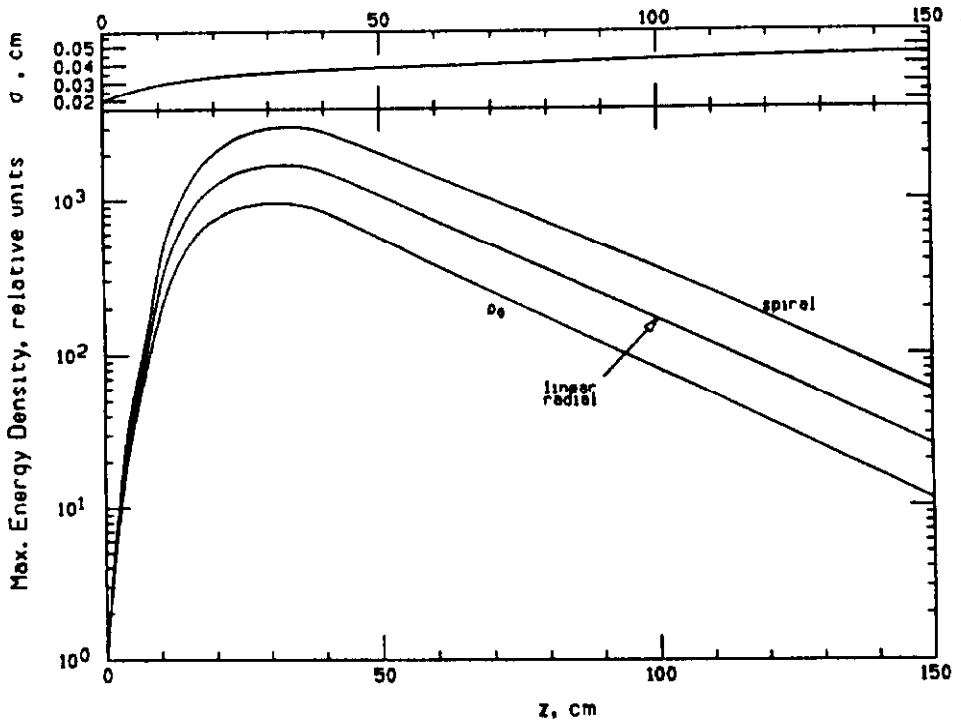

Figure 26: (bottom)-Relative depth dependence of ρ_E^{max} for Gaussian beam with $\sigma = 0.02cm$, and for linear and spiral sweeps. (top)-Depth dependence of σ associated with energy deposition.

a Gaussian beam of $\sigma = 0.02\ cm$ (see Fig. 22) as a function of z along with ρ_E^{max} for a linear/circular sweep ($\propto \sigma\rho_0$), and for a spiral sweep ($\propto \sigma^2\rho_0$). The variation of σ with depth is shown on the top of Fig. 26. (This is the sigma of a single Gaussian fit to ρ_E for $0 < r < 2.5\sigma$ and is meant for illustrative purposes only. The description would no doubt improve if one were to use a sum of Gaussians for the radial dependence.) The difference in depth dependence of the sweeps is clearly noticeable. Fig. 26 also exhibits a potential difficulty with the approach of [25]. The depth at which to find the overall $\widetilde{\rho}_{E_s}^{max}$ depends upon the sweeping mode and does not coincide with the depth dependence of the laterally integrated energy density, which peaks at still larger z than the curves of Fig. 26. Using a fit at the maximum of the integrated ρ_E overestimates the radial spread and underestimates the peak energy deposition. That $\rho_{E_s}^{max}$ has a depth dependence intermediate between ρ_0 and the laterally integrated one is not surprising since the latter is equivalent to that of a beam *uniformly* distributed over a large area, something which is *not* accomplished by the sweeping modes included here: for a linear/circular sweep only one dimension of the beam is spread out and even for a spiral sweep the particle density is still nonuniform (denser at

small radii). For typical beam dumping, the errors made by assuming $\rho_{E_z}^{max}$ and the lateral integral of ρ_E peak at the same z will not be large (10–20%). Details of depth dependence are apt to be much more significant in targetry problems [27]. The present approach, based on Gaussian distributions, is quite well suited to such problems. For more complicated beam distributions and/or sweeps the approach, mentioned above, of treating simultaneously a set of Gaussians with differing σ, can obviously be extended to sweeping.

3.3 Segmented Targets

The geometry for this case consists of a set of plates separated by gaps and followed by a solid dump. All of the plates as well as the dump are of the same material. As with the solid cylinders, a single computer run simultaneously treats several beam sizes ($\sigma = 0.02, 0.05, 0.15, 0.5, 2.0$, and $10\,cm$). In a similar vein, four positions of the solid dump can be simultaneously superposed on the same configuration of plates and spacings, again with savings in computing time and enhanced statistical discrimination, as pointed out in connection with the history files and parallel treatment of beam distributions. The geometry studied here is quite primitive considering the vast array of options available by varying, within the same geometry, plate thickness, plate spacing, and material composition. The choices made here reflect mostly convenience and ease of interpretation.

3.3.1 *Calculations*

For this geometry, results from one computer run for each of the four materials are reported here. For carbon and aluminum the plate thickness chosen is $2\,cm$, while for iron and tungsten it is $1\,cm$. The distance from the front of each plate to the front of the next one is always $1\,m$. Solid dumps begin after $50, 100$, and $150\,m$ for carbon and aluminum, after $40, 80$, and $120\,m$ for iron, and after $15, 30$, and $45\,m$ for tungsten. As a cross-check with the cylinder results, a solid dump is also started at zero depth. Only results for beam σ's of 0.15 and $2\,cm$ are presented here. Figs. 27-34 show the maximum energy density as a function of depth into the array. For convenience depth is expressed in g/cm^2 of the material (thus skipping over the gaps) and with all discontinuities in ρ_E^{max} smoothed out. The pattern is the same in all of the graphs: the upper curve corresponds to ρ_E^{max} for a solid dump and the lower one to ρ_E^{max} for a completely segmented dump. The in-between curves, launched at regular intervals from the lower one, correspond to the solid dumps starting at that depth. It can be readily determined from such

curves at what depth in the array a solid dump can be placed so that ρ_E^{max} in the dump does not exceed ρ_E^{max} in the array.

3.3.2 Practical Implications

The segmented dump case, along with the oblique incidence geometry, aspires to lower $\widetilde{\rho}_E^{max}$ significantly and are thus applicable, at least in principle, to the problem of dumping. The virtues of a passive versus an active dump, i.e., one with magnets (or at least electro-magnets) for blowing up and/or sweeping, must somehow be factored in when assessing the difficulties associated with these odd-ball geometries.

The results indicate that, while substantial reductions in $\widetilde{\rho}_E^{max}$ are possible, the structures must become uncommonly long to be worthwhile. For example, Fig. 21 shows that a reduction in $\widetilde{\rho}_E^{max}$ by a factor of ~ 200 (roughly the ratio of the maxima of the upper and lower curves) is possible for carbon with the arrangement studied there. Unfortunately, a solid dump cannot start until well off-scale, i.e., only after several hundred meters of the array. Since there must be a sufficiently thick mantle of iron and/or concrete surrounding the plates to contain induced radioactivity, this appears uneconomical. Perhaps a shorter (denser) array with a lesser reduction in $\widetilde{\rho}_e^{max}$ is still worth contemplating. The calculation for aluminum uses the same geometry as carbon so that Figs. 21 and 23, as well as Figs. 22 and 24, are directly comparable. For aluminum with the solid dump starting at $150\,m$, the peak in the dump is comparable to the peak in the plates. However, $\widetilde{\rho}_E^{max}$ is, in both cases, ~ 5 times higher for the aluminum and one needs to go to a larger spacing to match the $\widetilde{\rho}_E^{max}$ in carbon. Glasses and ceramics, which might be the material of choice for such a dump, can be approximated by aluminum when corrected for density.

3.4 Oblique Incidence

The variation of the energy density distribution in the target with angle of incidence of the beam is briefly examined. That there is a variation with angle, other than the trivial one connected with a coordinate rotation, is made plausible with the help of Fig. 35. The same beam of (monoenergetic, parallel incident) particles is shown (in superposition) to strike two targets, one at right angles and the other at a relatively shallow angle θ. For simplicity, neglect all radial spreading of the beam particles or of the internuclear cascades they induce, so that all energy is deposited along a straight line. Each such trajectory can be imagined to represent a large

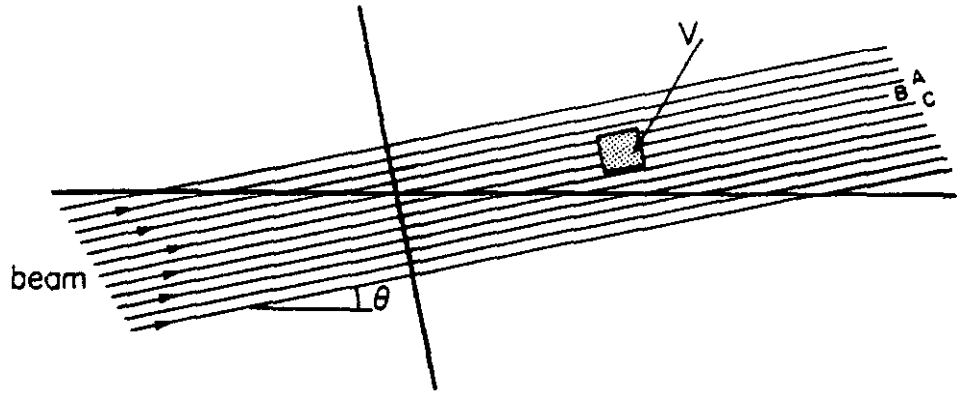

Figure 35: Beam striking target at small angle θ superposed on normal incidence (for which energy density peaks in elementary volume V).

number of incidents which justifies using the average (laterally integrated) energy deposition along each track, shown schematically in Fig. 36. For perpendicular incidence, the maximum energy density along each trajectory occurs at the same depth (distance from surface) as indicated in Fig. 35 by the location of the small volume, V. For oblique incidence the energy density along ray B (shown crossing V) is the same, but along A and C it is no longer in step (see Fig. 36) and the energy deposited in V is reduced. This picture also illustrates that to be effective $\theta <\sim \sigma/\Delta$ where σ is the beam size and Δ represents the width of the laterally integrated density which points to rather small θ's. At very small θ there is additionnal reduction of the energy density when leakage of particles out of the front face becomes significant. This happens when θ becomes comparable to the angle of emission of secondaries in the cascade.

While leaving the conclusion intact, the radial spread of the cascade and a nonuniform distribution of the beam considerably complicate the above picture and discourage the use of simple geometric arguments to convert data or predictions valid for perpendicular incidence to the oblique case (or to interrelate results for different theta). Instead energy densities are explicitly calculated for oblique incidence at a number of angles. From inspection of the results some *approximate* scaling rules then re-emerge along with some perception of their accuracy and their domain of validity.

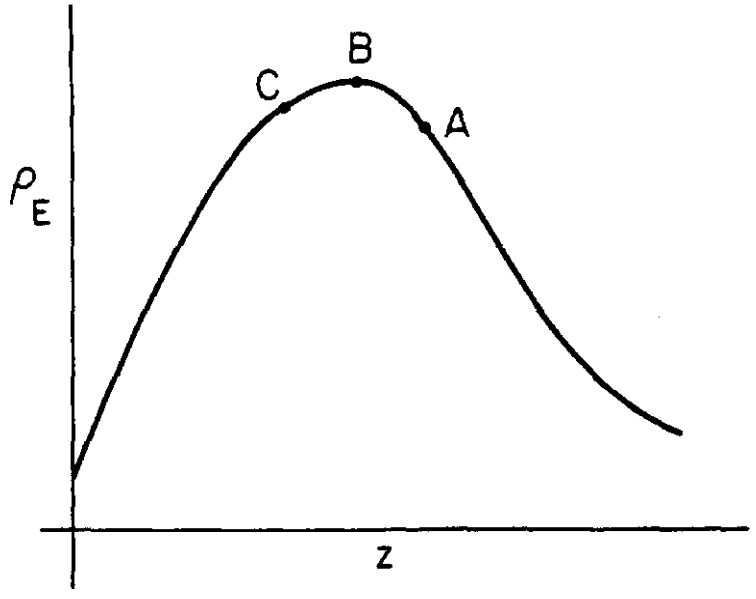

Figure 36: On average, rays A, B, and C all peak at the same depth for perpendicular incidence, at different depths for oblique incidence.

3.4.1 Calculations

The results presented here are intended as illustrations and not as a systematic exploration of the subject. The target is assumed to be solid and homogeneous. The calculation is run simultaneously for several beam σ's as in the case of perpendicular incidence. The geometry suggests collecting the energy deposited in prism-shaped cells as shown in Fig. 37. In the plane perpendicular to the target face and containing the beam axis, the x_b-axis is perpendicular to the beam axis (z_b) and points out of front face of the target. The y-axis completes an orthogonal system with x_b and z_b. This system is now replaced with an oblique coordinate system wherein the axis z_t, perpendicular to the target face, replaces the z_b axis, and the prism walls are the planes of constant $x(\equiv x_b)$, constant y, and constant z_t. For convenience, all cells have identical dimensions. The x and y dimensions are adjusted according to beam size while the length of the slices along z_t are chosen inversely proportional to the incident angle, i.e., constant steps along z_b. In accordance with Fig. 37, x is measured from the yz_b plane with positive x pointing out of the front face of the target.

The resulting energy deposition is symmetric in the y variable and this is exploited by sorting on $|y|$ only. This is not the case for x as illustrated for the case of a $\sigma = 0.15\,cm$ beam of $20\,TeV$ protons incident on aluminum at an angle of 0.001 *rad*. Fig. 38 shows contours of equal energy deposition

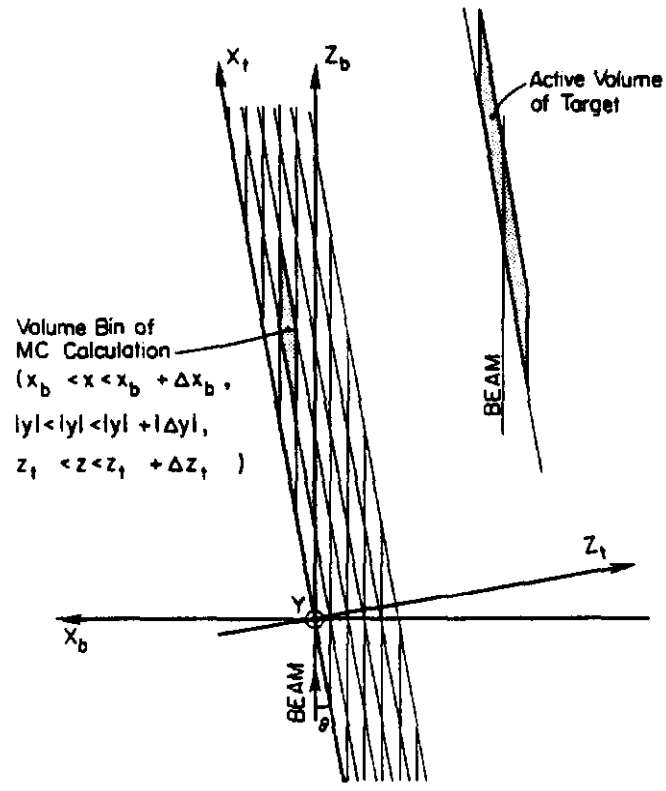

Figure 37: Binning scheme for oblique incidence. Target thickness along z_t changes with angle of incidence, θ, but remains the same along z_b.

in the *top* slice ($0 < z_t < 0.04\,cm$, i.e., the first $40\,cm$ along the beam) of the target and reveals a clear bias toward positive x. This is not surprising if one considers the contributions to ρ_E due to lower energy particles, exemplified by broad and isotropic angular distributions in the lab. From Fig. 37 it is easy to see that, in the top layer of the target, the bins at positive x lie much closer to the beam axis than those at negative x. In the ***bottom*** slice, ($0.36 < z_t < 0.40\,cm$) and under the same beam/target conditions, Fig. 39 shows that the situation is reversed which is likewise to be expected from the geometry. Also for this same case, Fig. 40 shows how the shift takes place as a function of z_t in the form of a contour map of ρ_E in the $y = 0$ plane, where $\rho_E(y)$ is expected to peak. These observations may lead to questions about the peculiar binning scheme of Fig. 37. However, this scheme has the advantage of simple (and automatic) adaptation to change in angle and beam width. It also leads to easy evaluation of the maximum energy deposition, both as to its value and its location within the target.

Since $\widehat{\rho}_E^{max}$ for the entire target appears to be the most important datum for a given material, incident angle, and beam spread, the results can be summarized compactly, as in Fig. 41 for $20\,TeV$ protons on aluminum. This presents $\widehat{\rho}_E^{max}$ for four different beam sizes as a function of incident angle,

and illustrates the rather small angles required before any gain is made. At the very small angles there is an important caveat. The target thickness assumed for the (aluminum) target of Fig. 41, is (for all θ) 400 cm along the beam direction, which, e.g., for $\theta = 10^{-6}$ reduces to a thickness of $4 \cdot 10^{-4}$ cm. This is not only impractical in an experimental sense but also strains the energy deposition model of the calculation, e.g., certain 'local' deposition mechanisms become diffuse on so small a distance scale. These complications are not further pursued here.

Some results for 20 TeV protons on iron are shown in Figs. 42–45. The depth dependence of ρ_E^{max} for each of the various angles and for a beam of $\sigma = 0.15$ cm is shown in Fig. 42, and for $\sigma = 10$ cm in Fig. 43. The maximum energy densities for the entire target are summarized in Fig. 44 which presents $\widehat{\rho}_E^{max}$ for four different σ's as a function of angle. The trends are quite similar to the aluminum case and suggest use of the scaling variable θ/σ^2 as demonstrated in Fig. 45, where $\widehat{\rho}_E^{max}$ is seen to vary linearly with this variable over a large range of σ and θ.

Fig. 46 illustrates the energy dependence connected with oblique incidence. It shows results similar to Fig. 44 (and Fig. 41) but for the case of 1 TeV protons on iron. As expected at this lower energy, the angles need not be quite as small before $\widehat{\rho}_E^{max}$ is significantly lowered. Deviations from scaling are also obvious at the smallest incident angles and are probably connected to the relative importance of the various energy deposition mechanisms. The caveat concerning the small angle results, mentioned above, applies here as well.

3.4.2 Practical Implications

As already remarked, for intentional beam dumping the small angles of incidence required before $\widehat{\rho}_E^{max}$ is substantially lowered, tend to preclude much practical use. Furthermore the angular dispersion of the beam, which has been neglected here, becomes significant in comparison with such small angles. But perhaps some variation of this geometry may succeed, e.g., a *long pipe with a very slight bend or taper (situated in a larger structure)* could avoid some of the steering problems associated with the small angles. This could possibly be combined with the notion of segmented beam dumps by introducing suitably spaced foils or plates into the pipe to speed dispersal of the beam. Contrasting the 1 TeV and 20 TeV results suggests examining oblique incidence at yet lower energy although conventional beam dumps do not pose a problem there, at least at present day intensities.

For accidental beam dumping the small angle oblique incidence geometry may provide a starting point, since this will be the prevalent condition when beam is lost inside the aperture. In actuality, particles hitting the beampipe wall will seldom fit the description adopted here (Gaussians with $\sigma_x = \sigma_y$ and with, for all particles, $x' = \theta, y' = 0$). But while serious calculations need sufficient detail about the beam in phase space (see, e.g., Ref.[28]) this may be quite difficult to ascertain unless one can identify the dominant beam loss mechanism(s). In the absence thereof one may try and bracket the maximum energy deposition using the Gaussians (or a superposition of Gaussians with different θ and σ).

Appendix

A number of comparisons of CASIM with experiment and other calculations [4,10,29] already exist. Here, CASIM results are compared with experiments [7] at 300 GeV and with calculations [6] at 20 TeV. CASIM, along with some other calculations [12], has already been compared with the data of Muraki et al. [7] but since the methodology of [12] is debatable, the CASIM comparison is repeated here. Comparisons with other predictions is limited to the calculations of Mokhov which appear to be the only published results in the 20 TeV regime directly comparable to the ones presented here. More complete intercomparisons would certainly be worthwhile.

The paper of Muraki et al. describes a classic beam dump experiment wherein 300 GeV protons strike an *iron* dump, about 75 cm long and consisting of a series of slabs ranging in thickness from 2.5 cm at the front to 15 cm for the bulk of the dump. X-ray films are placed in 0.5 cm wide slots separating the slabs. The photographic density of the irradiated film is taken as a measure of energy deposition. At each slot (z–location) the energy deposition is reported at radii $r = 0, 1, 2, 4, 8, 10$, and 12.5 cm. The incident beam is described by a fairly narrow peak (with a diameter of 0.18 cm at half its maximum) plus a substantial tail ('possibly due to muons' [7]) extending beyond 3.5 cm. The experiment is repeated in identical geometry but with *lead* as the target material. The energy densities are quoted in arbitrary units.

In [12] calculated results of CASIM, FLUKA [26], and GEISHA [30], obtained for homogeneous targets, are compared with the Muraki et al. experiment. The comparison is limited to the $r = 1, 4$ and 12.5 cm data. For the iron plates, the normalization problem is taken care of by fitting ('by

eye' [12]) the $r = 1\ cm$ data to the calculations. (For lead, their procedure is less clear [31].) As Ref. [12] concludes, the comparison is certainly more flattering to FLUKA and GEISHA than to CASIM. This is not surprising since this holds true already for the results in the iron at $r = 1\ cm$ where they are 'normalized'. In addition to this arbitrariness, the comparisons of Ref. [12] are carried out in a location where ρ_E is down a factor of ~ 20 from $\widehat{\rho}_E^{max}$ which makes them even less germane to the present main concern, viz., estimating $\widehat{\rho}_E^{max}$ in a thick target [32]. Mokhov [6,13] offers a more complete comparison, including a faithful simulation of the geometry, and normalizes the data to his calculated result at $z = 0, r = 0$ [33]. The same simulation and normalization procedure is followed here, using CASIM. The energy density of $\sim 0.16\ GeV/cm^3$ predicted in the emulsion at $z = 0, r = 0$ (and practically independent of target material) agrees well with [6]. But the procedure is not completely free of difficulties since the normalization question is closely tied to the assumed beam shape and this involves some arbitrary choices made in the simulation. Based on [7] the calculation assumes a Gaussian beam profile ($\sigma_x = 0.076\ cm$) plus a tail which is supplied numerically and is based on Fig. 3 of [7] for $x > 1.5\sigma$. No information is given for radii above $3.5\ cm$, but instead of an abrupt cut-off the beam profile is assumed to decline linearly to zero at $x = 5\ cm$. An identical distribution in y is assumed. All particles, peak and tail, are assumed to be $300\ GeV/c$ protons with $x' = y' = 0$.

Because of the superior experimental resolution ($\leq 0.1 mm$), smaller than the beam width, an average over some relatively large radius is unacceptable if one wishes to compare with the reported $r = 0$ results. Instead the maximum energy density on axis is estimated using a radial subdivision of $\Delta = 0.025\ cm$ at small radii. At the larger r, where there is less radial variation of the energy density, Monte Carlo results are averaged over $\Delta r's$ ranging from 0.5 to $3\ cm$. The $z = 0, r = 0$ result especially (and hence overall normalization), but all other results as well, is quite sensitive to detail regarding the incident beam. The $r = 0$ predictions are most sensitive to the assumptions about the peak, while those about the distribution of the tail have more effect elsewhere [34].

In addition to the radial binning and beam distribution, special measures are introduced to cope with the relatively small thickness of the X-ray film packs. Ordinarily, when the entire volume serves as detector, it suffices to deposit the energy associated with a given process at a finite number of locations along a, somewhat idealized, particle trajectory. In the present geometry only a few such events would fall within the active volume, causing

the calculation to converge too slowly. To boost the statistical impact of such a trajectory, it is traced boundary to boundary but with the essential physical approximations of the method preserved. Where it crosses (or stops in) an active volume an amount of energy proportional to the length of the trajectory in that volume is deposited, consistent with the condition that for an infinitely long run the results should be the same as those of a regular CASIM calculation.

Results of the calculation are shown in Fig. 47. Statistical problems remain, even after inclusion of the above refinement. (The calculated points of Fig. 47 are based on 10^5 incident particles.) There is a marked tendency (outside of the $r = 0$ results, where they are normalized) to underestimate the data at low z while agreeing much better deeper into the target. This is also observable in [6] and could be related to incomplete knowledge of the incident beam. For instance, to check the importance of the tail, energy densities are calculated (in parallel with those for the full distribution) for the Gaussian component only. These energy densities are suppressed by $\sim 10 - 20\%$ not only at radii corresponding to the tail but also at larger r. One could imagine larger differences if, e.g., the particles in the tail are lower energy hadrons or have a large angular divergence, or if allowance were made for the presence of neutrons and/or photons. It should also be noted that the energy density at large radii is substantially intermediated by low energy neutrons which are admittedly treated rather cursorily in CASIM. Since, at large r, energy densities at low z are much smaller than at large depths, even small changes in the magnitude or range of this diffuse component could dramatically improve the low z comparison, yet leave agreement intact at large z. The fits of the on-axis ρ_E are excellent at low z—up to the peak. Thereafter the Monte Carlo tends to increasingly overestimate the experiment. Empirically, the comparison at low z benefits more from the normalization at $z = 0$ so the better agreement there is not surprising. The discrepancy at large z could be interpreted as a manifestation of the 'leading particle surplus' quoted earlier [13], though it is then somewhat surprising that Ref. [6] has much the same problems. It should be pointed out in this respect that the more accurate treatment of δ-rays, implemented recently into CASIM (Sec 2.2), noticeably improves the comparisons at $r = 0$, which is especially important if one is to succeed in predicting ρ_E^{max}. Note also that, since the beam energy of 300 GeV is less than the 600 GeV cut-off, only 'old' CASIM enters in this comparison.

Fig. 48 compares results of present calculations with those of MARS10 [6] on the energy density along the beam axis in various targets produced by

$20 TeV$ proton beams of $\sigma = 0.05 cm$ and $\sigma = 0.2 cm$, respectively. Agreement is quite good, with the predicted $\widetilde{\rho}_E^{max}$ almost identical in all cases. The comparison is quite limited in extent but covers the most interesting region from the viewpoint of beam dumping, targetry, etc., and the agreement brings a measure of credibility to both calculations with regards to these applications.

References

[1] Conceptual Design of the Superconducting Super Collider, SSC Central Design Group, J. D. Jackson, Ed. (1986).

[2] A. Van Ginneken, P. Yurista and C. Yamaguchi, *Shielding Calculations for Multi-TeV Hadron Colliders*, Fermilab FN-447 / SSC-106 (1987).

[3] While the Fermilab Tevatron has long been operational the information at $1 TeV$ may be of use in connection with experiments and upgrades.

[4] A. Van Ginneken, *CASIM. Program to Simulate Hadronic Cascades in Bulk Matter*, Fermilab FN-272 (1975).

[5] A. Van Ginneken, *AEGIS. A Program to Calculate the Average Behavior of Electromagnetic Showers*, Fermilab FN-309 (1978).

[6] N. V. Mokhov, Yadern. Fiz. **18**, 960 (1980).

[7] Y. Muraki et al., Nucl. Inst. Meth. **A236**, 47 (1985).

[8] A. Van Ginneken, Phys. Rev. D **37**, 3292 (1988).

[9] S. Qian and A. Van Ginneken, Nucl. Inst. and Meth. **A256**, 285 (1987).

[10] M. Awschalom et al., Nucl. Inst. Meth. **138** 521 (1976); J. D. Cossairt et al., Nucl. Inst. Meth. **197** 465 (1982); J. D. Cossairt et al., Nucl. Inst. Meth. **A238** 504 (1985).

[11] M. Awshalom et al., Nucl. Inst. Meth. **131** 235 (1975).

[12] F. Ebeling et al., *Simulation of Hadronic Showers with Monte Carlo Codes. Comparison with Data and First Application to the Design of the Hera Beam Dump.*, DESY Rept. No. 87-057 (1987).

[13] N. V. Mokhov, *Inclusive Simulation of Hadronic and Electromagnetic Cascades in the SSC Components*, Appendix 19 of *Radiation Levels in the SSC Interaction Regions*, D. E. Groom, Ed., SSC-SR-1033 (1988).

[14] R. Hagedorn, Suppl. Nuovo Cim., **3**, 147 (1965); R. Hagedorn and J. Ranft, Suppl. Nuovo Cim., **6**, 169 (1968); J. Ranft, *Secondary Particle Spectra According to the Thermodynamical Model. A fit to Data Measured in p-Nucleus collisions*, TUL-36, Karl Marx Univ., Leipzig, DDR (1970). An empirical high-p_T term is added to the Hagedorn-Ranft predictions. Spectra of low energy nucleons are modeled by: J. Ranft and J. T. Routti,*Hadron Cascade Calculations of Angular Distributions of Secondary Particle Fluxes from External Targets and Description of the Program FLUKU*, CERN-II-RA/72-8 (1972).

[15] S. Frederiksson et al., Phys. Rep. **144**, 187 (1987).

[16] F. E. Paige and S. D. Protopopescu, BNL Report No. 38034 (1986).

[17] J. Ranft et al., *DTUJET. Dual Topological Unitarization of Soft and Hard Hadronic Processes: Predictions of a New Monte Carlo Event Generator for Beam-Beam Collisions at* $\sqrt{s} = 40\,TeV$, Appendix 3 of *Radiation Levels in the SSC Interaction Regions*, D. E. Groom, Ed., SSC-SR-1033 (1988).

[18] D. S. Barton, Phys. Rev. D **26**, 2580 (1983).

[19] B. Alper et al., Nucl. Phys. **B100**, 237 (1975).

[20] G. Arnison et al., Phys. Lett. **118B**, 167 (1982).

[21] A. Van Ginneken, Nucl. Inst. and Meth. **A251**, 21 (1986).

[22] see e.g., *Review of Particle Properties*, M. Aguilar-Benitez et al. Phys. Lett. **170B**, 1 (1986).

[23] N. V. Mokhov and A. Van Ginneken, *Calculations of Energy Deposition in High Energy Accelerator Targets* Fermilab TM-977 (1980).

[24] M. Harrison, private communication. According to design, with both lens and kickers operative the combined beam size and offset is of the order of 40 *cm* (see [1]).

[25] A. Ijspeert and G. Stevenson, *Formulae for the Calculation of Energy Deposition Densities in the Graphite Dumps of the LHC at a Proton Momentum of 10 TeV/c* CERN Report TIS-RP/TM/87-22 (1987).

[26] P. A. Aarnio et al., *A Long Write-up of the FLUKA82 program*, CERN ReportTIS-RP/106 (1983) and TIS-RP/129 (1984).

[27] C.M. Bhat and N.V. Mokhov, *Calculation of Beam Sweeping Effect for the Fermilab Antiproton Source*, FNAL-TM-1585 (1989).

[28] A. Van Ginneken, D. Edwards and M. Harrison, Fermilab-Pub-87/113 (1987).

[29] N. V. Mokhov and J. D. Cossairt, Nucl. Inst. Meth. **A244**, 349 (1986).

[30] H. Fesefeldt, preprint TH Aachen, PITHA-85-02 (1985).

[31] The statement in [12] that the data are fitted to the Monte Carlo 'at $r = 1$ *cm* in iron without changing the relative magnitude of the data for different radii and materials' is somewhat puzzling since the scale factors of Figs. 1a and 1b of [12] relative to Fig. 4 of [7] are obviously not identical. (Perhaps the lead data are adjusted by the ratio of the densities of lead and iron.)

[32] At very large radii, the preferred method for studying energy deposition with CASIM is to relate star density to *rad* (or *gray*) [A. Van Ginneken and M. Awschalom, *High Energy Particle Interactions in Large Targets*, Fermilab, Batavia IL (1975).] This assumes that the hadronic part of the shower dominates and that the energy spectra of the participating particles (mostly neutrons) are equilibrium spectra.

[33] Note that in Fig. A19-1 of [13] the calculations of [12] (CASIM and GEISHA only) are reproduced unchanged in their 'normalization' with respect to the Muraki et al. data.

[34] Ref. [7] does not specify that the beam is Gaussian (for small r) and their Fig. 3 lacks sufficient resolution in the peak region to be of direct use.

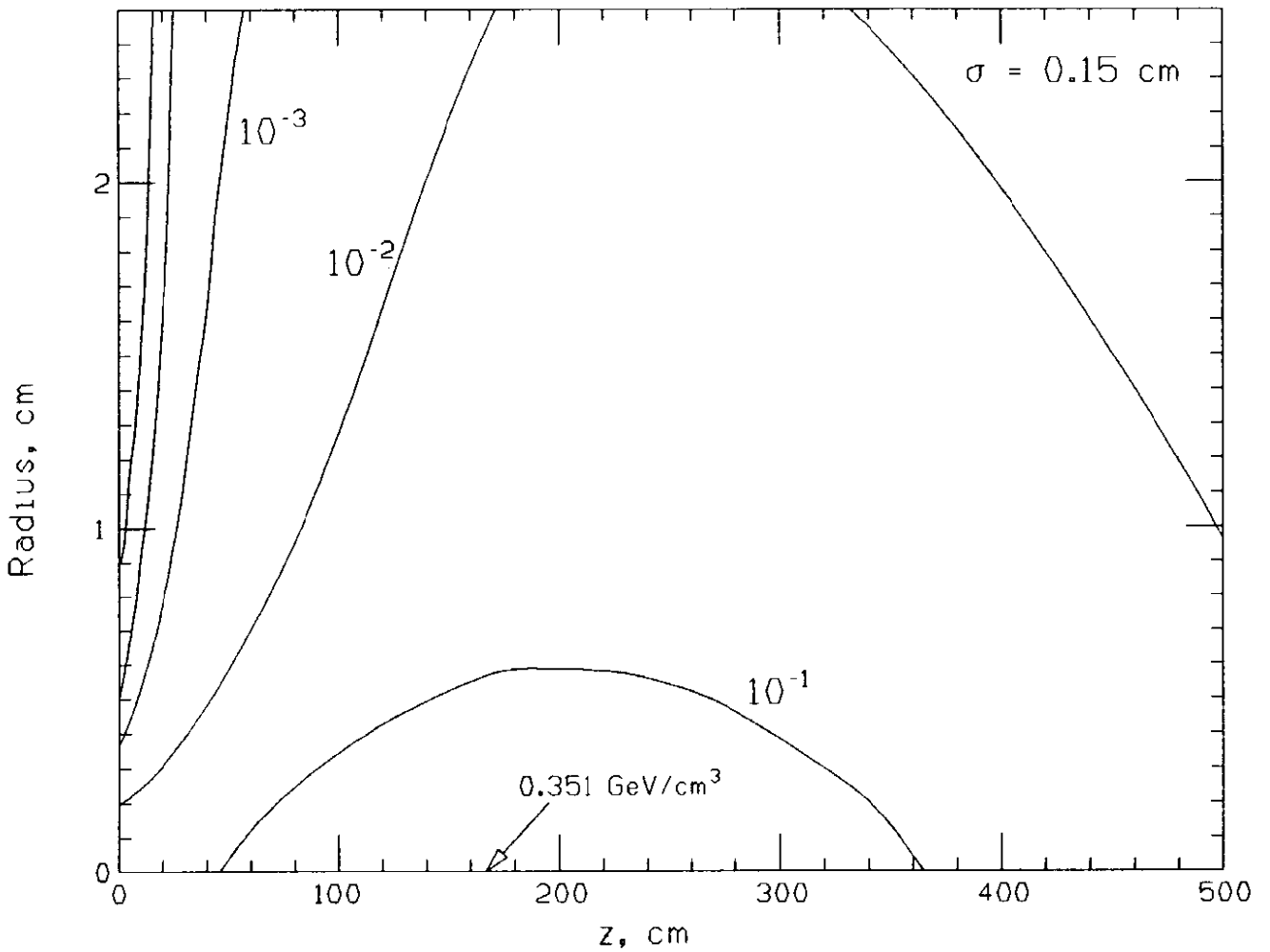

Figure 2: Contours of equal energy density for $\sigma_x = \sigma_y = 0.15\,cm$ Gaussian beam of $1\,TeV$ protons incident along axis of solid Carbon cylinder. Value and location of maximum energy density is indicated.

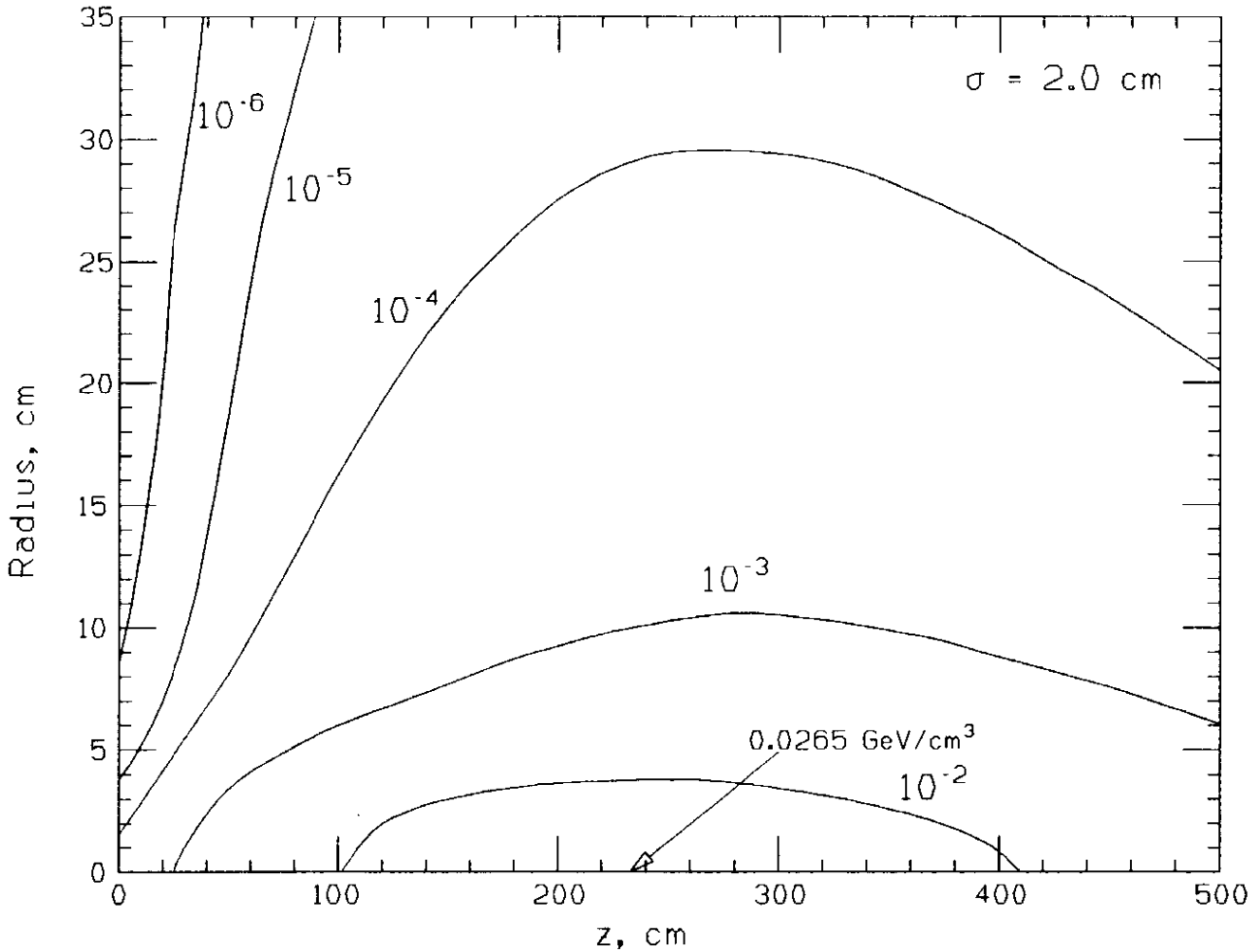

Figure 3: Contours of equal energy density for $\sigma_x = \sigma_y = 2\,cm$ Gaussian beam of 1 TeV protons incident along axis of solid Carbon cylinder. Value and location of maximum energy density is indicated.

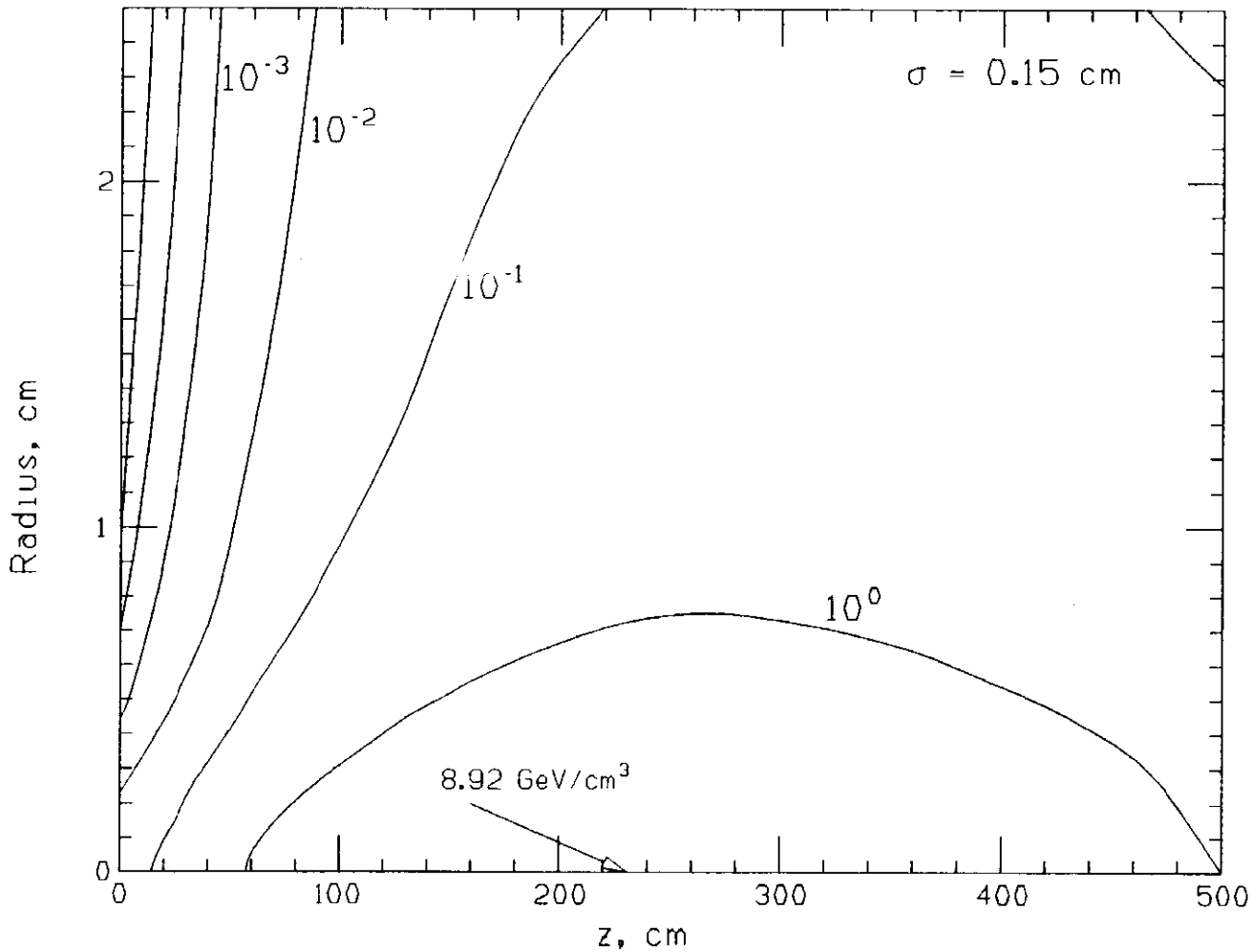

Figure 4: Contours of equal energy density for $\sigma_x = \sigma_y = 0.15\,cm$ Gaussian beam of $10\,TeV$ protons incident along axis of solid Carbon cylinder. Value and location of maximum energy density is indicated.

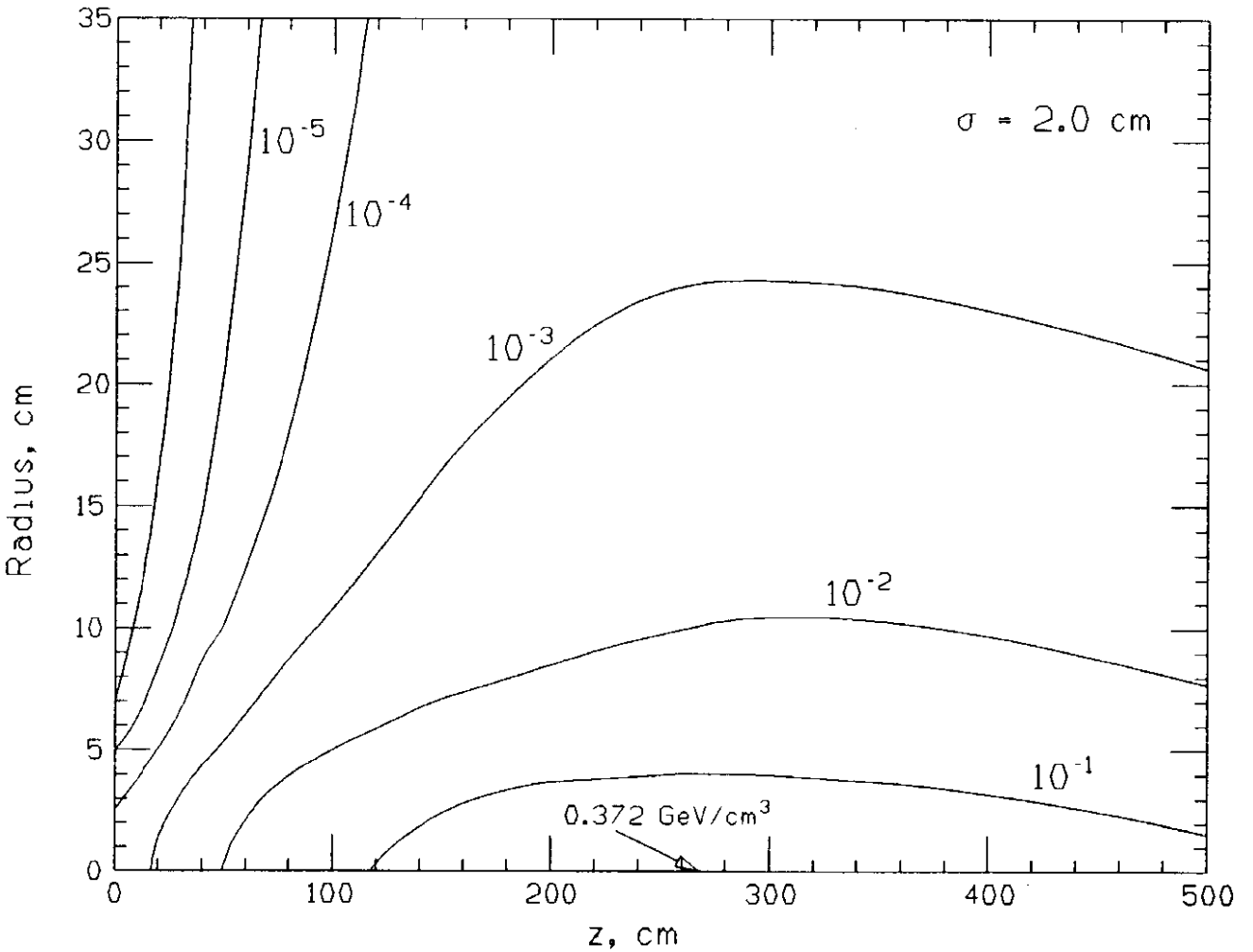

Figure 5: Contours of equal energy density for $\sigma_x = \sigma_y = 2\,cm$ Gaussian beam of $10\,TeV$ protons incident along axis of solid Carbon cylinder. Value and location of maximum energy density is indicated.

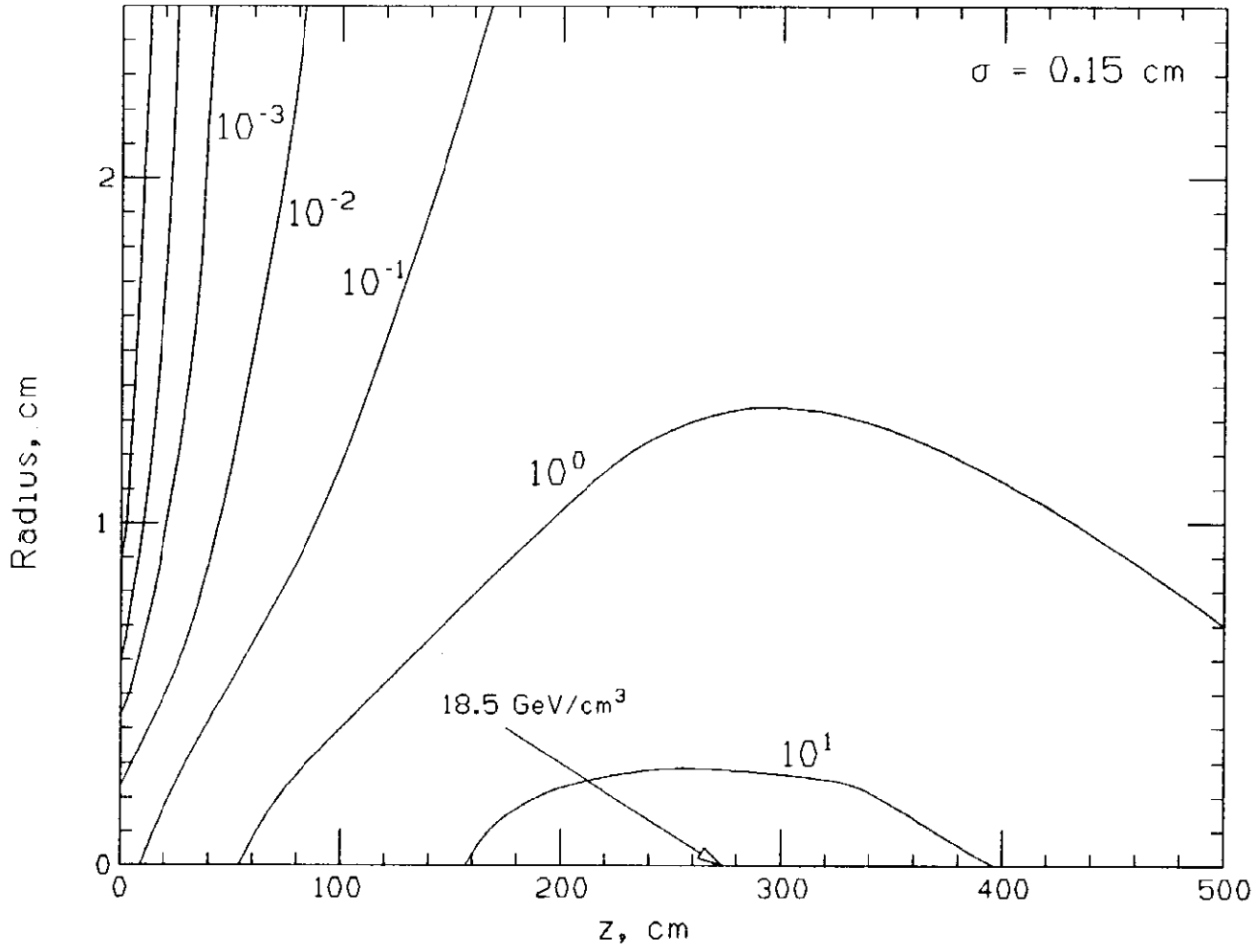

Figure 6: Contours of equal energy density for $\sigma_x = \sigma_y = 0.15\,cm$ Gaussian beam of $20\,TeV$ protons incident along axis of solid Carbon cylinder. Value and location of maximum energy density is indicated.

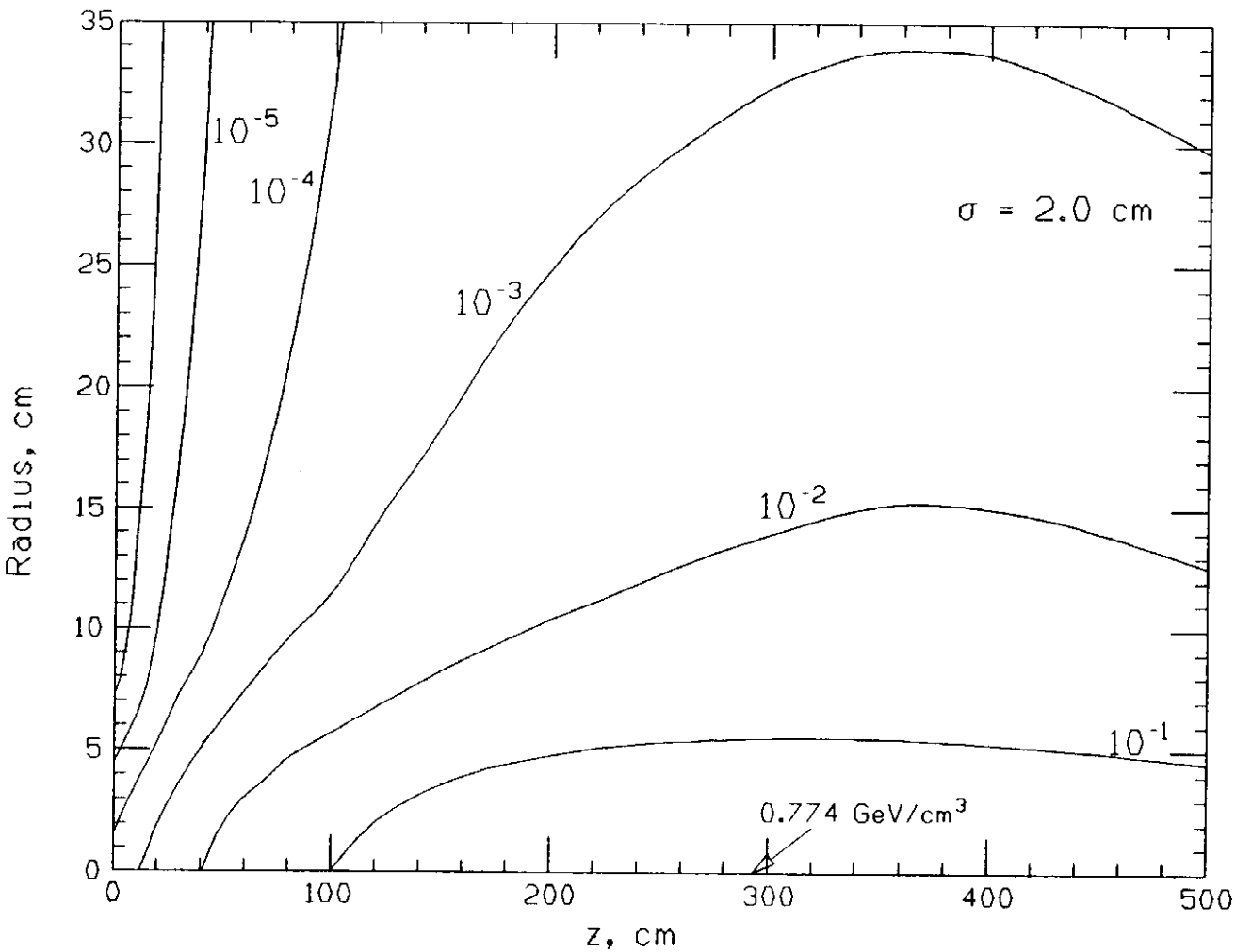

Figure 7: Contours of equal energy density for $\sigma_x = \sigma_y = 2\,cm$ Gaussian beam of 20 TeV protons incident along axis of solid Carbon cylinder. Value and location of maximum energy density is indicated.

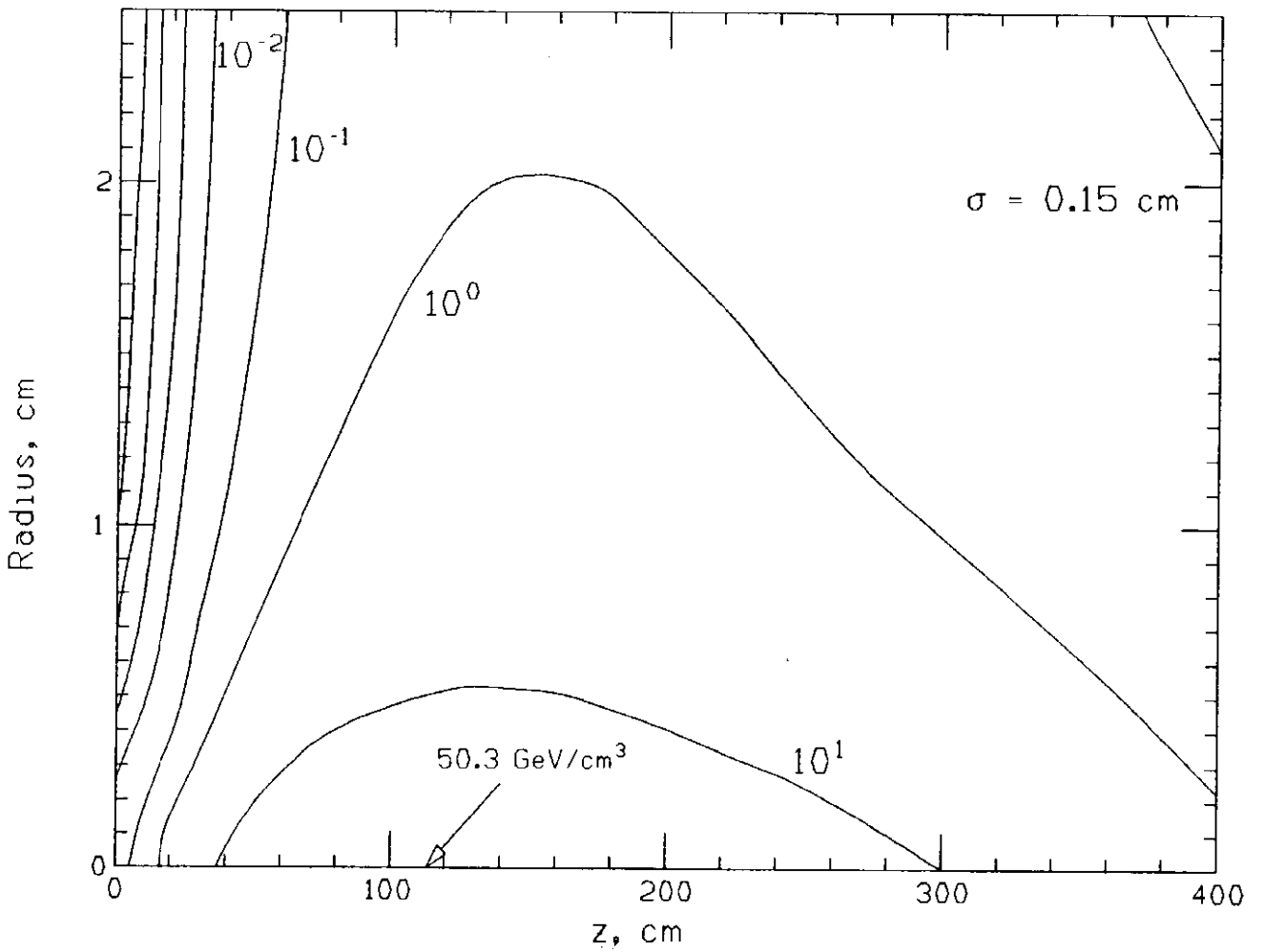

Figure 8: Contours of equal energy density for $\sigma_x = \sigma_y = 0.15\,cm$ Gaussian beam of $20\,TeV$ protons incident along axis of solid Aluminum cylinder. Value and location of maximum energy density is indicated.

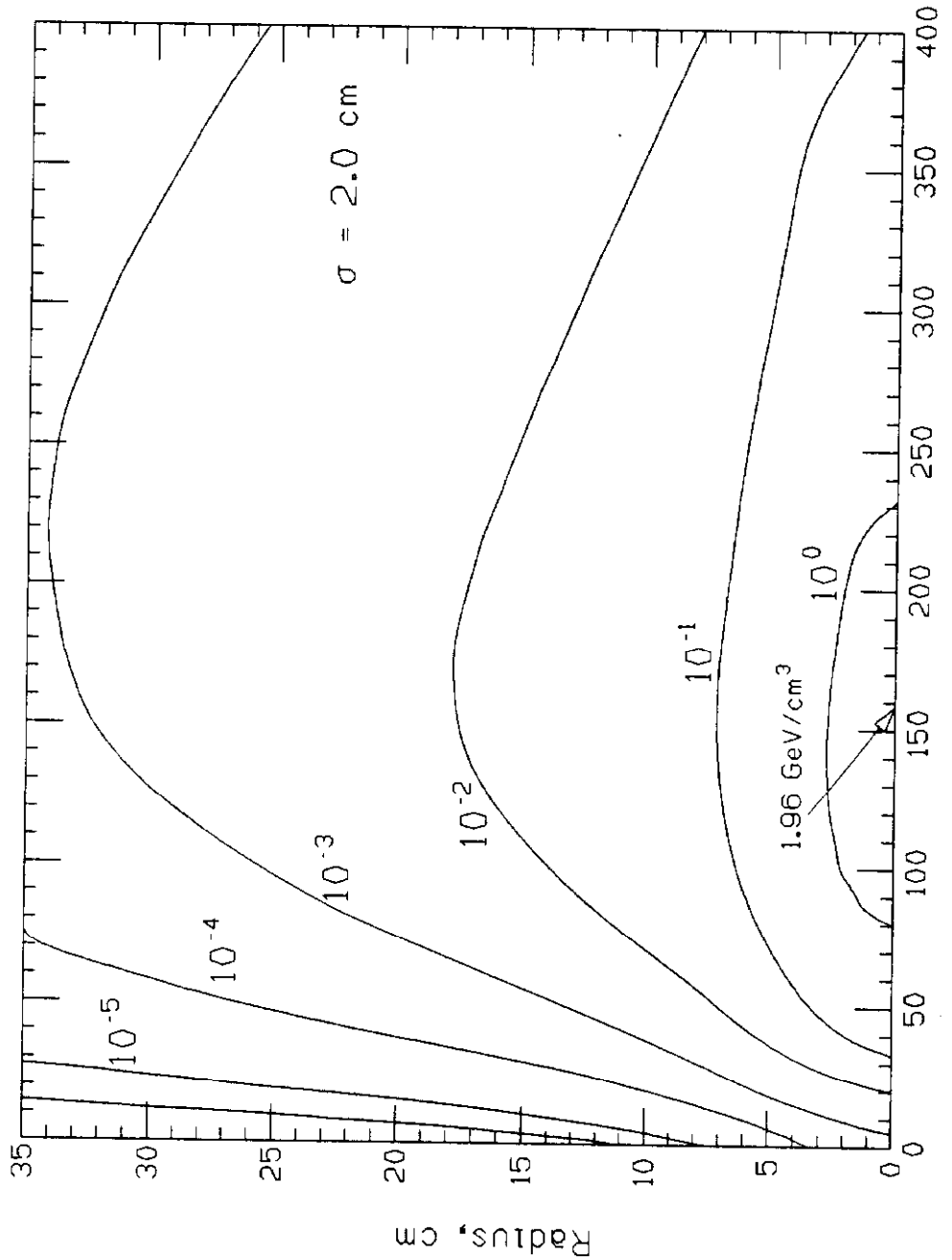

Figure 9: Contours of equal energy density for $\sigma_x = \sigma_y = 2\,cm$ Gaussian beam of $20\,TeV$ protons incident along axis of solid Aluminum cylinder. Value and location of maximum energy density is indicated.

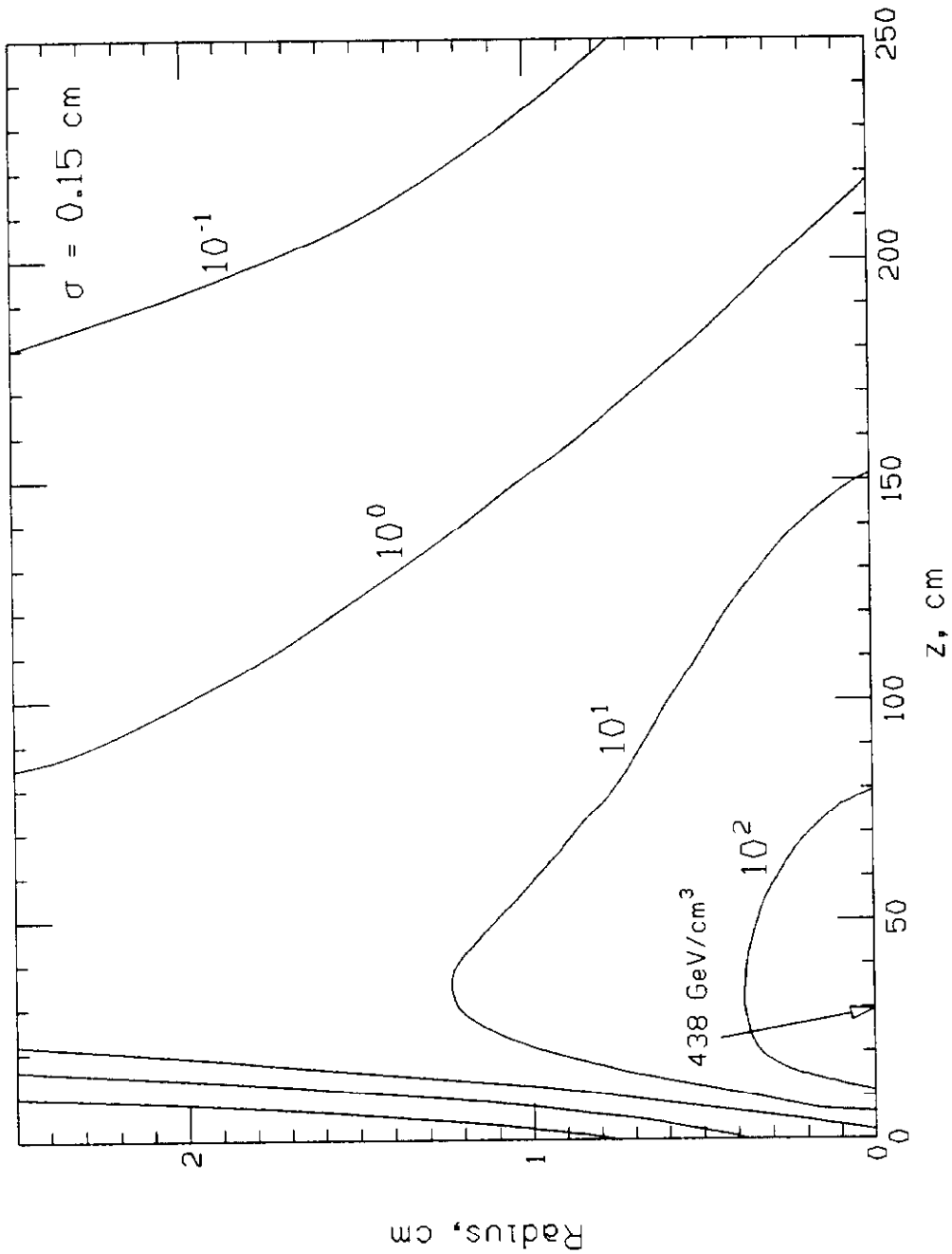

Figure 10: Contours of equal energy density for $\sigma_x = \sigma_y = 0.15\,cm$ Gaussian beam of $20\,TeV$ protons incident along axis of solid Iron cylinder. Value and location of maximum energy density is indicated.

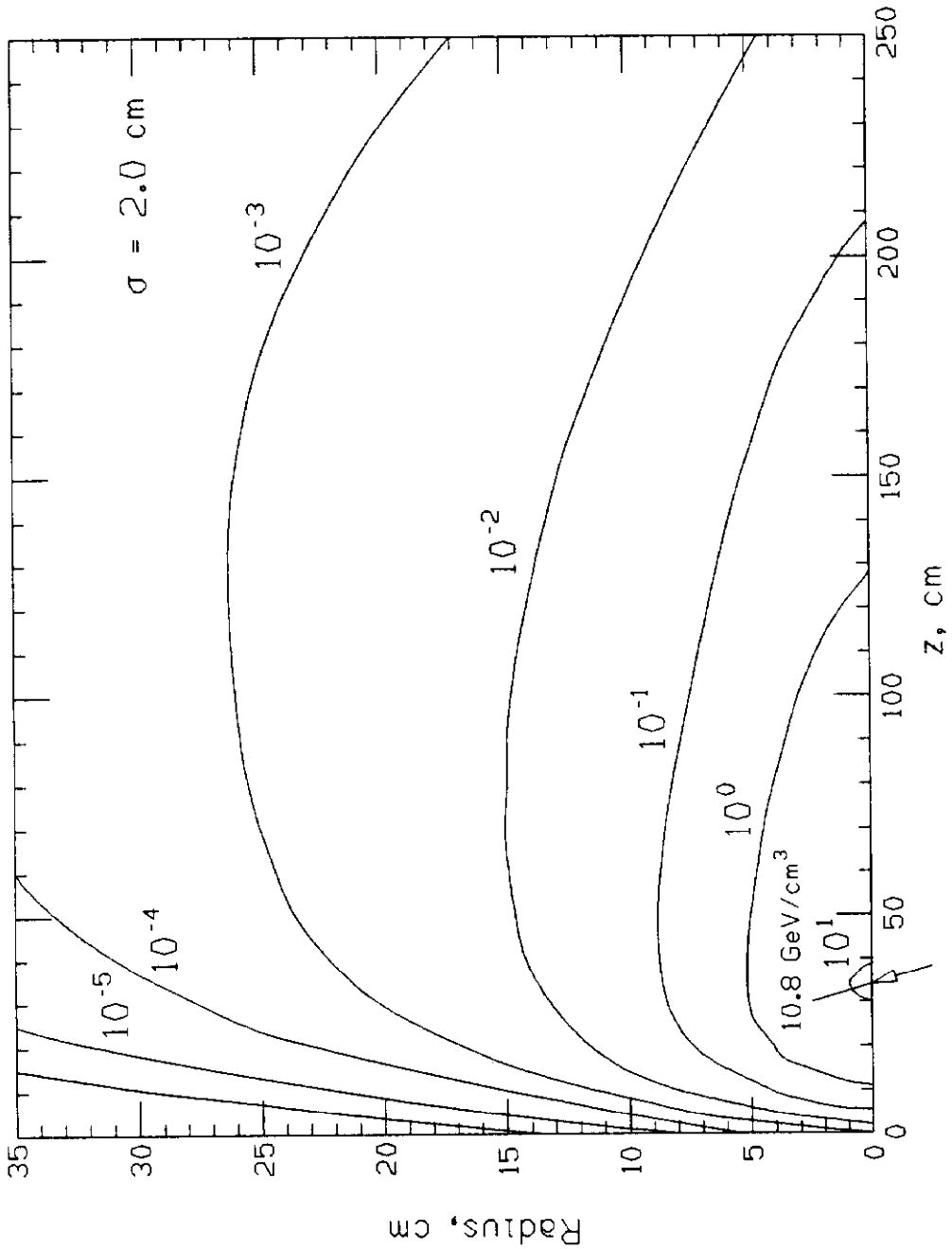

Figure 11: Contours of equal energy density for $\sigma_x = \sigma_y = 2\ cm$ Gaussian beam of $20\ TeV$ protons incident along axis of solid Iron cylinder. Value and location of maximum energy density is indicated.

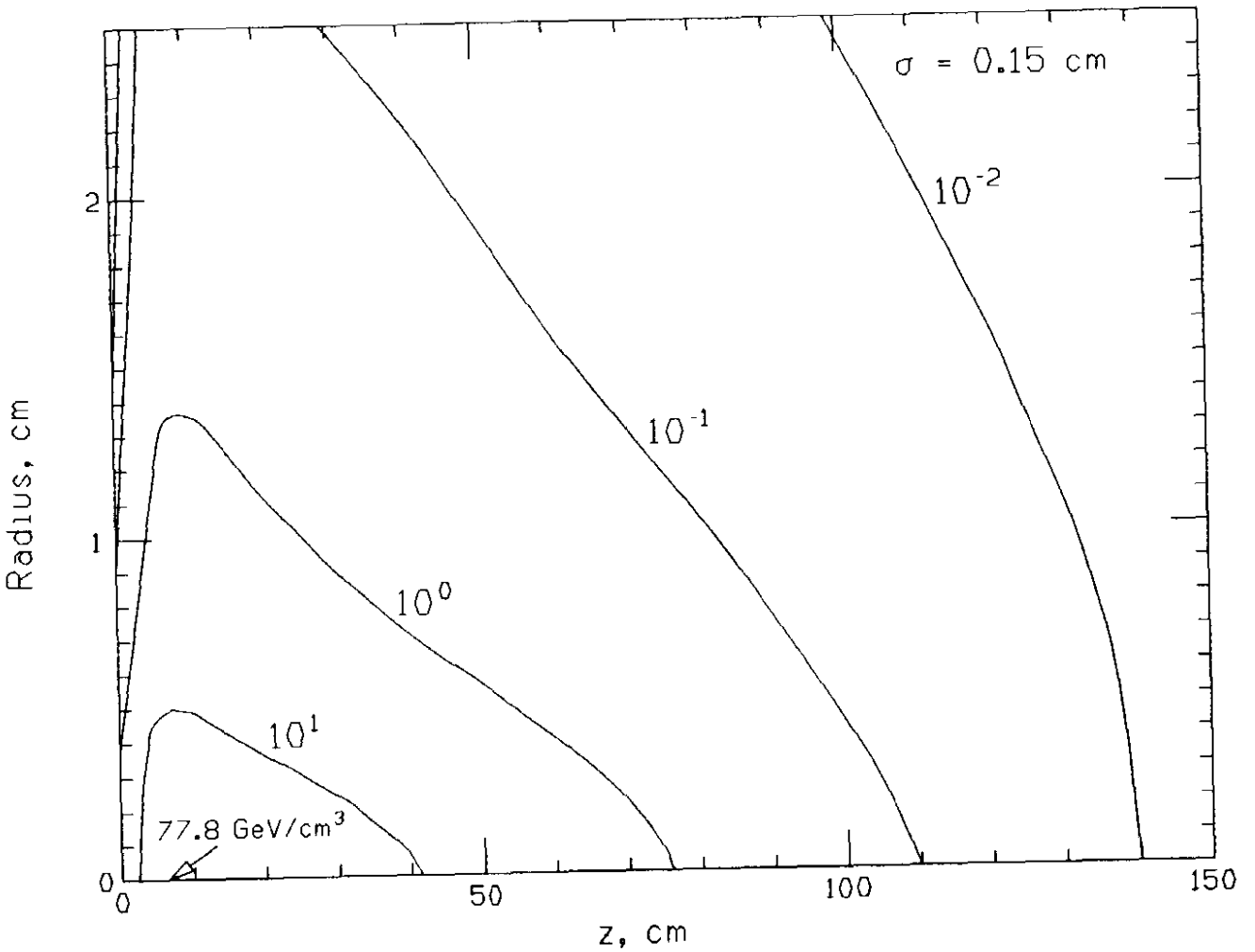

Figure 12: Contours of equal energy density for $\sigma_x = \sigma_y = 0.15\ cm$ Gaussian beam of $1\ TeV$ protons incident along axis of solid Tungsten cylinder. Value and location of maximum energy density is indicated.

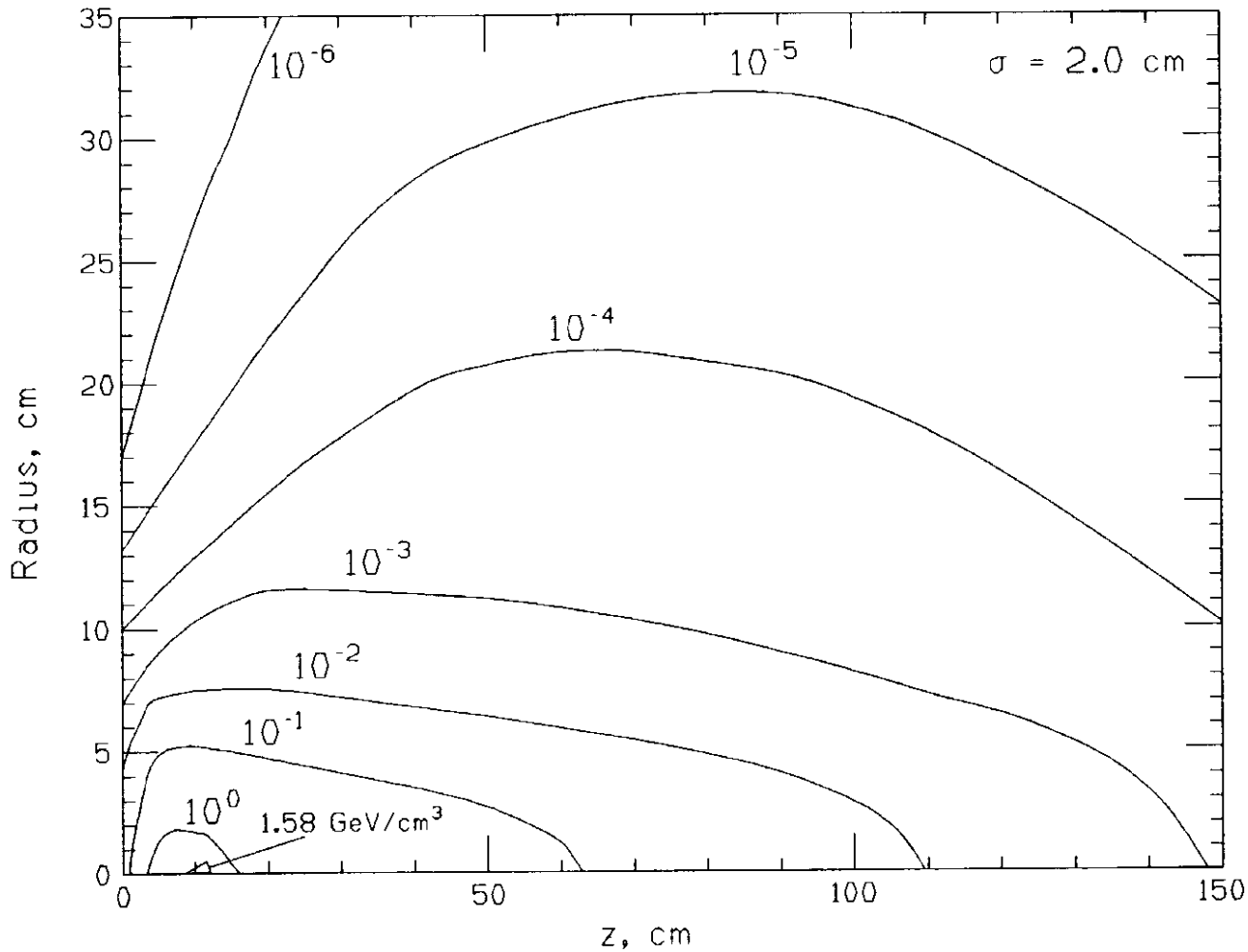

Figure 13: Contours of equal energy density for $\sigma_x = \sigma_y = 2\,cm$ Gaussian beam of 1 TeV protons incident along axis of solid Tungsten cylinder. Value and location of maximum energy density is indicated.

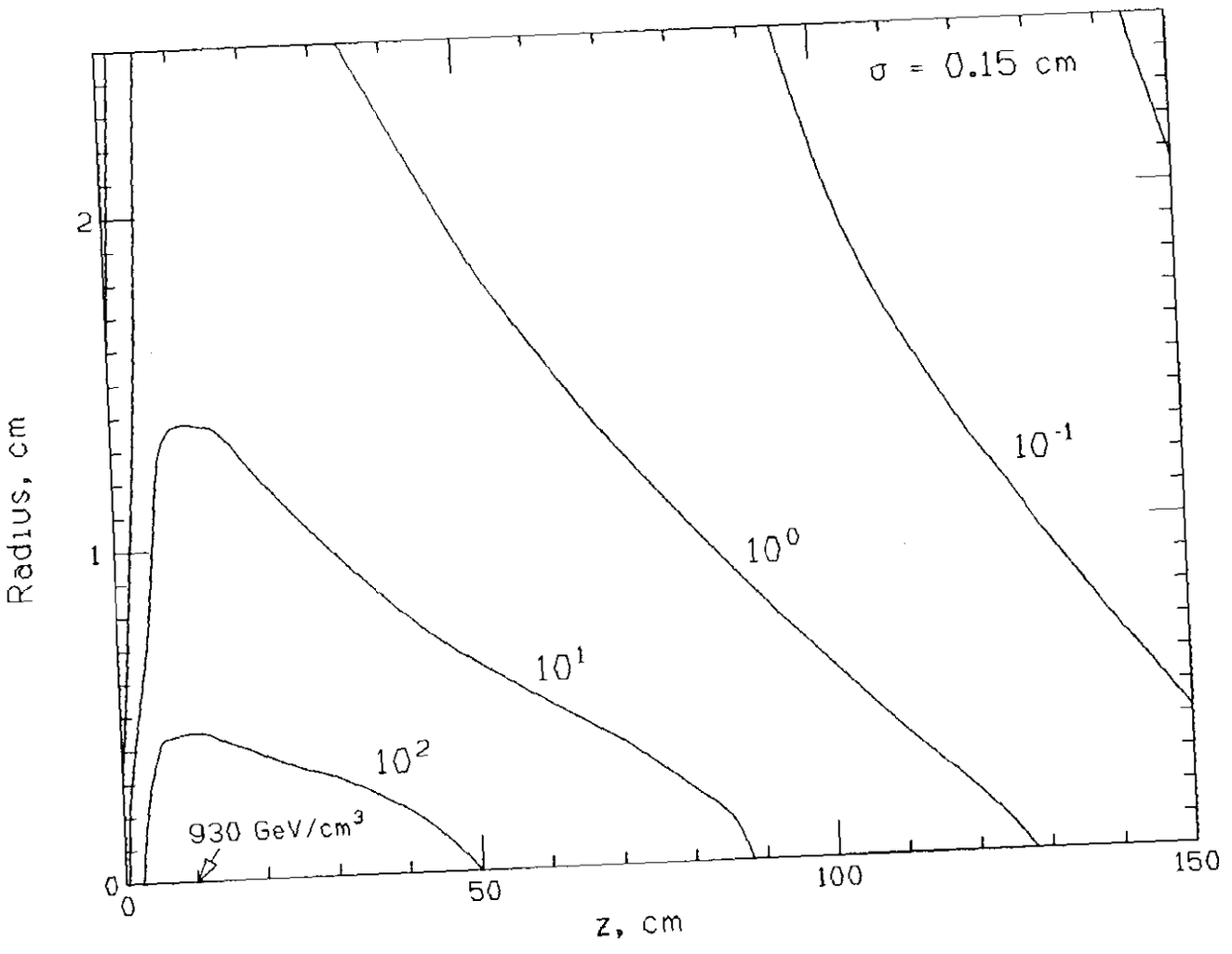

Figure 14: Contours of equal energy density for $\sigma_x = \sigma_y = 0.15\,cm$ Gaussian beam of $10\,TeV$ protons incident along axis of solid Tungsten cylinder. Value and location of maximum energy density is indicated.

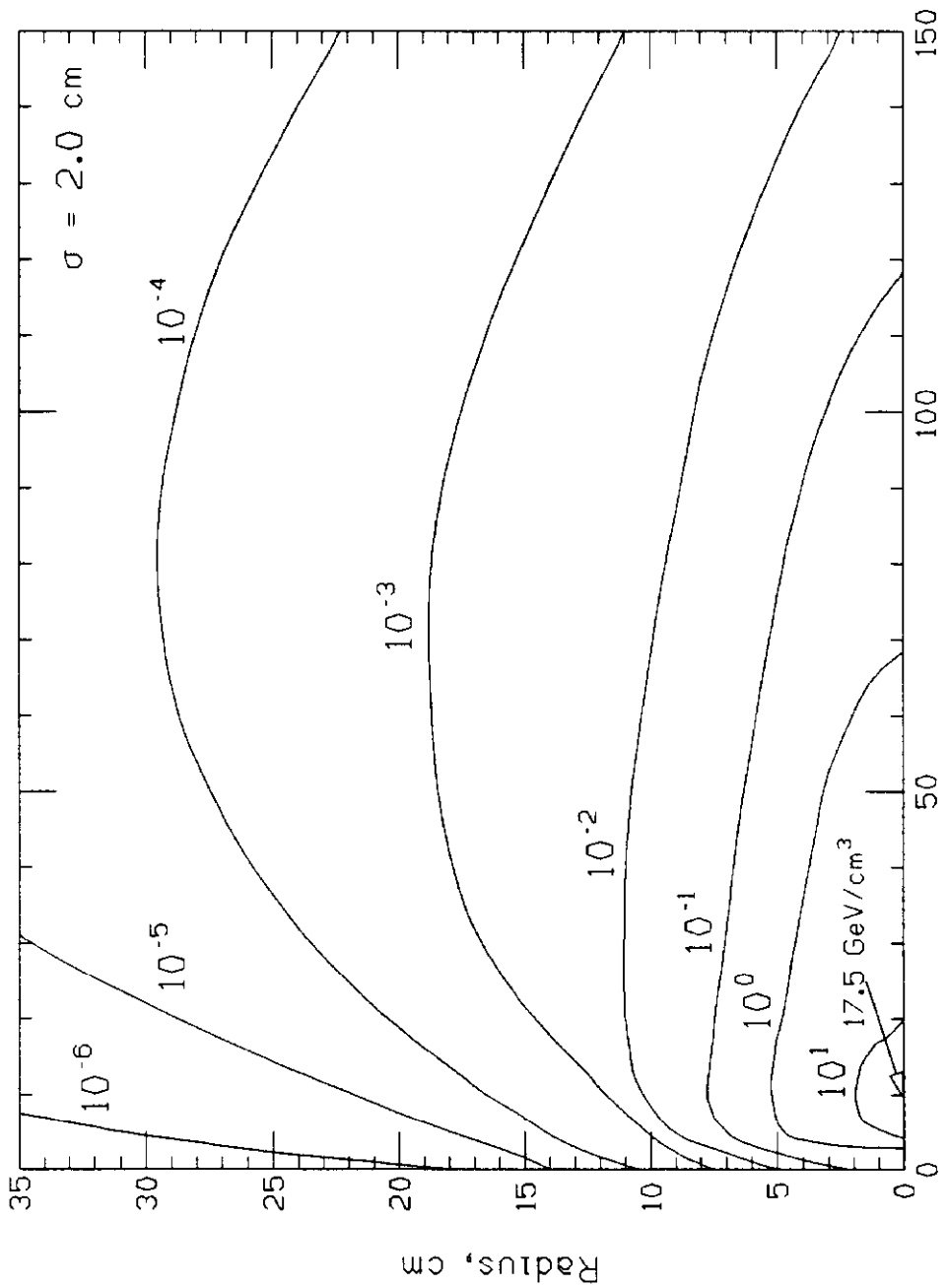

Figure 15: Contours of equal energy density for $\sigma_x = \sigma_y = 2\,cm$ Gaussian beam of $10\,TeV$ protons incident along axis of solid Tungsten cylinder. Value and location of maximum energy density is indicated.

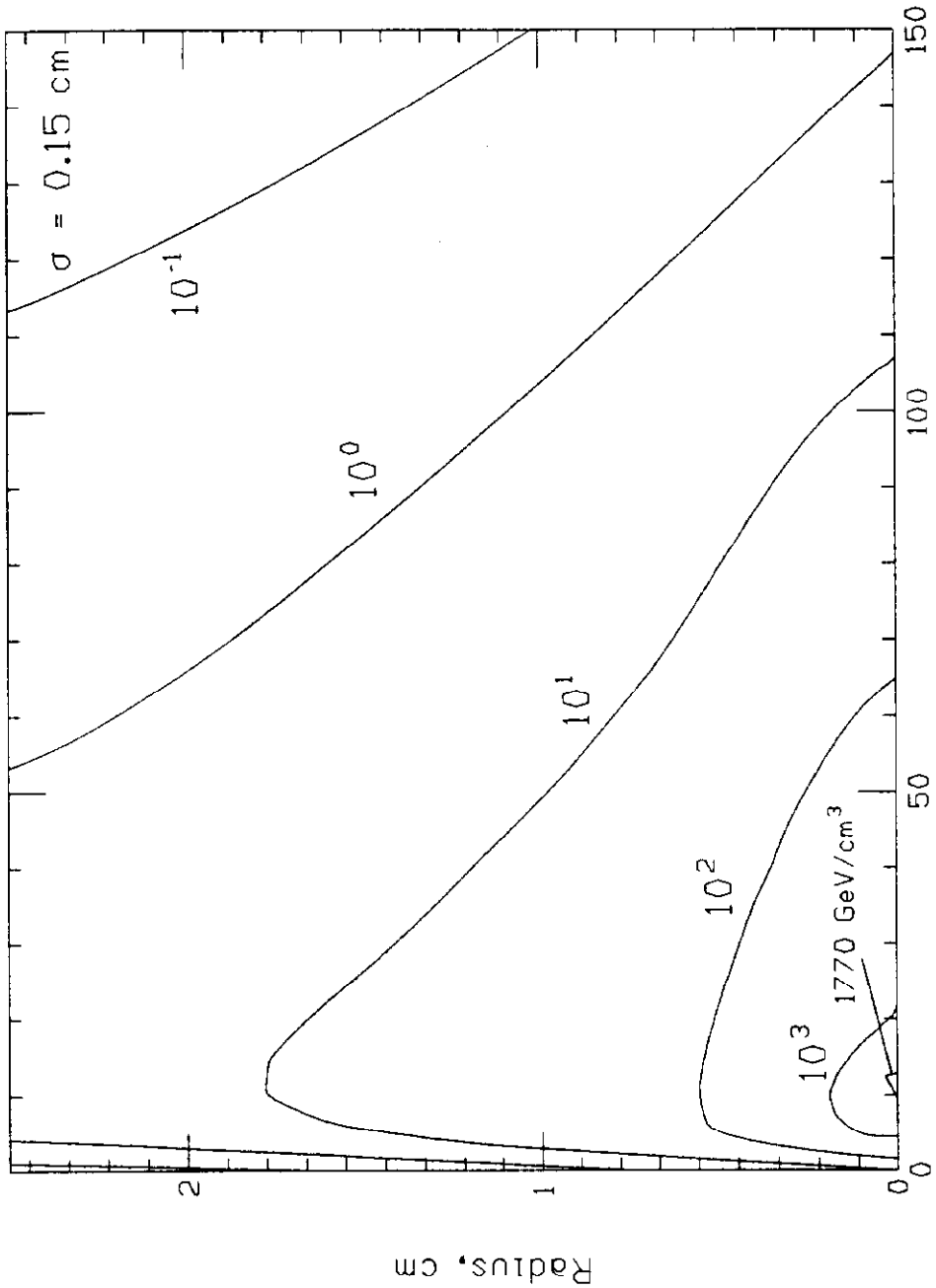

Figure 16: Contours of equal energy density for $\sigma_x = \sigma_y = 0.15\,cm$ Gaussian beam of $20\,TeV$ protons incident along axis of solid Tungsten cylinder. Value and location of maximum energy density is indicated.

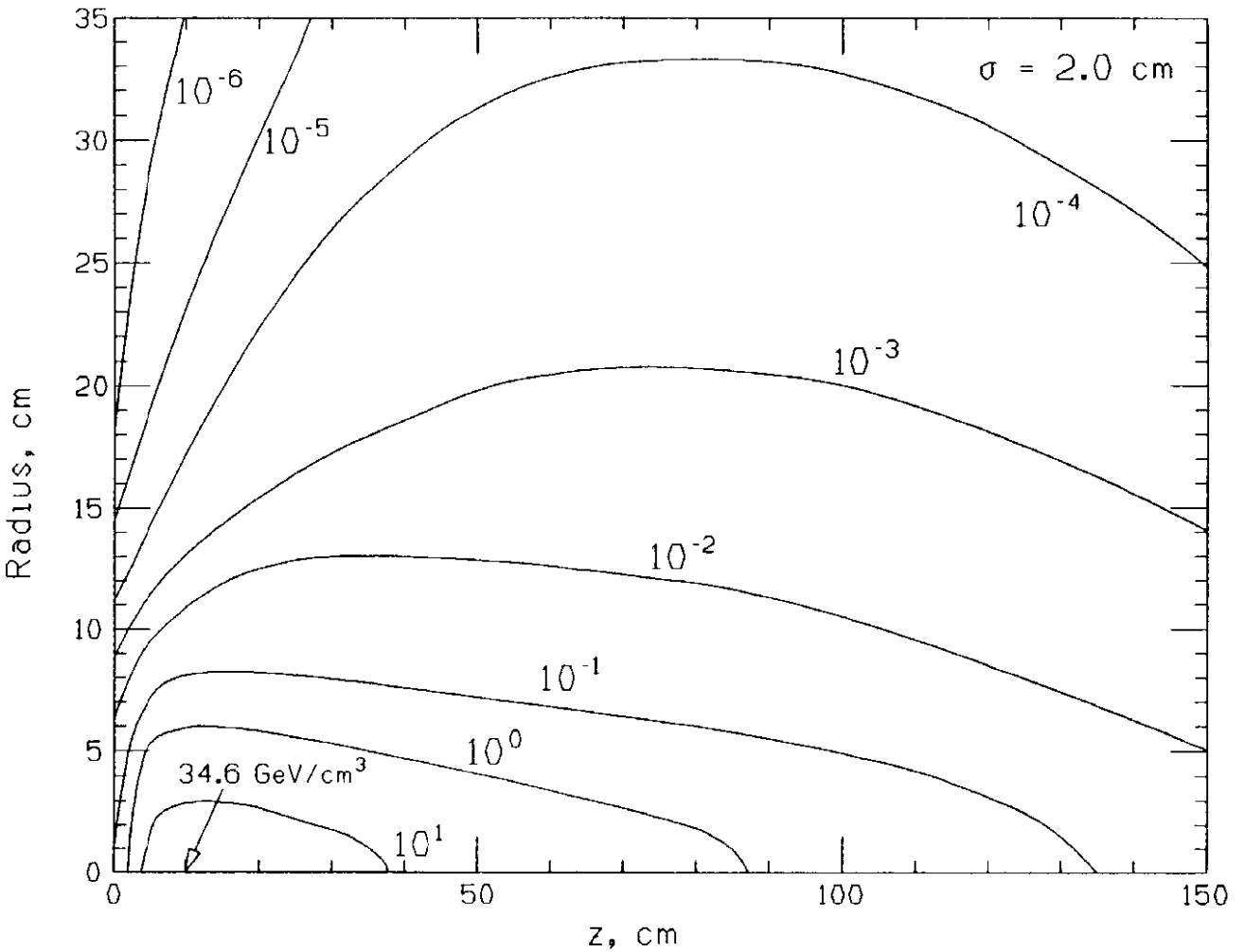

Figure 17: Contours of equal energy density for $\sigma_x = \sigma_y = 2\,cm$ Gaussian beam of $20\,TeV$ protons incident along axis of solid Tungsten cylinder. Value and location of maximum energy density is indicated.

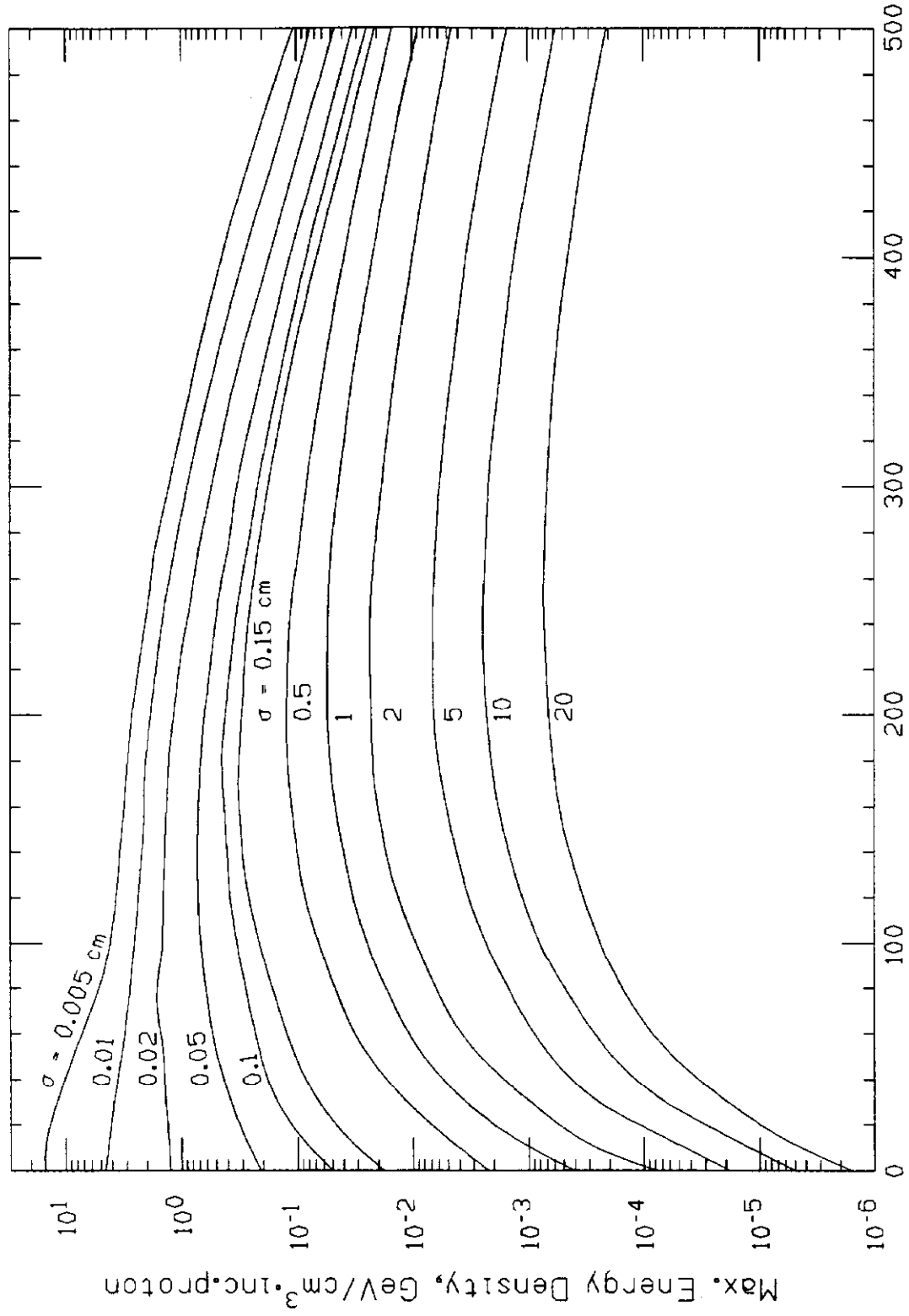

Figure 18: Maximum energy density for Gaussian beams with various σ of $1\,TeV$ protons on solid Carbon versus depth.

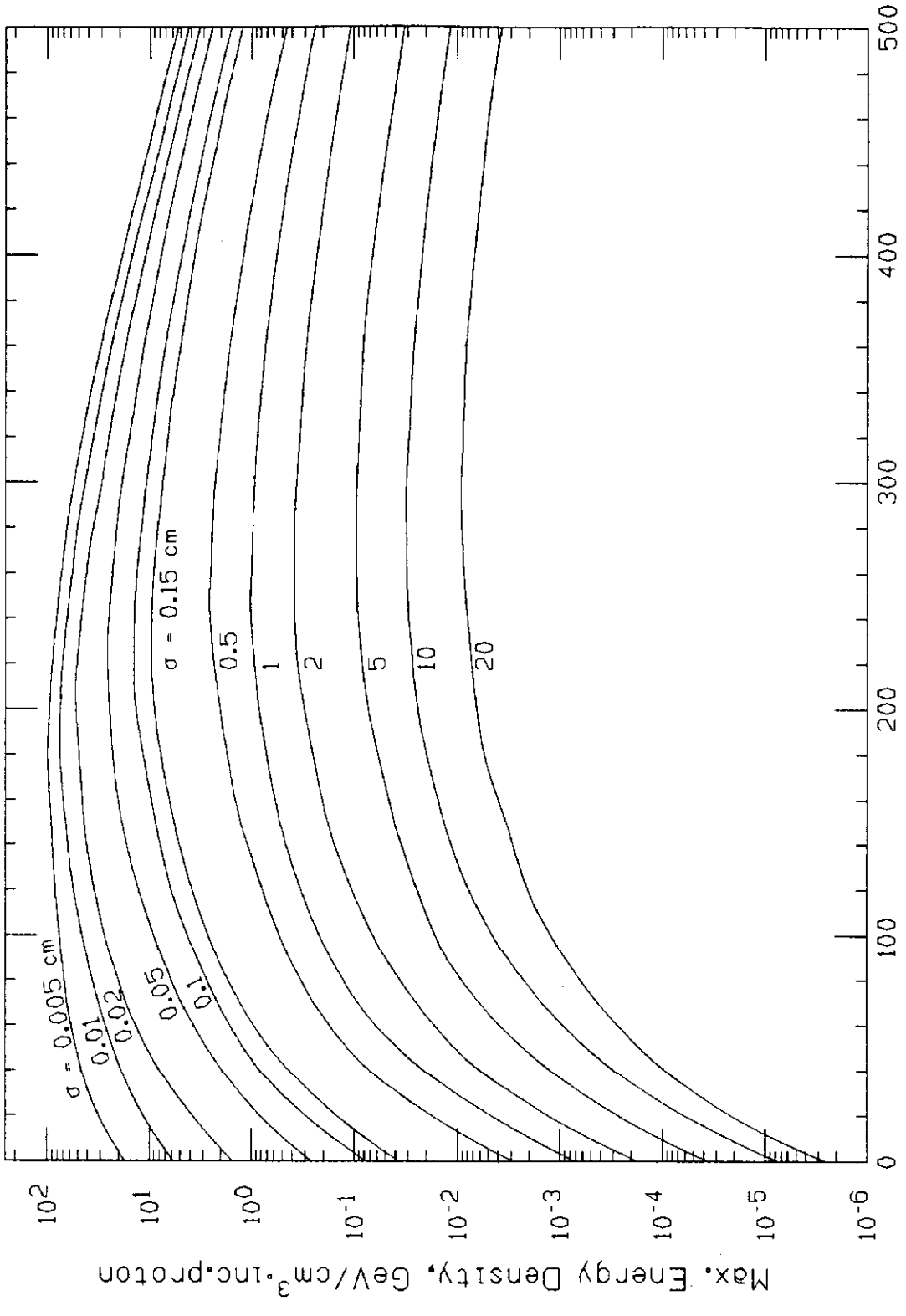

Figure 19: Maximum energy density for Gaussian beams with various σ of $10\,TeV$ protons on solid Carbon versus depth.

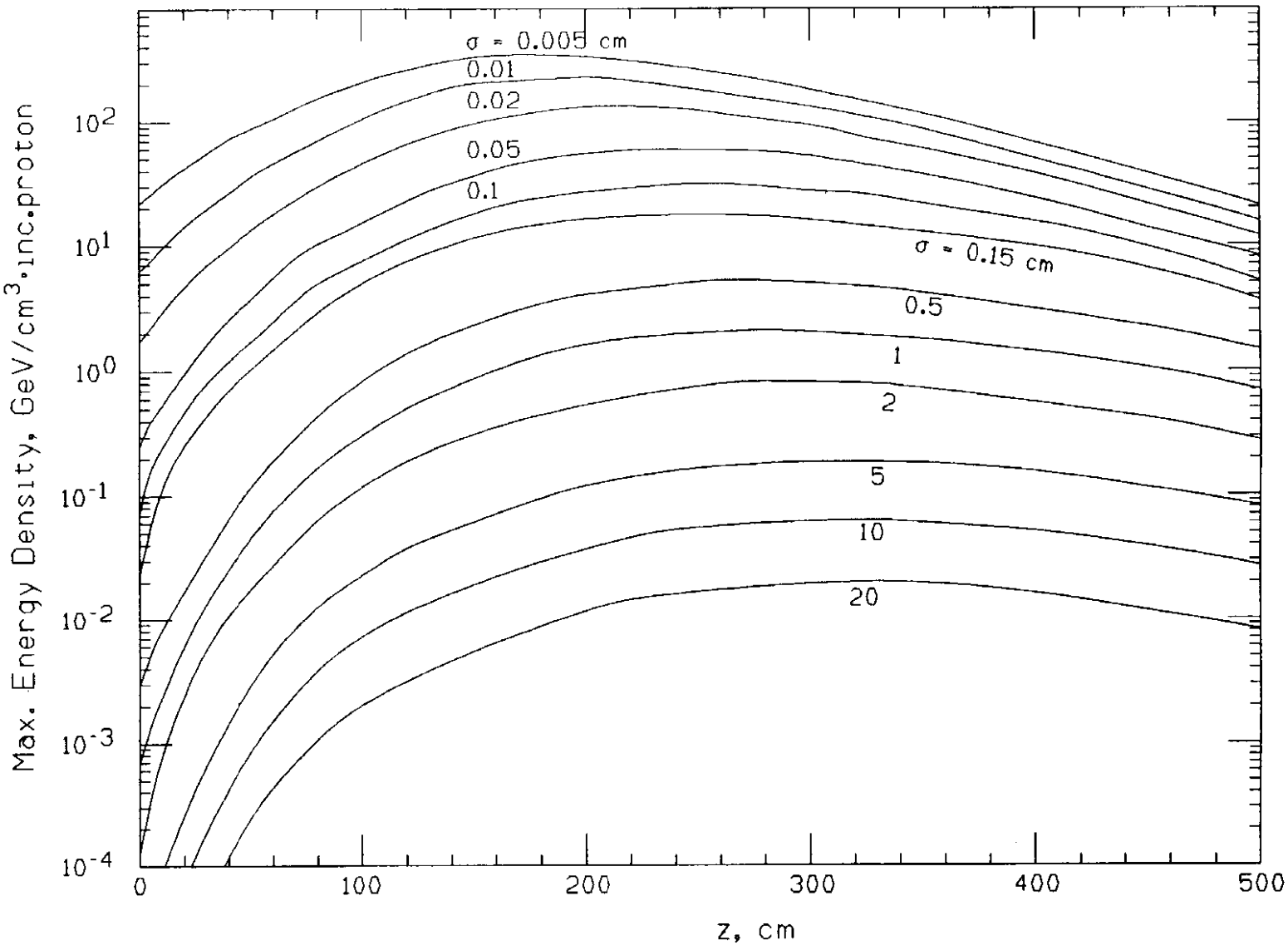

Figure 20: Maximum energy density for Gaussian beams with various σ of $20\,TeV$ protons on solid Carbon versus depth.

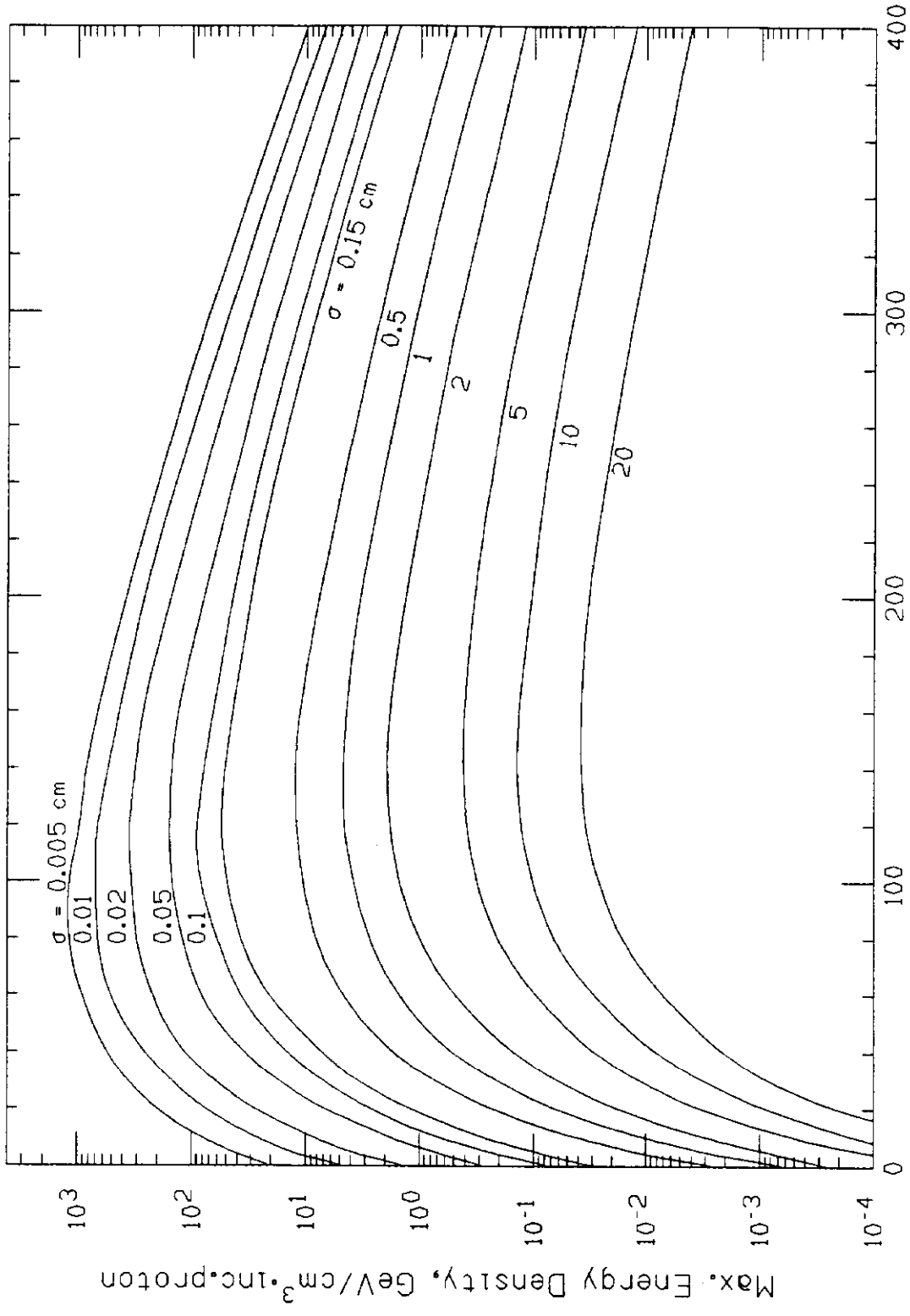

Figure 21: Maximum energy density for Gaussian beams with various σ of 20 TeV protons on solid Aluminum versus depth.

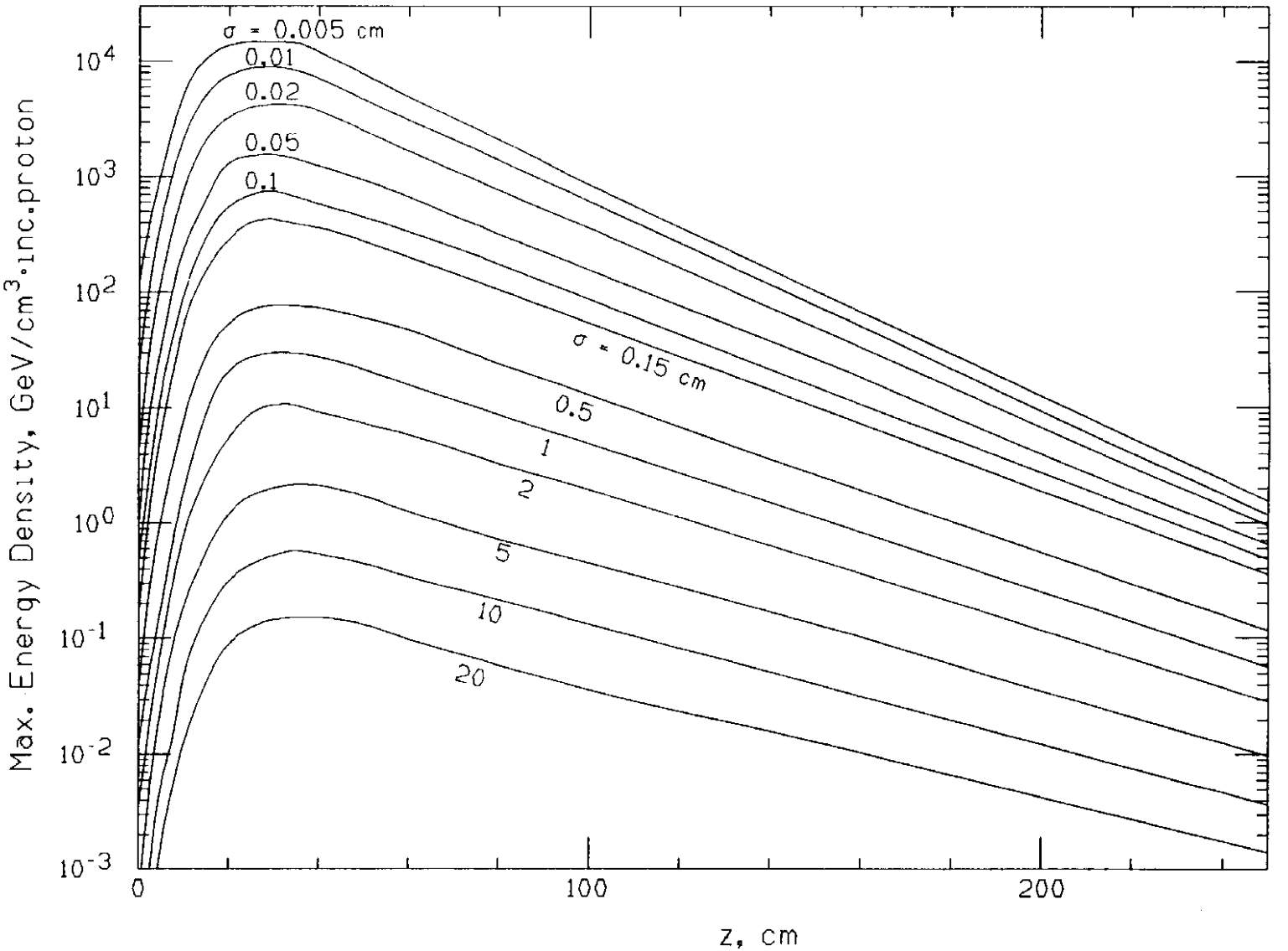

Figure 22: Maximum energy density for Gaussian beams with various σ of 20 TeV protons on solid Iron versus depth.

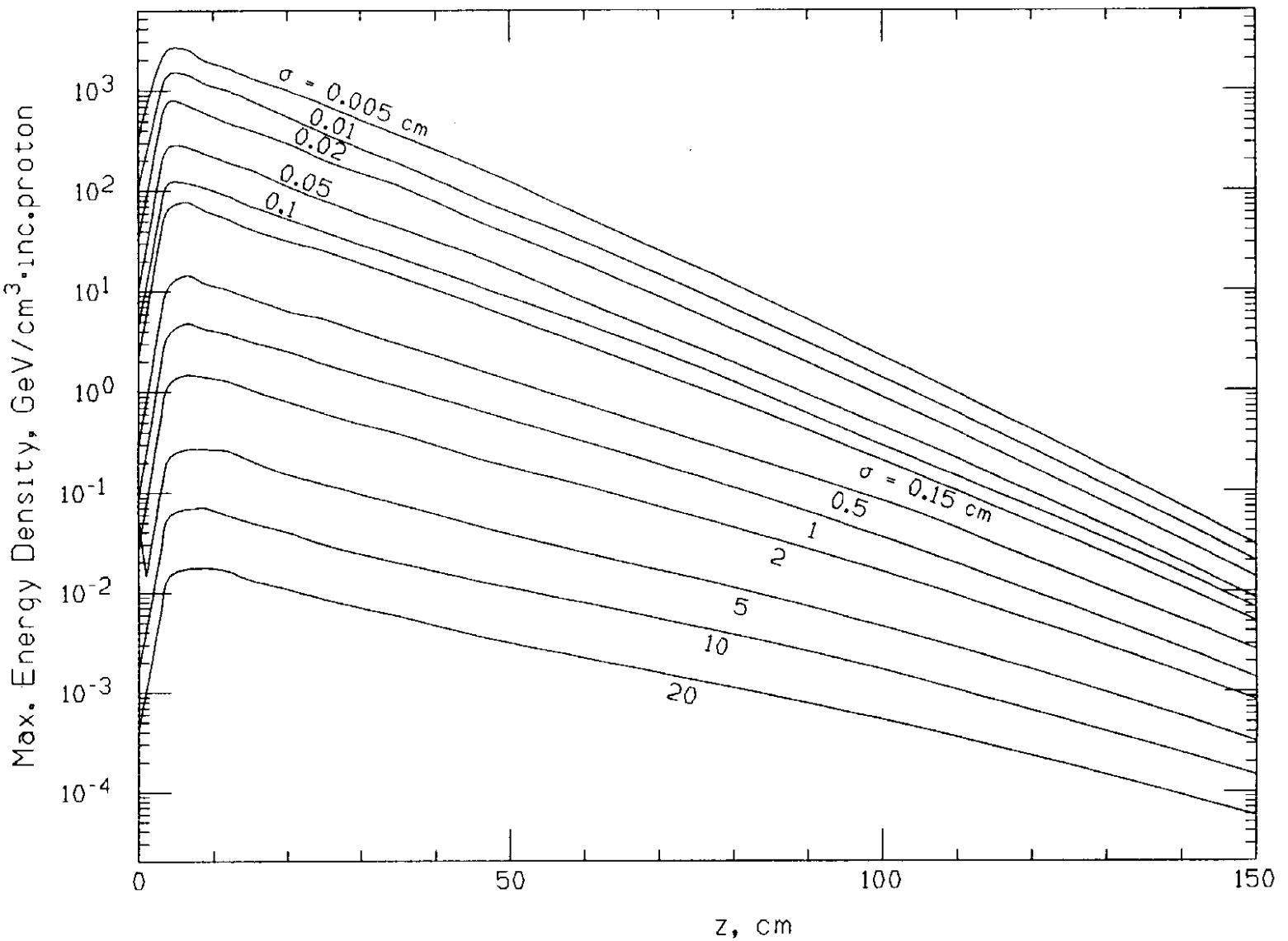

Figure 23: Maximum energy density for Gaussian beams with various σ of $1\,TeV$ protons on solid Tungsten versus depth.

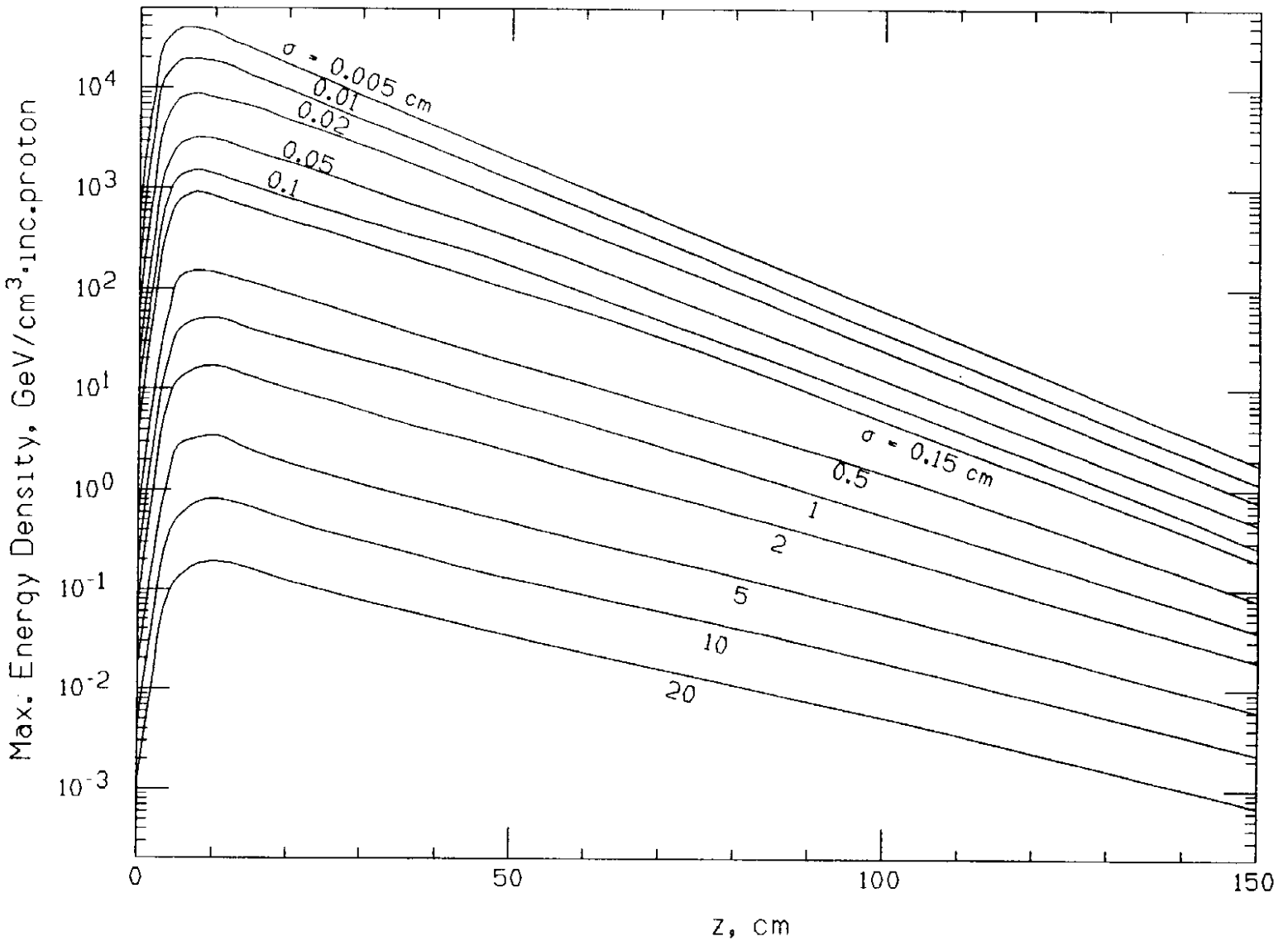

Figure 24: Maximum energy density for Gaussian beams with various σ of 10 TeV protons on solid Tungsten versus depth.

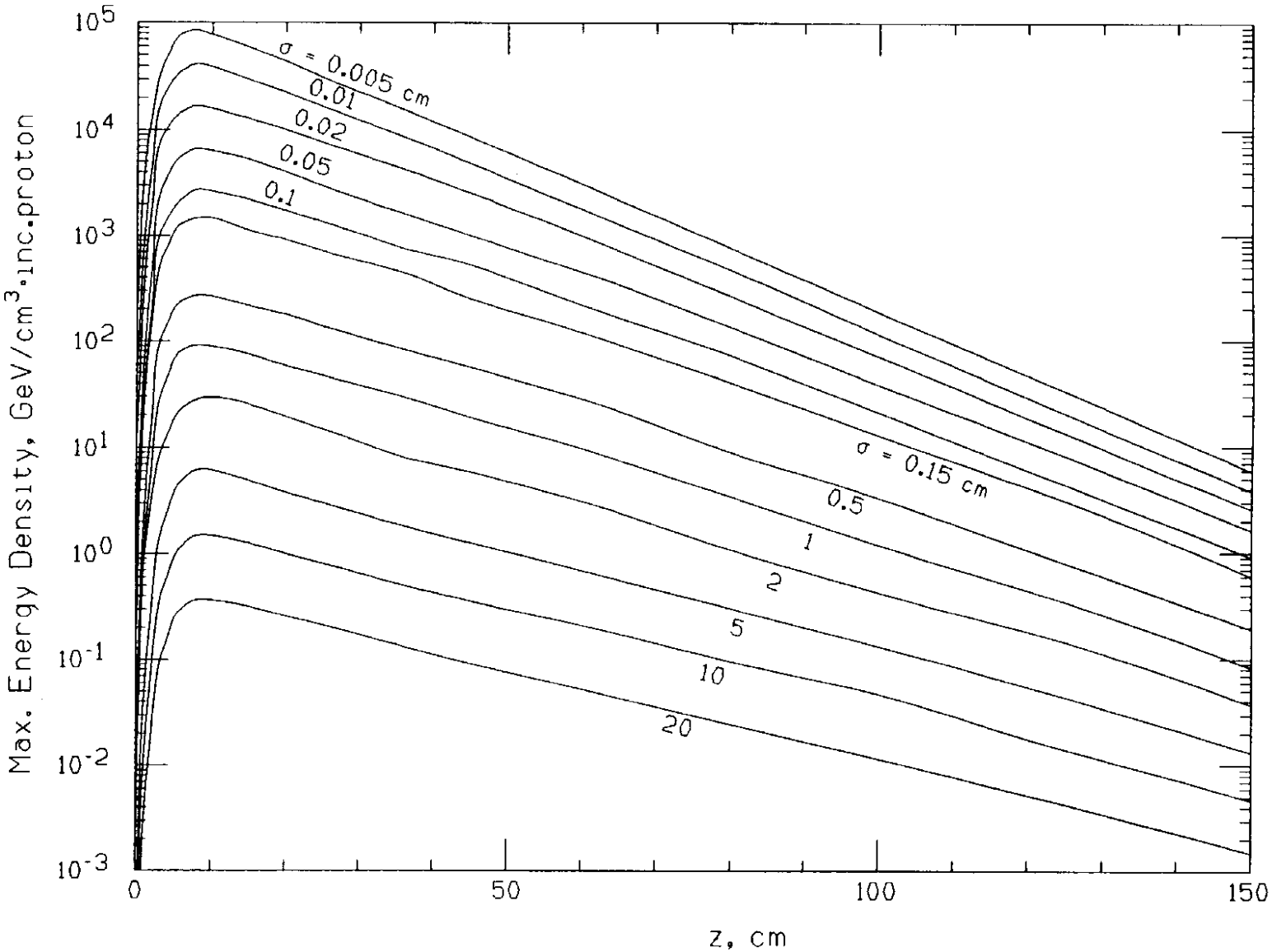

Figure 25: Maximum energy density for Gaussian beams with various σ of 20 TeV protons on solid Tungsten versus depth.

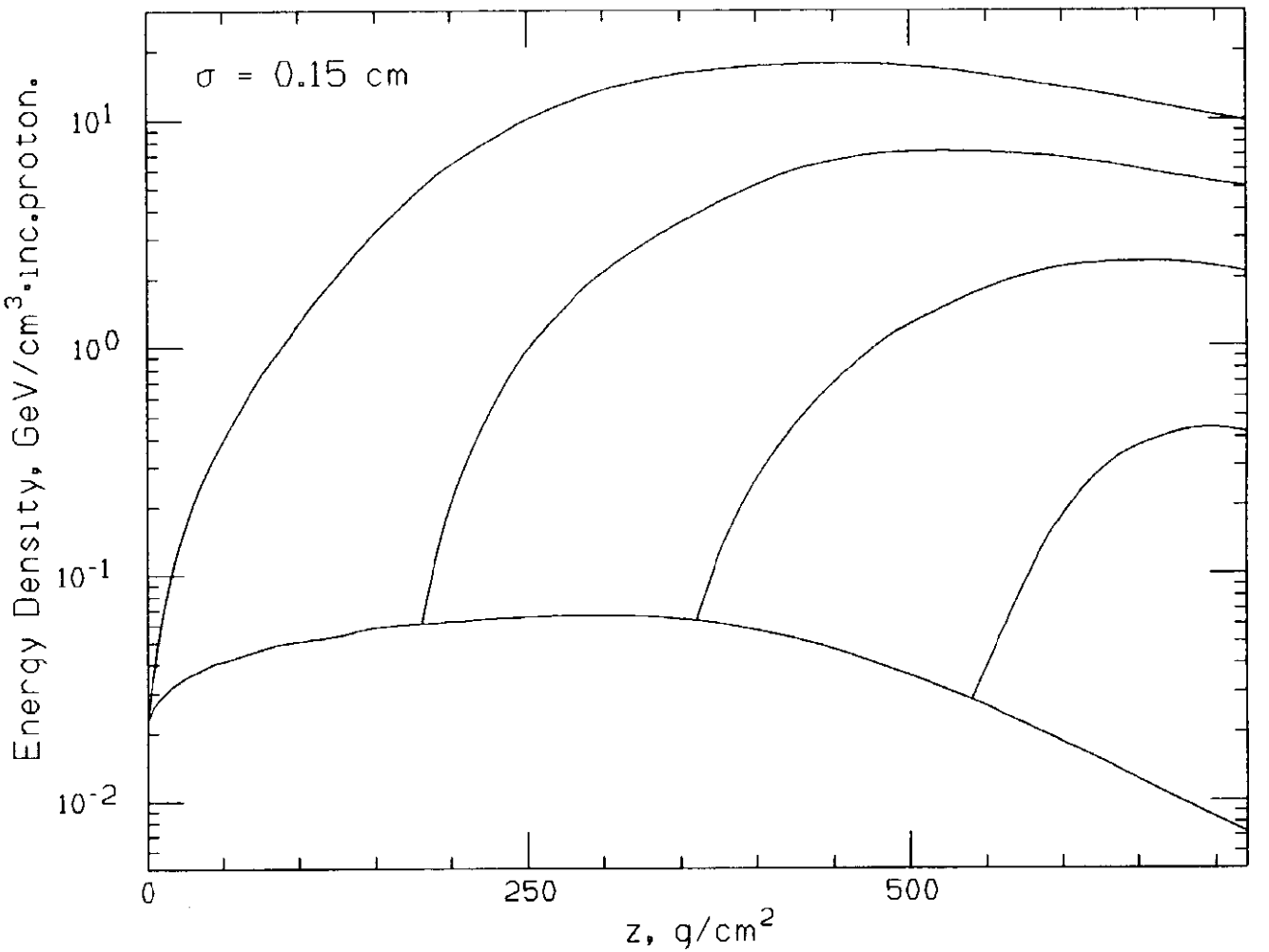

Figure 27: Maximum energy density for $\sigma = 0.15\,cm$ Gaussian beam of $20\,TeV$ protons on Carbon ($2\,cm$ thick plates at $1\,m$ intervals) versus depth (g/cm^2). Upper curve: solid dump, lower: full array, in between: dumps at $50, 100, 150\,m$.

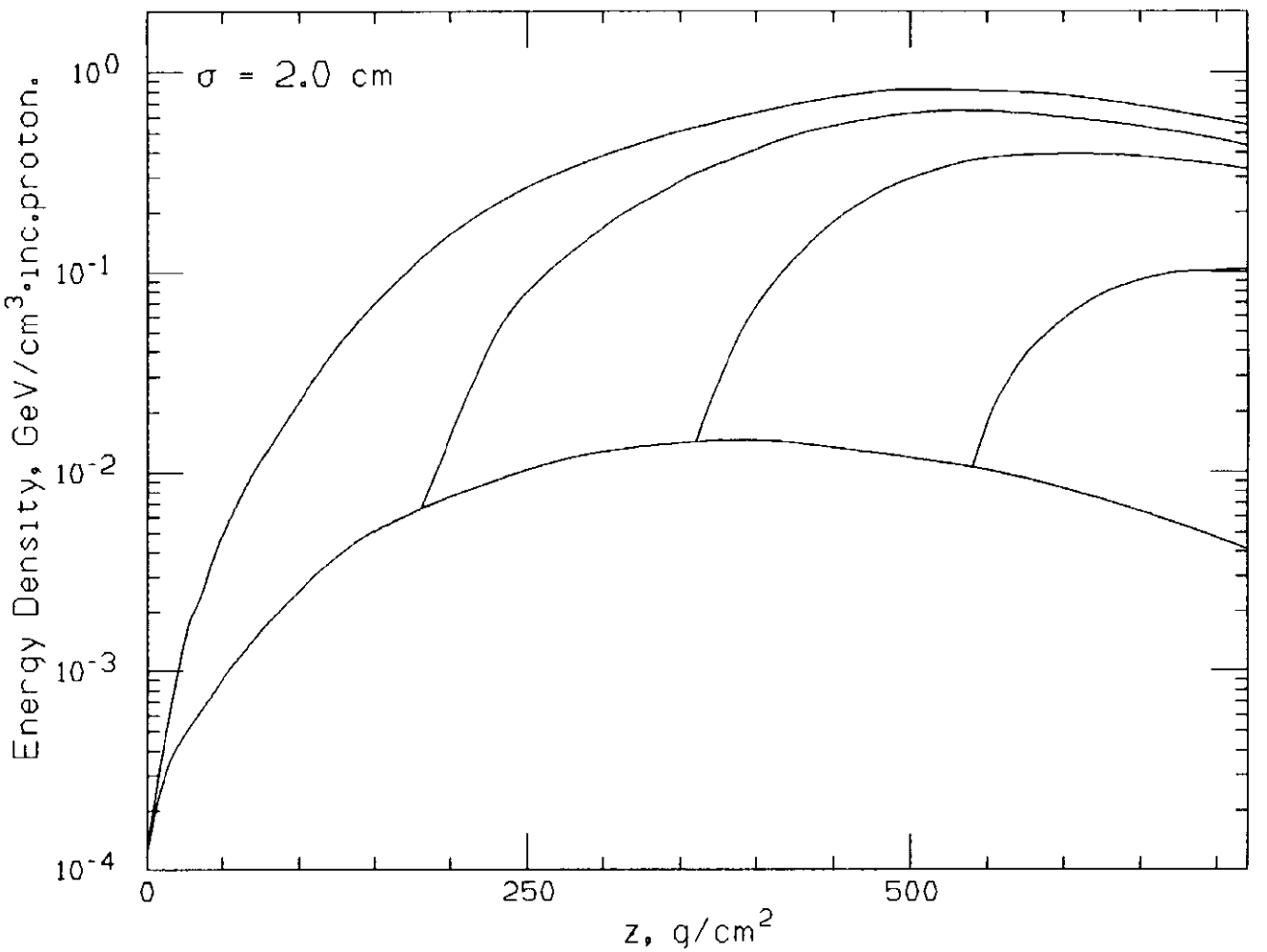

Figure 28: Maximum energy density for $\sigma = 2\,cm$ Gaussian beam of $20\,TeV$ protons on Carbon ($2\,cm$ thick plates at $1\,m$ intervals) versus depth (g/cm^2). Upper curve: solid dump, lower: full array, in between: dumps at $50, 100, 150\,m$.

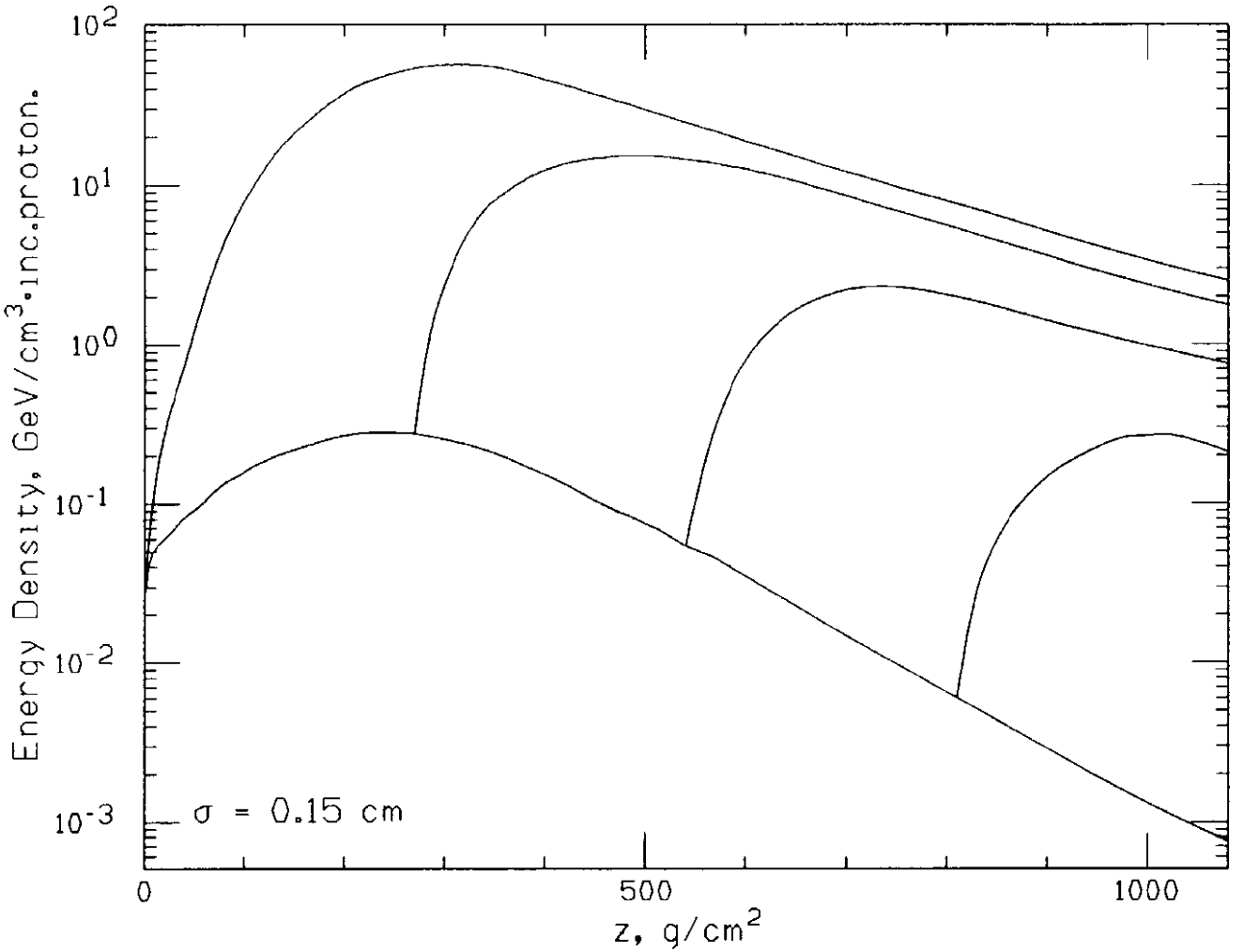

Figure 29: Maximum energy density for $\sigma = 0.15\,cm$ Gaussian beam of $20\,TeV$ protons on Aluminum ($2\,cm$ thick plates at $1\,m$ intervals) versus depth (g/cm^2). Upper curve: solid dump, lower: full array, in between: dumps at $50, 100, 150\,m$.

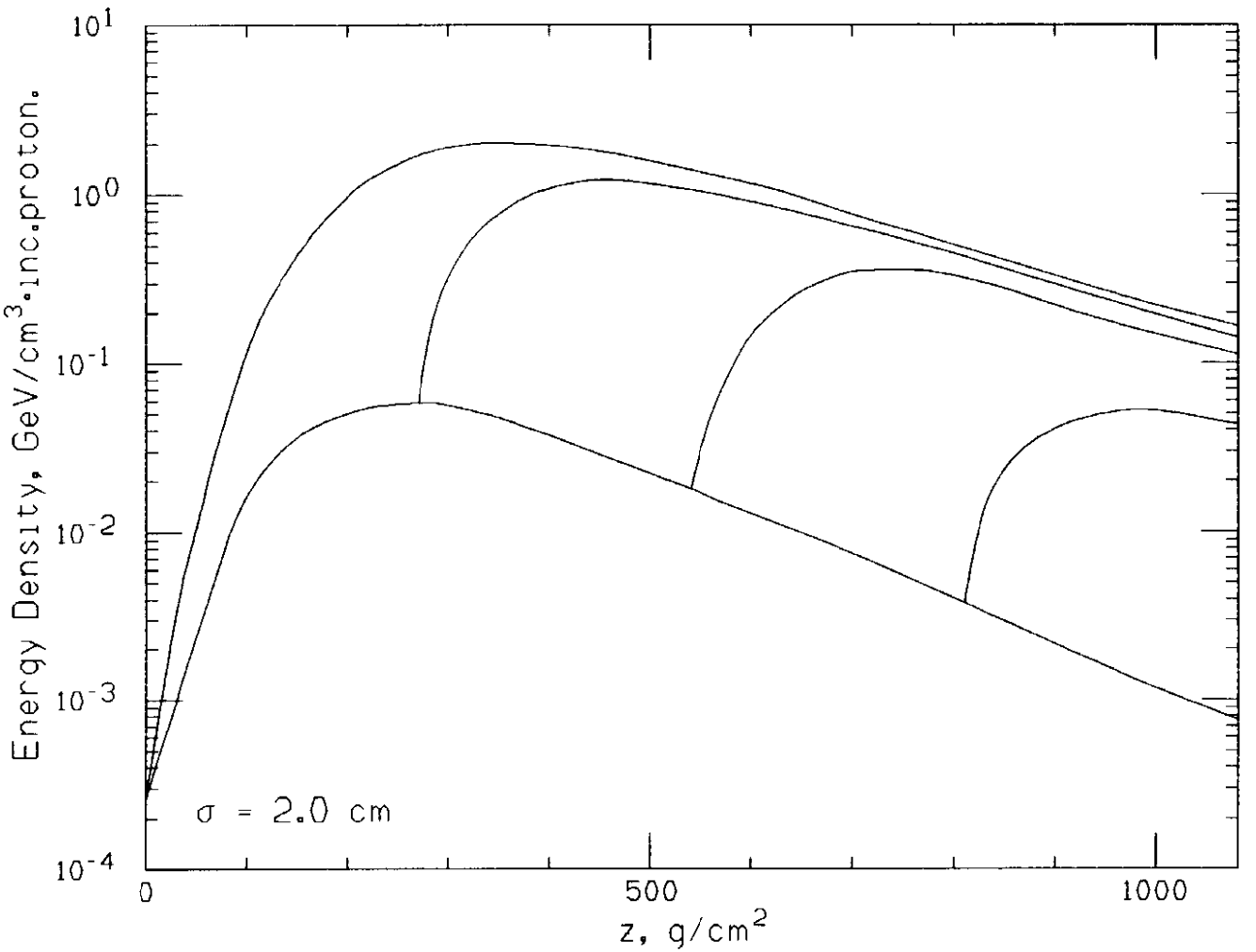

Figure 30: Maximum energy density for $\sigma = 2\,cm$ Gaussian beam of 20 TeV protons on Aluminum ($2\,cm$ thick plates at $1\,m$ intervals) versus depth (g/cm^2). Upper curve: solid dump, lower: full array, in between: dumps at $50, 100, 150\,m$.

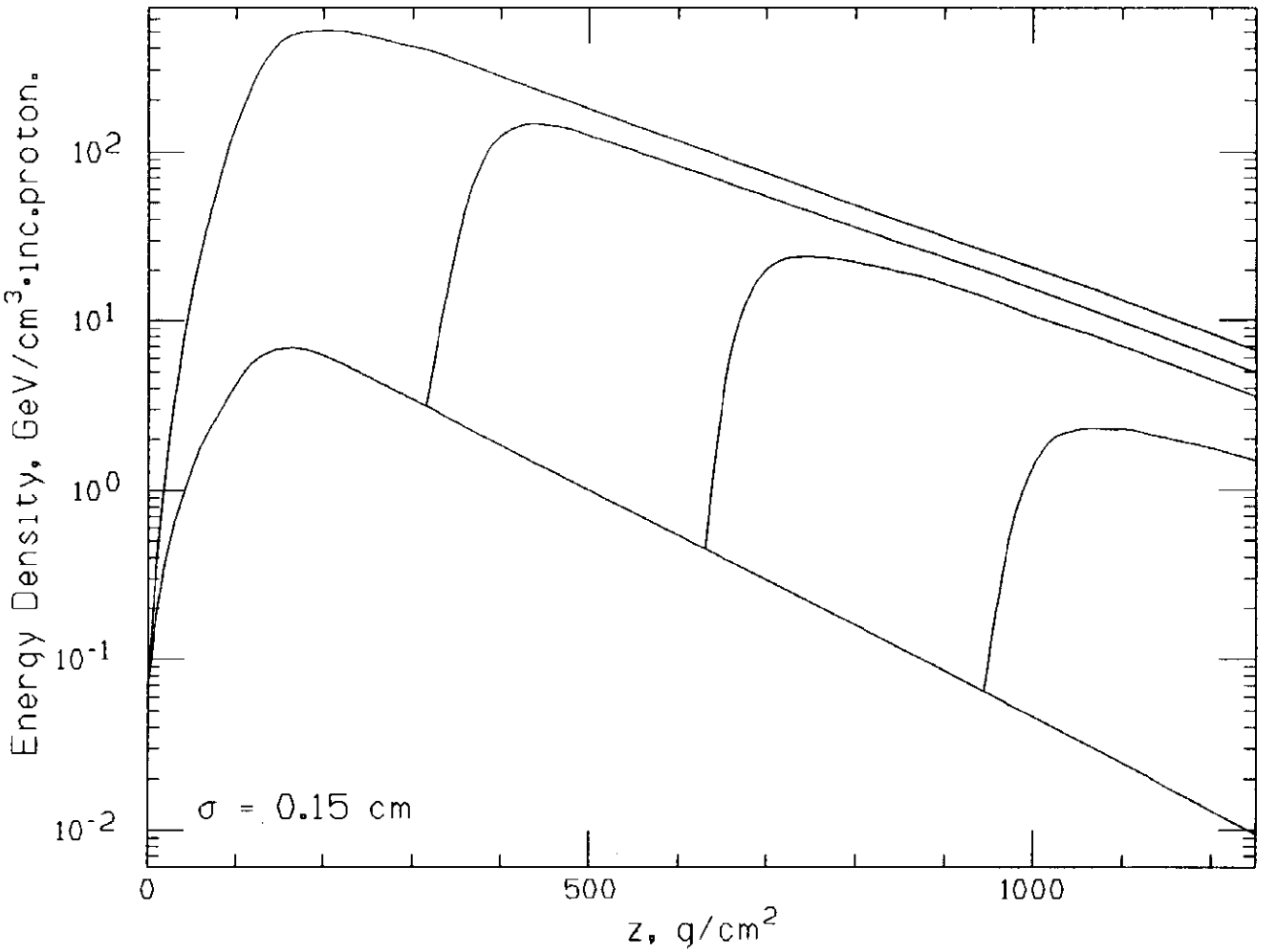

Figure 31: Maximum energy density for $\sigma = 0.15\,cm$ Gaussian beam of 20 TeV protons on Iron (1 cm thick plates at 1 m intervals) versus depth (g/cm^2). Upper curve: solid dump, lower: full array, in between: dumps at $40, 80, 120\,m$.

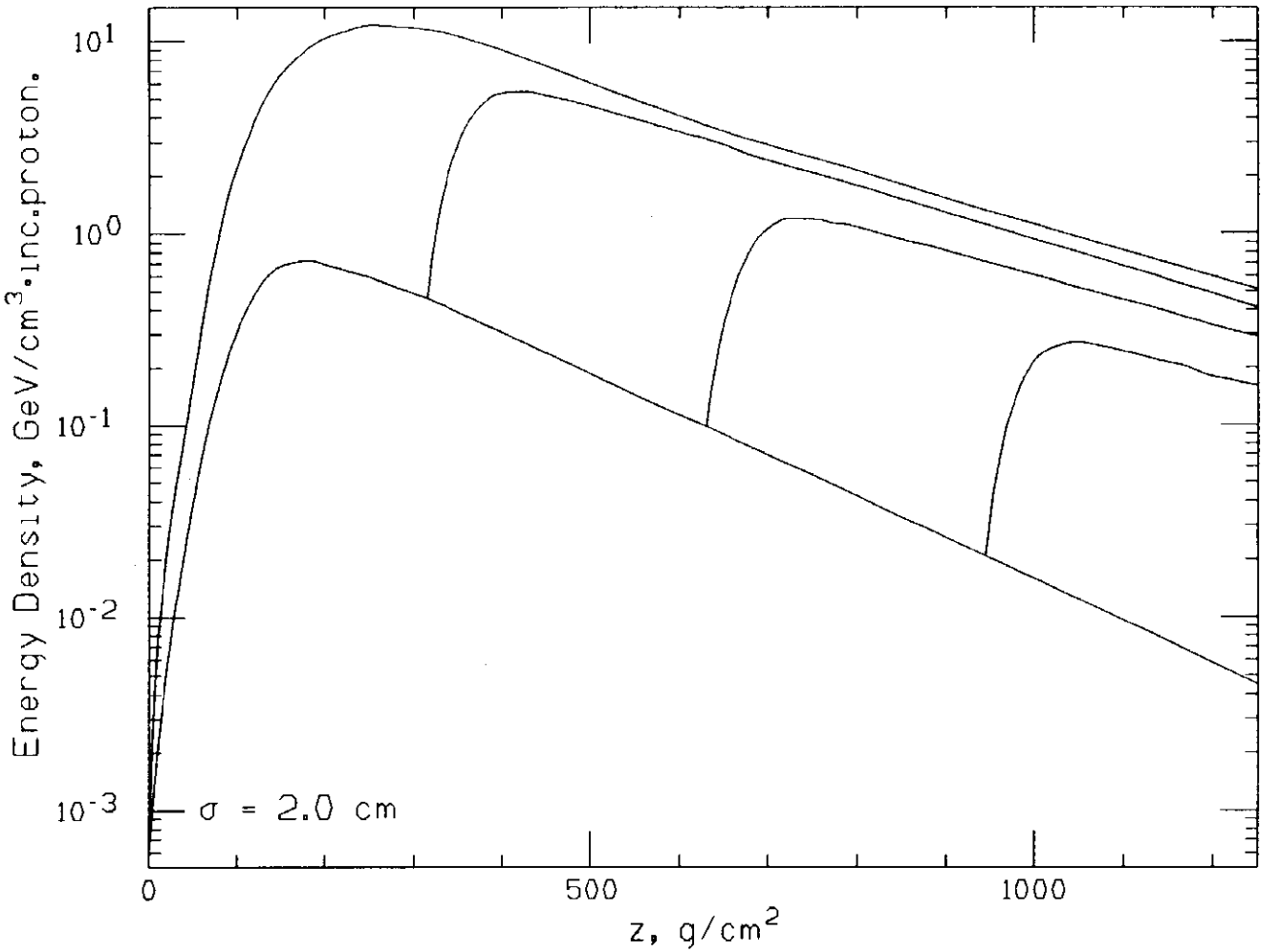

Figure 32: Maximum energy density for $\sigma = 2cm$ Gaussian beam of $20TeV$ protons on Iron ($1cm$ thick plates at $1m$ intervals) versus depth (g/cm^2). Upper curve: solid dump, lower: full array, in between: dumps at $40, 80, 120\,m$.

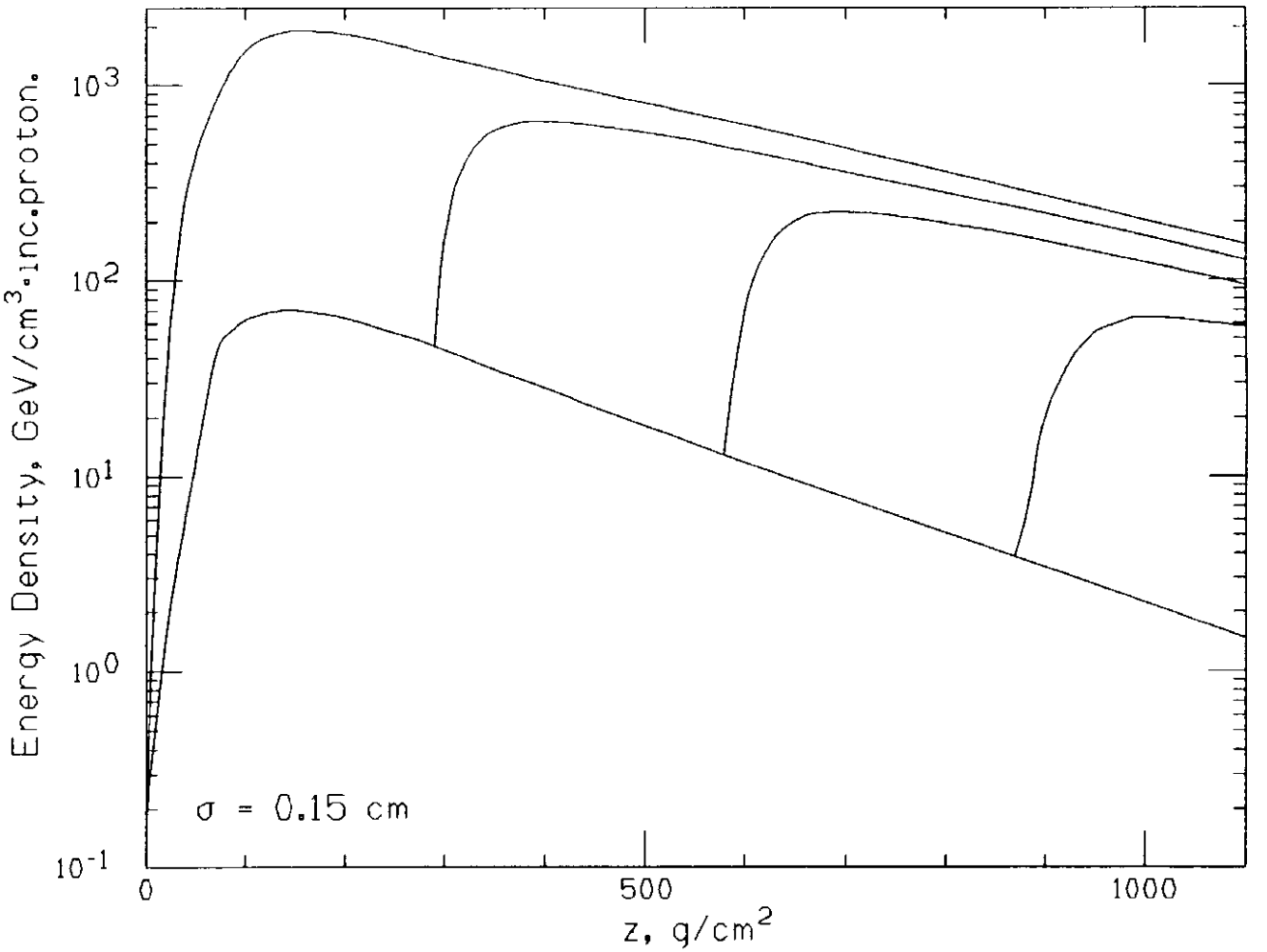

Figure 33: Maximum energy density for $\sigma = 0.15\,cm$ Gaussian beam of $20\,TeV$ protons on Tungsten ($1\,cm$ thick plates at $1\,m$ intervals) versus depth (g/cm^2). Upper curve: solid dump, lower: full array, in between: dumps at $15, 30, 45\,m$.

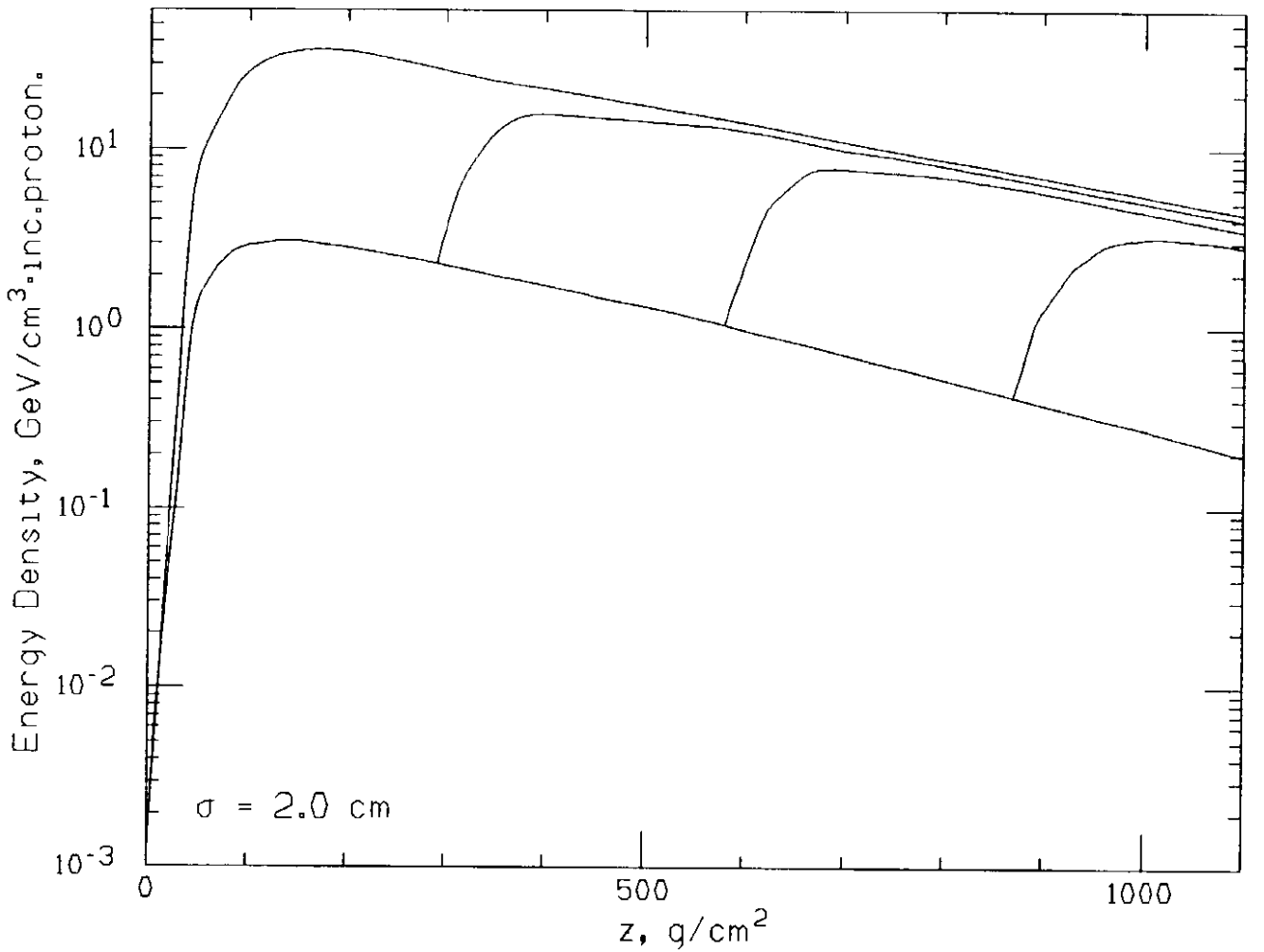

Figure 34: Maximum energy density for $\sigma = 2\,cm$ Gaussian beam of 20 TeV protons on Tungsten (1 cm thick plates at 1 m intervals) versus depth (g/cm^2). Upper curve: solid dump, lower: full array, in between: dumps at $15, 30, 45\,m$.

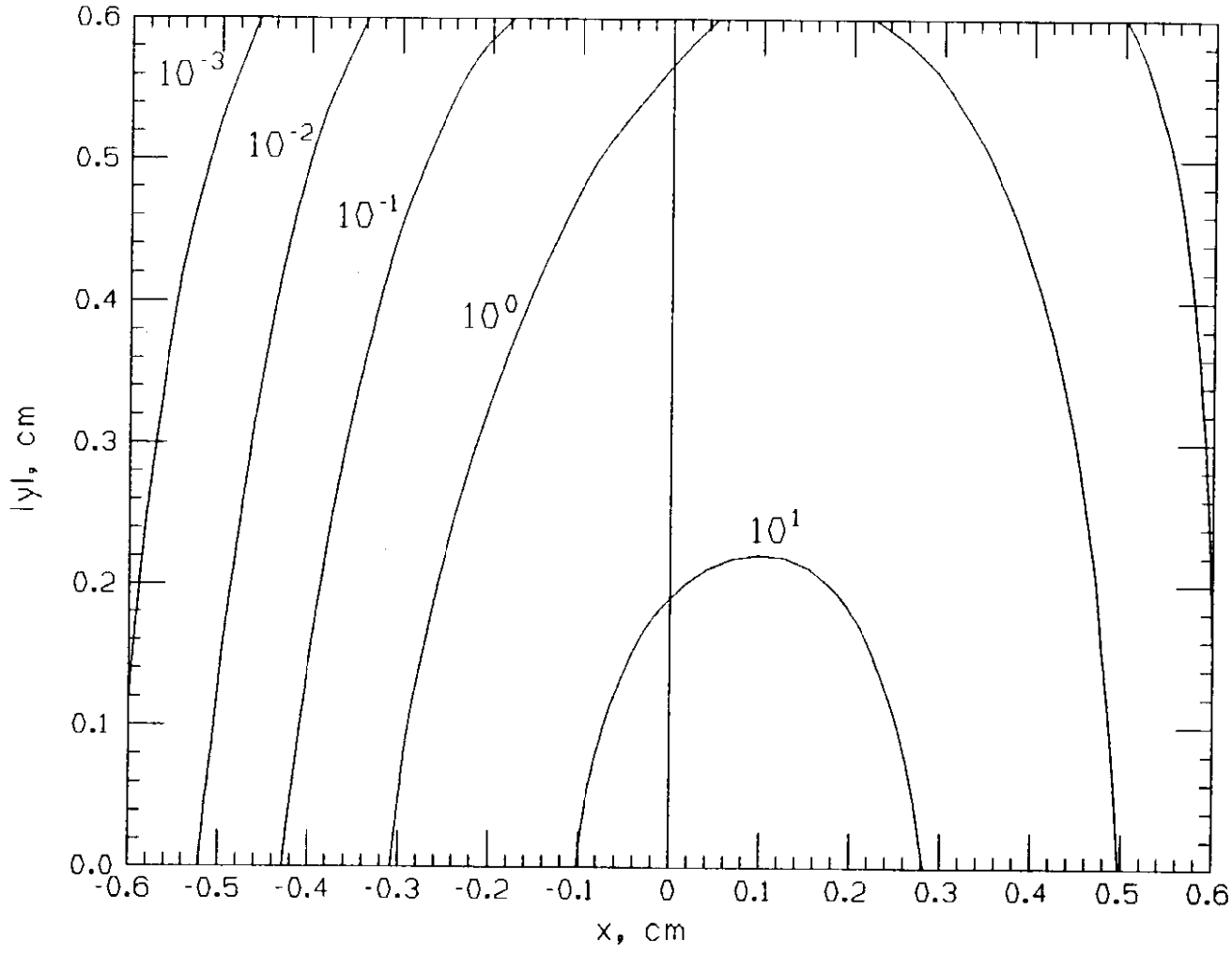

Figure 38: Contours of equal energy density in em top slice ($0 < z_t < 0.04\ cm$) of solid Aluminum target for $\sigma_x = \sigma_y = 0.15\ cm$ Gaussian beam of $20\ TeV$ protons incident at $1\ mrad$ angle.

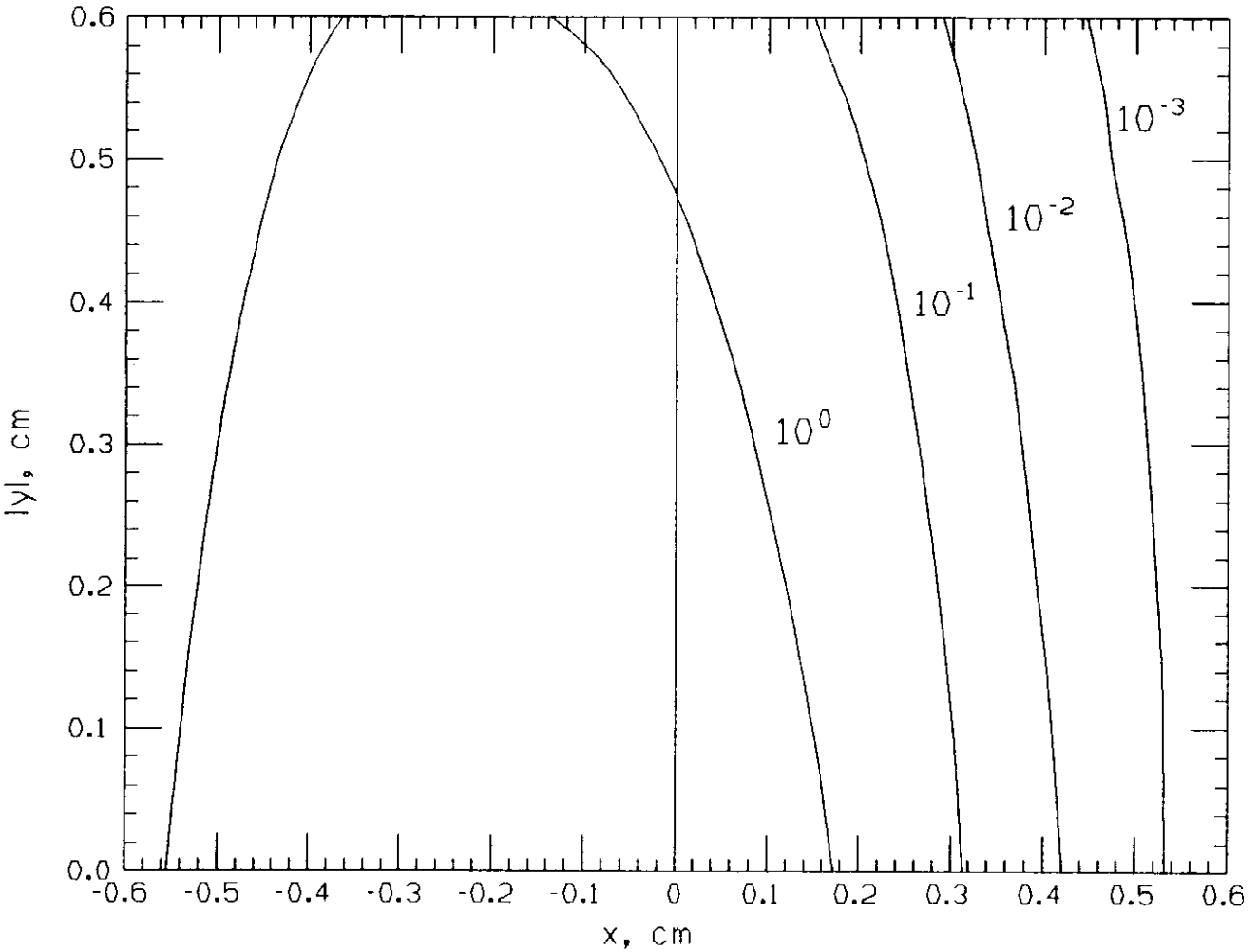

Figure 39: Contours of equal energy density in em bottom slice ($0.36 < z_t < 0.40\,cm$) of solid Aluminum target for $\sigma_x = \sigma_y = 0.15\,cm$ Gaussian beam of $20\,TeV$ protons incident at 1 $mrad$ angle.

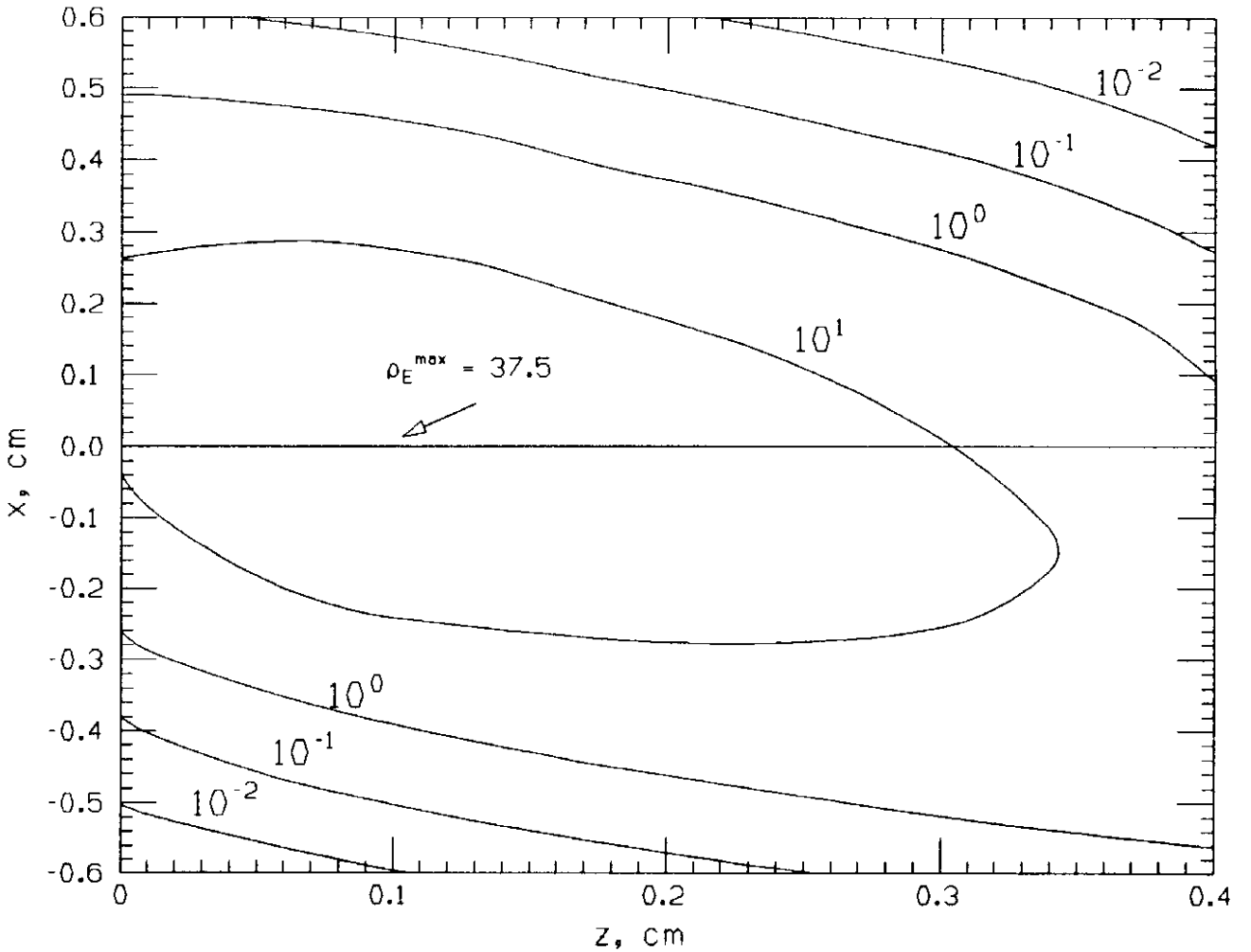

Figure 40: Contours of equal energy density at $y = 0$ in solid Aluminum target for $\sigma_x = \sigma_y = 0.15\,cm$ Gaussian beam of 20 TeV protons incident at 1 *mrad* angle.

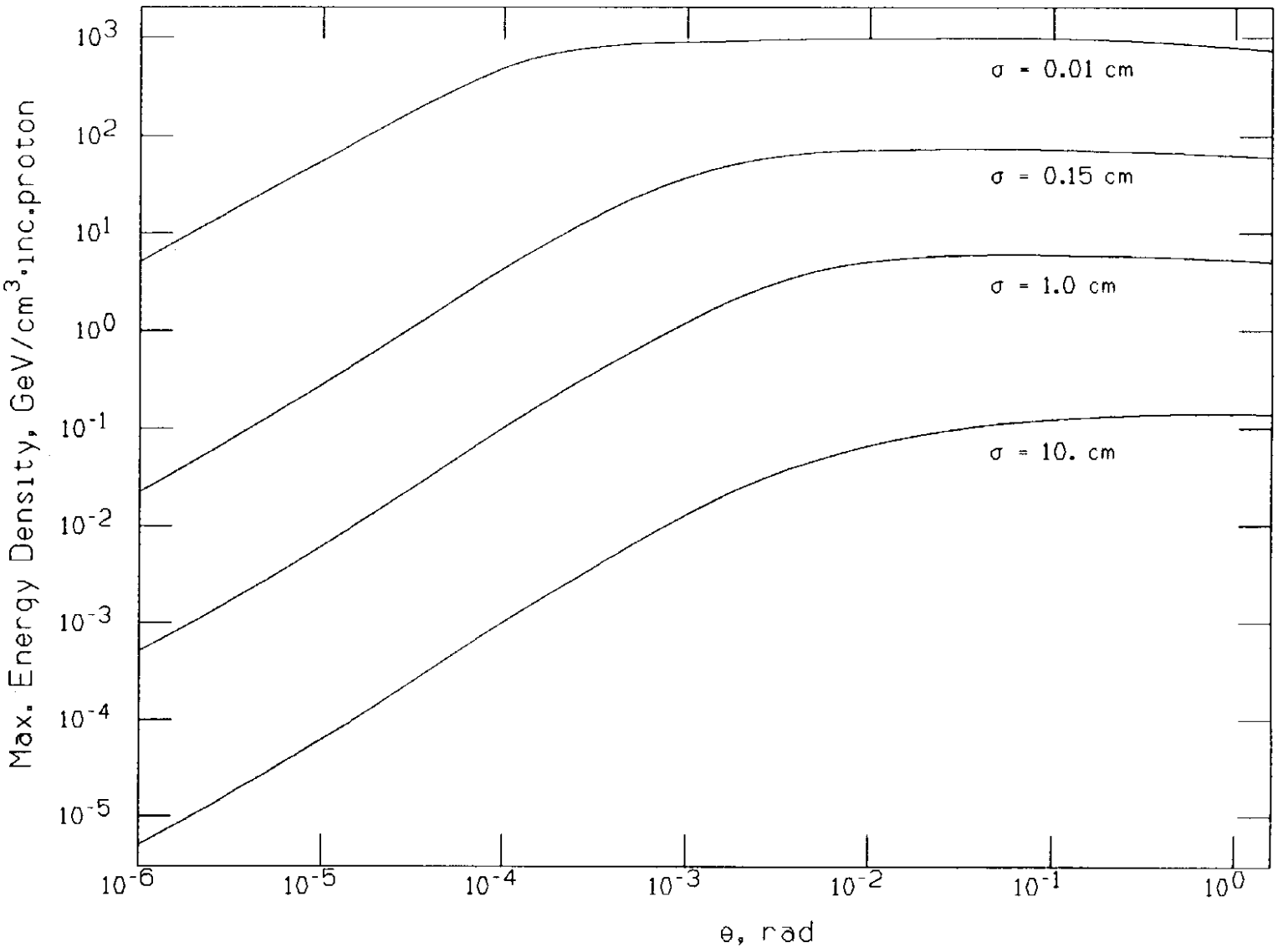

Figure 41: Overall maximum energy density for Gaussian beams with various σ of 20 TeV protons incident on solid Aluminum target versus incident angle (θ).

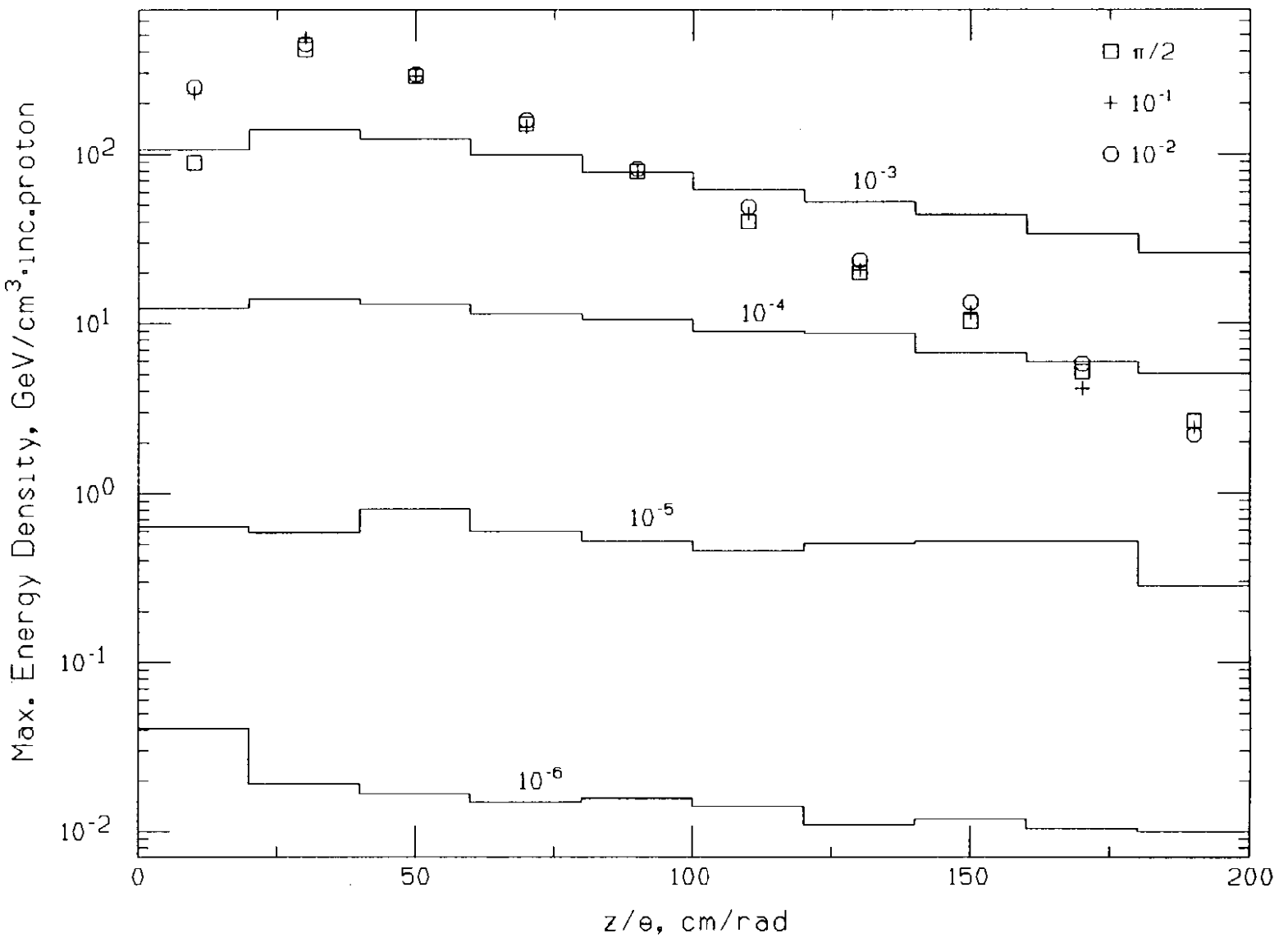

Figure 42: Maximum energy density for $\sigma_x = \sigma_y = 0.15\,cm$ Gaussian beam of $20\,TeV$ protons incident at various angles on solid Iron versus distance along beam in target.

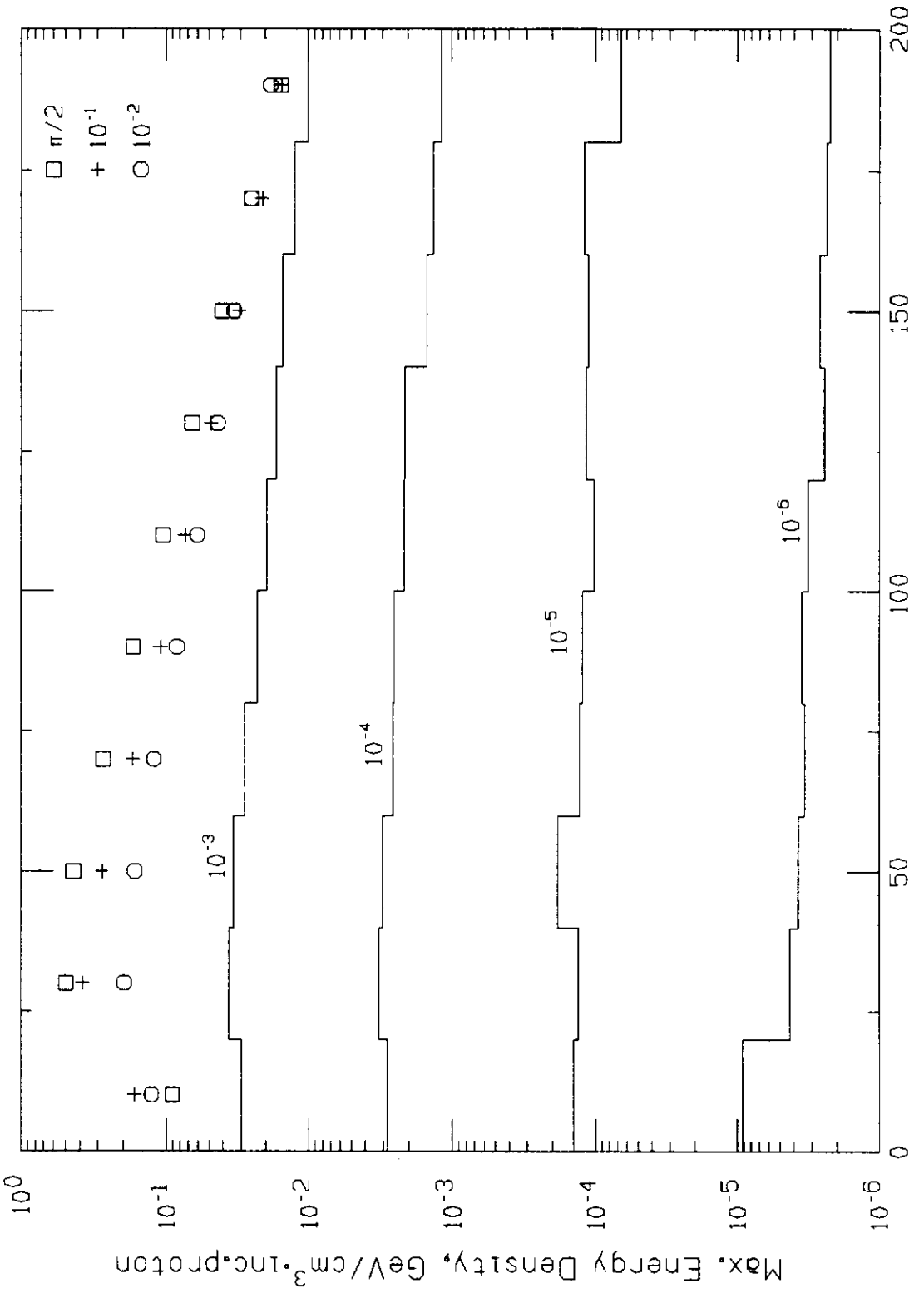

Figure 43: Maximum energy density for $\sigma_x = \sigma_y = 10\,cm$ Gaussian beam of $20\,TeV$ protons incident at various angles on solid Iron versus distance along beam in target.

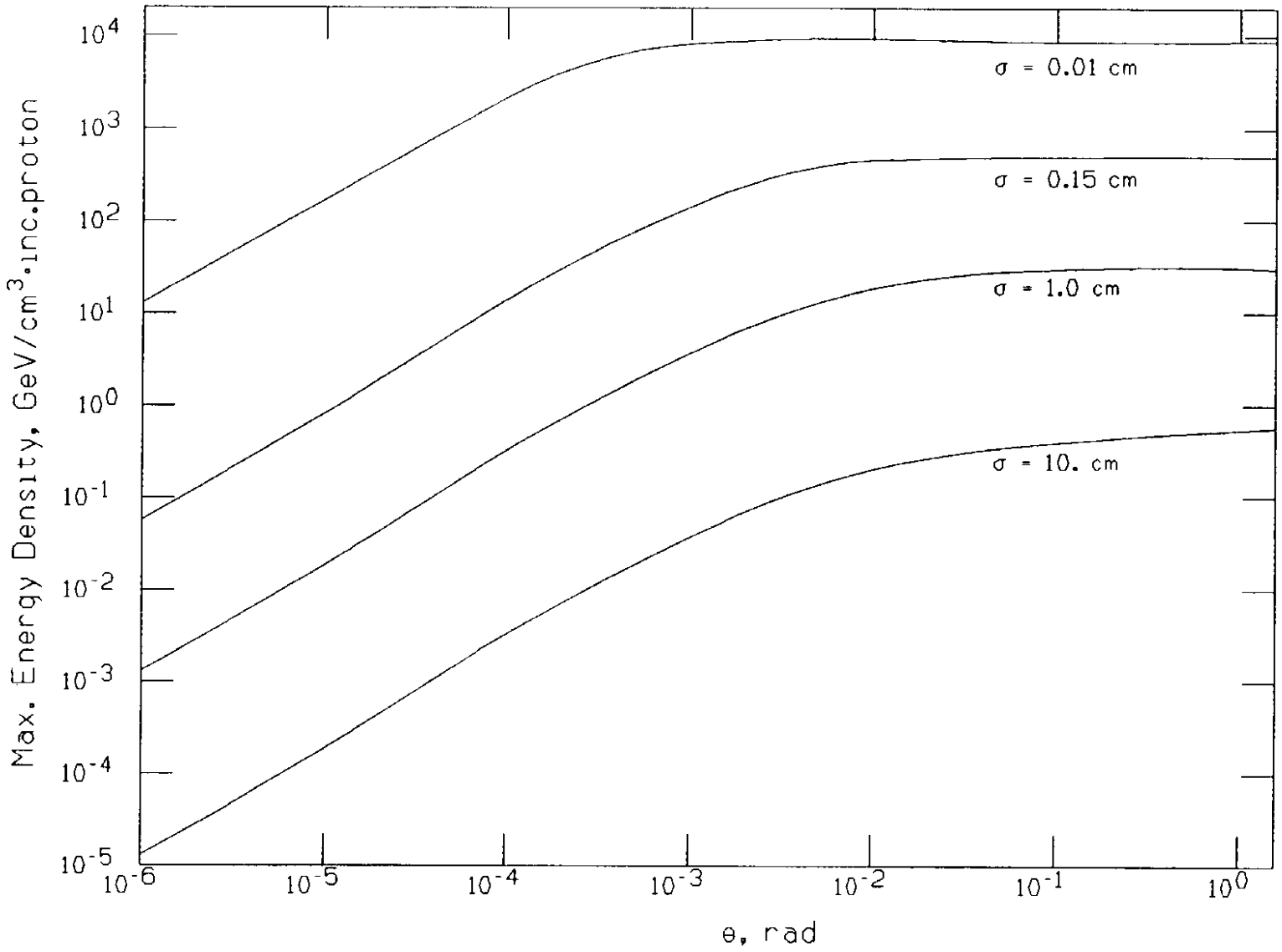

Figure 44: Overall maximum energy density for Gaussian beams with various σ of 20 TeV protons on solid Iron versus incident angle (*theta*).

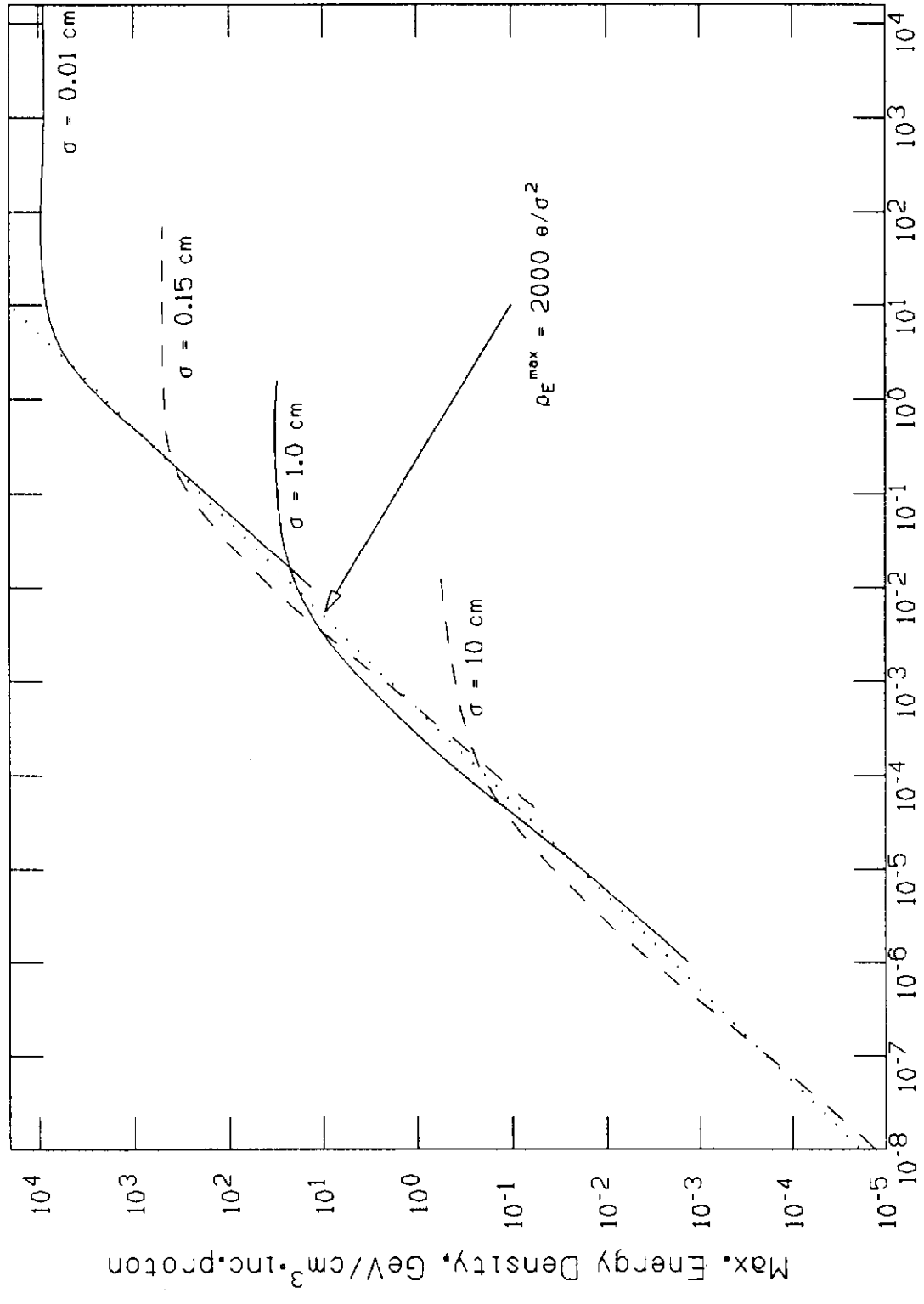

Figure 45: Overall maximum energy density for Gaussian beams with various σ of 20 TeV protons incident at various angles (θ) on solid Iron versus scaling variable θ/σ^2.

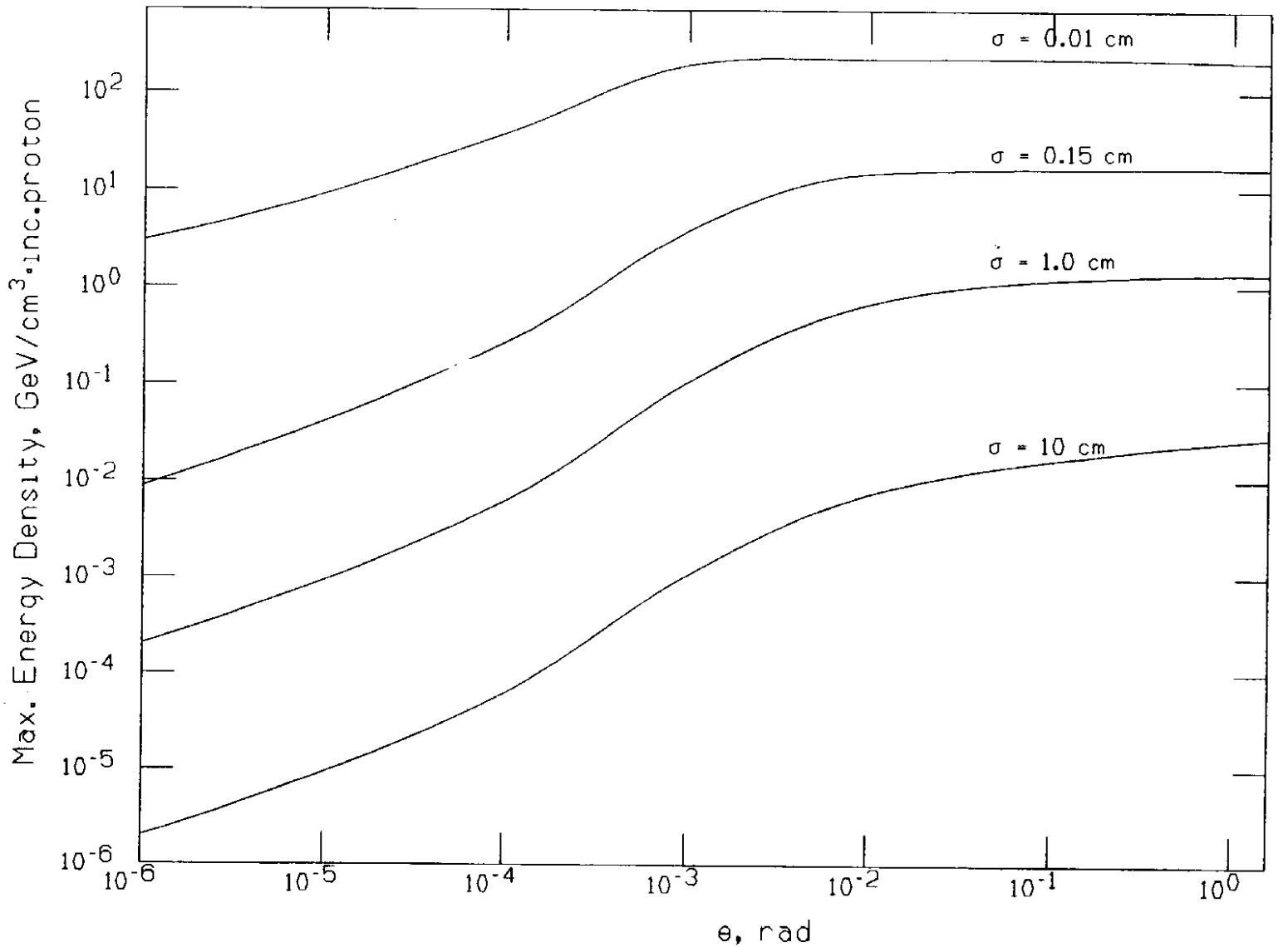

Figure 46: Overall maximum energy density for Gaussian beams with various σ of 1 TeV protons on solid Iron versus incident angle (*theta*).

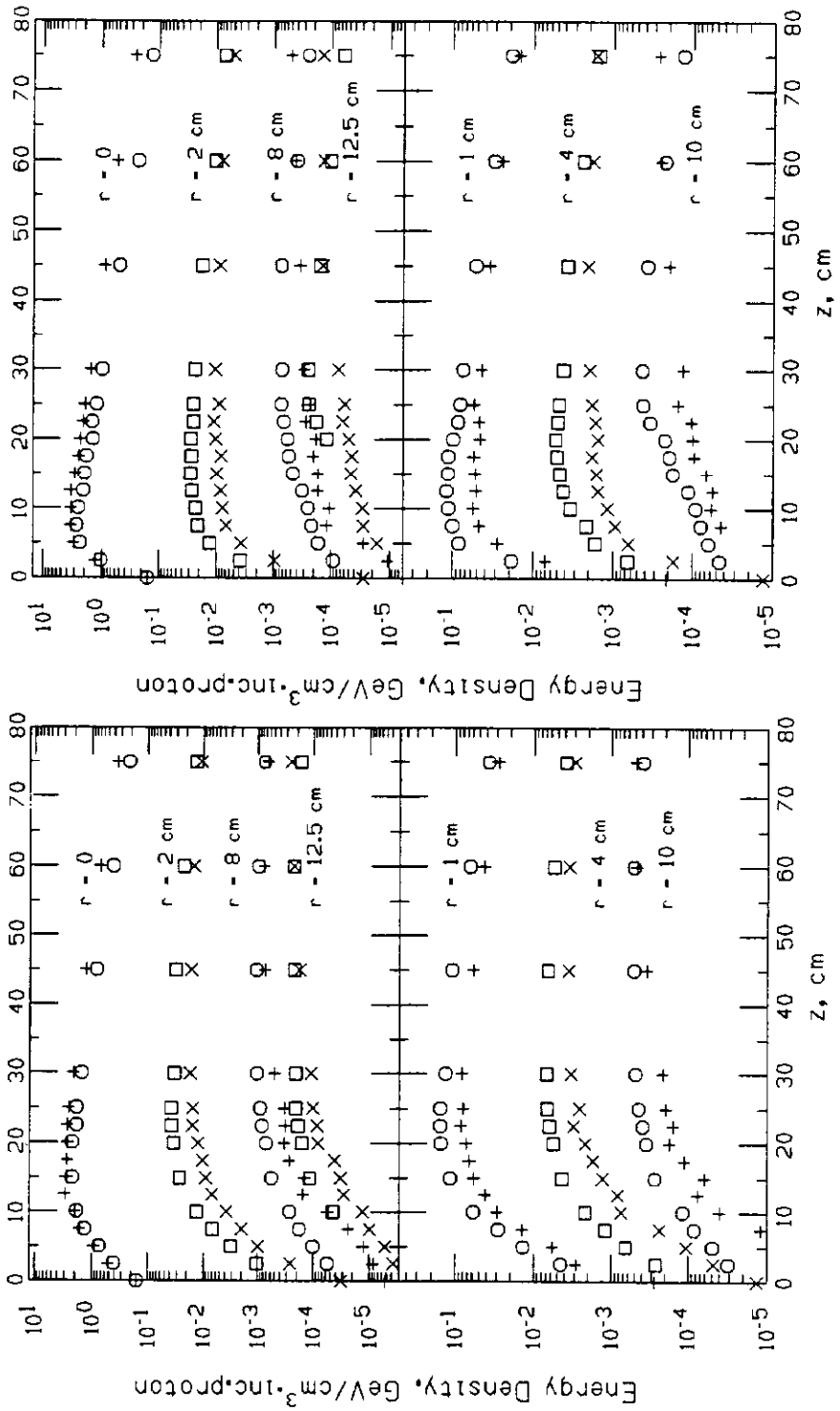

Figure 47: Comparison of 300 GeV data of Muraki et al. ($\bigcirc, \square$) with CASIM ($+, \times$). (left)–iron, (right)–lead.

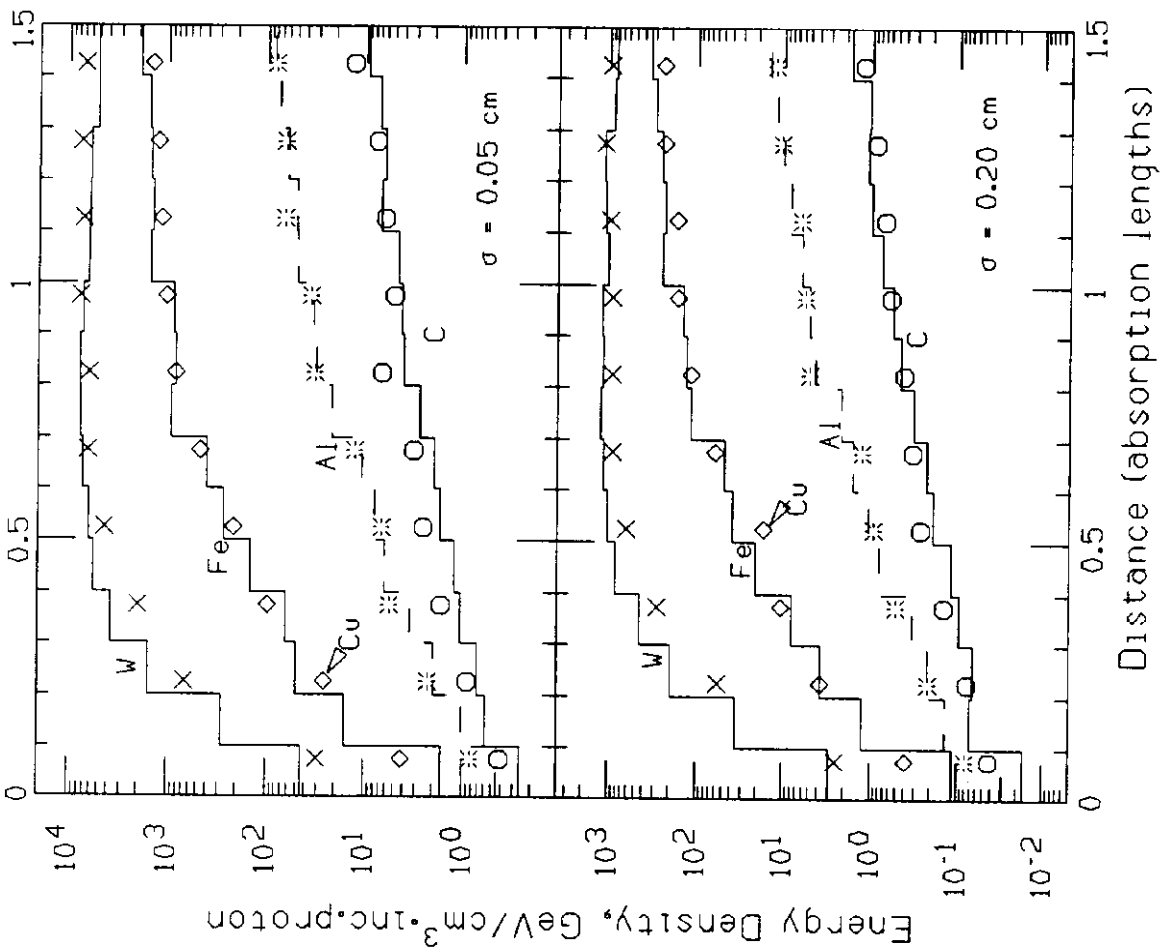

Figure 48: Comparison of predictions at 20 TeV of MARS10 (point symbols) and CASIM (histograms) for on-axis energy density in various materials.